Internal Report
DESY F35D-97-03
February 1997

Neutral Strange Particle Production in Neutral Current Deep Inelastic Scattering at HERA

by

R. T. Ullmann

Neutral Strange Particle Production in Neutral Current Deep Inelastic Scattering at HERA

by
Rainer Thomas Ullmann

Department of Physics
McGill University, Montréal
November, 1996

A thesis submitted to the Faculty of Graduate Studies and Research
in partial fulfilment of the requirements of the degree of
Doctor of Philosophy

Contents

LIST OF FIGURES

List of Tables

RÉSUMÉ

Cette thèse présente la première étude de la production de particules étranges neutres dans des événements de diffusion inélastique profonde, produites dans des collissions de faisceaux de protons d'une énergie de $820\,GeV$ et de positrons de $27.5\,GeV$. Les données ont été accumulées en 1994 avec le détecteur ZEUS au collissionneur HERA. On a déterminé les taux des K^0 et Λ en fonction de la pseudorapidité et de l'impulsion transverse de ces particules, dans des événements situés dans la région cinématique limitée par $10\,GeV^2 < Q^2 < 1280\,GeV^2$, $0.0003 < x < 0.1$ et $y > 0.04$. On a étudié la production de ces particules et leurs énergies moyennes à l'aide d'une fonction de la distance relative à la direction du quark diffusé, d'une fonction du transfert de quadri-impulsion Q^2 ainsi que de l'énergie du centre de masse hadronique W du processus de diffusion ep. Les taux de K^0 et Λ dans la région cinématique limitée par $10\,GeV^2 < Q^2 < 640\,GeV^2$, $0.0003 < x < 0.01$ et $y > 0.04$ sont comparés avec les résultats déterminés par un ensemble de données accumulées en 1993, produites dans des collissions de faisceaux de protons de $820\,GeV$ et d'électrons de $26.7\,GeV$. On a comparé les propriétés de la production de K^0 dans des événements avec et sans brèche d'activité hadronique entre la direction du proton et du quark diffusé afin de sonder des différences des mécanismes de production de K^0 dans des processus de diffusion diffractifs et non-diffractifs.

ABSTRACT

This thesis presents a first study of various aspects of K^0 and Λ production in neutral current deep inelastic scattering of $27.5\,GeV$ positrons and $820\,GeV$ protons. The data were accumulated with the ZEUS detector at HERA in the 1994 run period. The average multiplicities for the neutral strange particle production as functions of pseudorapidity η and transverse momentum p_t have been determined in the kinematic range $10\,GeV^2 < Q^2 < 1280\,GeV^2$, $0.0003 < x < 0.1$ and $y > 0.04$. The particle and energy flow with respect to the struck quark direction, as well as the dependence of the average production rate as function of the four-momentum transfer Q^2 and the hadronic centre of mass energy W of the ep scattering process have been studied. The K^0 and Λ multiplicities in the kinematic range $10\,GeV^2 < Q^2 < 640\,GeV^2$, $0.0003 < x < 0.01$ and $y > 0.04$ are compared with the results from data from the 1993 run period with $26.7\,GeV$ electrons and $820\,GeV$ protons. The production mechanisms of K^0 in events with and without large rapidity gaps with respect to the proton direction are compared in order to probe differences in diffractive and non-diffractive scattering processes.

ACKNOWLEDGMENTS

It seems like a hopeless venture to try to thank all the people who helped over the last years to write this thesis.

First of all I'd like to thank my supervisor, Prof. David Hanna, for his support and encouragement throughout the whole time, for many long discussions and lots of good advice. I'm also grateful to him and to Dr. Joseph Mitchell for making easy my decision to come to McGill.

I am grateful to all members of the ZEUS collaboration for advice and criticism, in particular to my collaborators on the "Strange Particles in DIS" subject, Dr. Jutta Hartmann, Dr. Chris Matthews, Simon George, Prof. Luis Labarga and Juan-Pablo Fernandez. Discussions with Profs. Douglas Stairs and François Corriveau were also very helpful. I want to thank Dr. David Gilkinson for his help with various problems with program packages and computing facilities. Special thanks to Dr. habil. Gabriele Zacek for the thorough reading of my thesis in its various stages and for her many critical comments.

I'm very grateful to my office colleagues at DESY, who helped to make it fun coming to work : Laurel Sinclair, Ling Wai Hung and Marc St.Laurent. Not to forget my other "fellow Canadians" Patrick Saull, Richard Teuscher, Frédéric Bénard, Kyung Kwang Joo, Peter Fagerstroem, Mike Cardy, Burkhard Burrow, Michael Riveline, Mohsen Khakzad, David Simmons, Frank Chlebana, Kathrin Farrow, Sampa Bhadra and John Martin. Special thanks to Miloš Brkić and Cortney Sampson - hey, we had good times, didn't we ? I also want to include into the list of people I am indebted to : Gabriele, Thomas, Bjoern, Bettina, Maria, Susanna, Jon, Wouter, Bill, and Larry. I hope I didn't forget anyone...

Back at McGill I want to thank my office mates Nirinjan Govind, François Drolet, Dean Stinson-O'Gorman, Kostas Kordas, Graham Cross, Andreas Ochs, Claude Théoret, Shem Malus and Marko Milek. Thanks to Paul Mercure and Juan Gallego for providing and maintaining the computing environment. Life in Montréal would not have been as wonderful without my friends Mary, Peter, Philippe, Jim,

Alex, Klaus, Jason, Sean & Bonnie, Lynda, Robert, Scott & Laura, Mikko & Merja, Mikko, Oleh, Dmitri, Erol and many others....

Last but not least, all my gratitude to my family for their love and support.

1

INTRODUCTION

1.1 *Strange Particles in High Energy Physics*

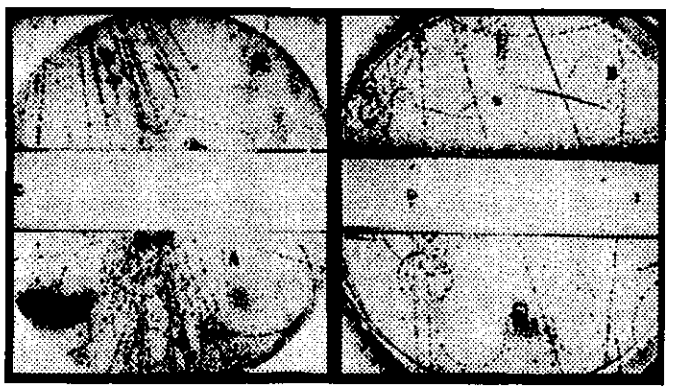

Figure 1.1: *Original observation of the decay of a neutral (left image) and a positively charged (right image) V-particle in cloud-chamber photographs of G. D. Rochester and C. C. Butler at Manchester University. The interaction of cosmic ray particles with a 3 cm lead plate (horizontal bar in the pictures) has been studied in a magnetic field. The images are colour inverted for reasons of better visibility of the tracks. The neutral V is probably a K^0, which is produced in an interaction of the cosmic ray particles with the lead, and decays into a negative and a positive pion. The characteristic V-shaped fork of the tracks are seen close to the letter "A" (lower right half of the left image). Close to the letter "B" (upper right half of the right image) a K^+ in the cosmic ray decays into a μ^+ and a ν. The μ^+ leaves a track penetrating through the 3 cm lead plate, the neutrino escapes undetected.*

In 1947 G. D. Rochester and C. C. Butler reported in an article in Nature ([Roc47]) about their discovery of new unstable elementary particles in their investigation of the nature of the cosmic rays discovered earlier. In about 1% of the 5000 cloud-chamber

photographs collected in one year they observed V-shaped tracks that could not be explained as a scattering process of a charged particle but rather as spontaneous transformations of unknown types of particles. Due to their decay topology these particles were named "V-particles". The mass of these V-particles was determined to be about half a proton mass. Figure 1.1 shows two cloud-chamber photographs from the original publication. In 1951, the decays of more massive V-particles, slightly heavier than the proton, were observed in bubble chamber photographs by several experimenters. Figure 1.2 shows such a photograph of a Λ decay from the 80 *inch* bubble chamber in Brookhaven.

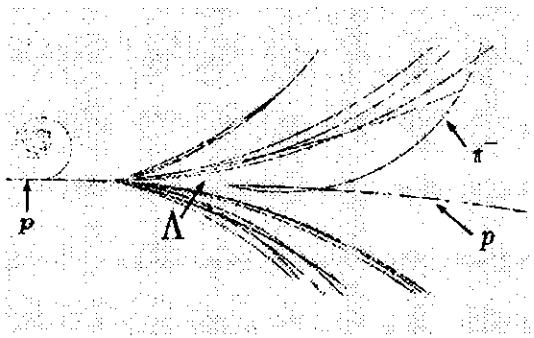

Figure 1.2: *(Colour inverted) photograph of the production and decay of a Λ-particle in the 80 inch bubble chamber at the Brookhaven National Laboratory. A high energy proton enters from the left and collides with a proton at rest in the liquid hydrogen. The magnetic field of the experiment bends negative particle tracks on upward curves. In the collision in this image, several charged particles and a Λ are produced. The neutral Λ travels undetected towards the right until it decays into a π^- and a proton (forward going track). The charged particles are charged pions, a proton and a K^+. The latter is produced in the "associated production" with the Λ.*

Long since then these "strange" new neutral particles have been understood in the framework of the newly developed theory of elementary particle physics and are referred to as the neutral mesons K^0 and $\bar{K}^0$ (henceforth both simply referred to as K^0) and the neutral baryon Λ and its anti-particle $\bar{\Lambda}$ (henceforth both referred to as Λ^0 if distinction is not intended). Their properties have been measured and established to high precision (see Appendices A.1.1 and A.1.2 for a brief summary

of the particle properties).

In case of the K^0 one actually observes the weak decays of the CP eigenstates K^0_S and K^0_L (see appendix A.1.1), where 'S' and 'L' stand for 'Short' and 'Long' respectively, indicating the difference in their mean life time. Due to their decay pattern the K^0_S and Λ^0 are identified using their main decay channels $K^0_S \to \pi^+\pi^-$ ($68.61 \pm 0.28\%$), $\Lambda \to p\pi^-$ and $\bar{\Lambda} \to \bar{p}\pi^+$ ($63.9 \pm 0.5\%$). In fact, due to their well-measured mass and lifetime, they are often used to improve on the understanding of the detector.

The general study of strange particle production started in the 50's with bubble chamber experiments and continued later on with different types of colliding beam or fixed target experiments at various centre of mass energies. The strange particles turned out to be a very useful tool, so called "strangeness tags", which allowed one to test various aspects of particle production. In the deep inelastic scattering (DIS) processes, the study of strange particle production can provide direct information about the strange (sea) quark content of the nucleon. With increasing energy the appearance of jets - highly collimated particle showers - in scattering processes allowed one to investigate the fragmentation processes - the transition from the partons of the scattering process into observable multi-hadron states. Although the theory of particle physics has made astonishing progress during the last decades it is far from being completely understood. Especially this fragmentation process can not be completely calculated, but has to be described by phenomenological models. Much effort has been dedicated over the last decades to gain insight into the fragmentation processes; the study of strange particle production in the fragmentation chain is one step in this direction.

Of interest is, for example, the ratio of strange particle to light non-strange particle creation, often referred to as the degree of SU(3) symmetry violation. In phenomenological models this is parameterized by the strange quark suppression factor P_s/P_u, the probability for creating a s- rather than a u- or d-quark from the vacuum during the fragmentation process. Production of quarks heavier than the s in the fragmentation is strongly suppressed. P_s/P_u has been measured before by different experiments and at various centre of mass energies :

- At e^+e^- colliders with symmetric beam energies up to $\sim 90\,GeV$[1].
- With neutrino and antineutrino beams on nucleon targets with typical beam energies of $20 - 30\,GeV$.
- At $p\bar{p}$ experiments with beam energies up to $\sim 1\,TeV$ covering a wide range in hadronic centre of mass energies.

Deep inelastic ep scattering (DIS) also covers a wide range of hadronic centre of mass energies with an accurate reconstruction of the event kinematics from the scattered lepton. DIS allows one to study in one experiment aspects of fragmentation that appear in either e^+e^- or hadron collider experiments. The fragmentation in the region of the scattered quark, the current region, resembles that of the pair-produced quarks in e^+e^- interactions, the diquark fragmentation of the proton remnant, the target region, is similar to hadron collider experiments. The region in between, the colour flow region, exists in both types of collider experiments.

HERA allows the study at hadronic centre of mass energies of $\sqrt{s} \sim 300\,GeV$ and therefore at least one order of magnitude higher than in previous lepton nucleon scattering experiments. The increased kinematic range also includes a region where the gluon density in the proton plays an important role, leading to a mechanism that allows pair-production of quarks. This mechanism is called boson gluon fusion and the study of strange particle production can provide insight into this production mechanism. Strange particles are also found in most of the decay chains of heavier particles. They therefore provide indirectly information about the production of these heavier particles in boson gluon fusion and the distribution of the heavier quarks in the nucleon. The acceptance of the central tracking detector of ZEUS experiment allows us to study the strange particle production in the fragmentation region of the

[1] Throughout this thesis I will use GeV as unit for energies, momenta and masses, i.e. let $c = 1$.

struck quark and colour flow region. The fragmentation region of the proton remnant is generally not accessible.

In about 10 % of the DIS, events no proton remnant is detected, which results in a large rapidity gap between the acceptance limit in the proton direction and the first visible particle in the detector. The properties of these "diffractive" events are consistent with a scattering process of a photon off a colourless object, generally referred to as a pomeron. However, the nature of this pomeron is not understood and a study of strange particle production in these processes can provide information of its possible partonic structure and the fragmentation mechanism in diffractive processes.

As this section showed the strange particles, although well established and understood, are still a useful tool to study interesting topics in high energy physics.

1.2 Outline

This thesis describes in detail the analysis of strange particle production in deep inelastic e^+p scattering at HERA. First results, based on the data collected in the 1993 e^-p run period, were described in the ZEUS-Note 94-155 and the preprint DESY 95-084. The latter has been published by Zeitschrift für Physik, C68 (1995), pages 29-42.

After the review on the history of strange particle production in this chapter, chapter 2 gives a brief introduction to the Standard Model of high energy physics with an emphasis on deep inelastic lepton-nucleon scattering and diffractive processes. Chapter 3 describes the experimental environment in which the data for this thesis have been accumulated : the HERA collider facility and the ZEUS experiment. Chapter 4 will introduce the event kinematics in deep inelastic scattering and methods to reconstruct the kinematic variables. Chapter 5 gives a description of the Monte Carlo generators and underlying models that are used in this thesis. Chapter 6 outlines the procedure to isolate a sample of DIS events from the data accumulated with the ZEUS detector. Chapter 7 is devoted to the reconstruction of a clean sample of neutral strange particles, Chapter 8 to the procedures necessary to correct for detector

acceptance and reconstruction efficiencies. The results are presented and discussed in chapter 9. Chapter 10 finally gives a short summary of the results of this thesis and an outlook for a possible continuation of this study. A brief summary of properties of neutral strange particles and a glossary for expressions used in this thesis are given in the appendix.

2

Introduction to Deep Inelastic Scattering (DIS)

High energy particle physics is the quest to find the ultimate constituents of matter and to understand the nature of the interactions between them. Originating from the study of nuclear physics it evolved to an independent field of research. In the early 30's of this century a very simple picture with few elementary particles was commonly accepted. The elementary particles of this picture were the proton, the neutron and the electron; all existing matter is built up from these : the proton and the neutron form the nuclei, the nuclei together with the electrons build up the atoms and finally conglomerates of atoms form the matter. In attempts to understand the details of internuclear forces with early accelerator experiments and in high energy cosmic ray interactions hundreds of new particles have been detected. This could not be explained within the picture of nuclear physics without including *ad hoc* a large variety of new "elementary" particles and therefore destroying the simplicity of the theory. Systematic particle spectroscopy and attempts to introduce an order into this seeming chaos of new particles led finally to a new simple picture. Today this new picture, the so called "Standard Model" as described in the following section, is generally accepted to be a good model - at least no contradicting results or definitive evidence for physics beyond it have been found so far.

2.1 The Standard Model

The Standard Model (SM) is the theory of the elementary particles and their interactions. In the picture of the SM the basic constituents of all matter are three generations of fundamental fermions and their antiparticles as listed in table 2.1.

The quarks or leptons of the second and third generation resemble strongly the corresponding quark or lepton of the first generation, except for their higher masses (hence the term "generation"). Three fundamental forces[1] (see table 2.2) mediated by vector bosons are sufficient to describe all particle interactions. The mathematical formulation of the SM in terms of a field theory is based on the $SU(3)_C \otimes SU(2) \otimes U(1)$ gauge group.

Generation	Quarks			Leptons		
	name	symbol	charge	name	symbol	charge
I	up	u	$+\frac{2}{3}$	electron neutrino	ν_e	0
	down	d	$-\frac{1}{3}$	electron	e	-1
II	charm	c	$+\frac{2}{3}$	muon neutrino	ν_μ	0
	strange	s	$-\frac{1}{3}$	muon	μ	-1
III	top	t	$+\frac{2}{3}$	tau neutrino	ν_τ	0
	bottom	b	$-\frac{1}{3}$	tau	τ	-1

Table 2.1: *The fundamental fermions of the Standard Model. For each particle an antiparticle exists. The charge is in units of (positive) electron charges.*

The weak interaction describes quark (or lepton) transitions between or within quark (or lepton) generations. Depending on whether the interaction involves only hadrons, or hadrons and leptons or only leptons, they are often classified as hadronic (or nonleptonic), semileptonic and leptonic interactions. The force is mediated by vector bosons, the Z^0 in case that the interaction proceeds without charge transfer, or the W^+ and W^- otherwise. The electromagnetic interaction describes the interaction between the charged quarks and leptons, mediated by photons. Glashow, Salam and Weinberg succeeded in unifying the weak and the electromagnetic forces into one electroweak force. The underlying field theory, the so called Quantum Flavour

[1] Due to its small relative coupling strength, gravity is generally negligible in applications to high energy experiments and will therefore not be further mentioned here. However, Theories of Everything (TOEs) exist that interpret all four forces as different aspects of one, more fundamental, force.

Interaction	Mediating gauge boson					
	strength	name	symbol	mass	charge	spin
Strong	~ 1	gluon	g	massless	0	$1\hbar$
Electromagnetic	$\frac{1}{137}$	photon	γ	massless	0	$1\hbar$
Weak	1.02×10^{-5}	Vector bosons	Z^0	$(91.17 \pm 0.02)\,GeV$	0	$1\hbar$
			$W^{\pm}$	$(80.22 \pm 0.26)\,GeV$	± 1	$1\hbar$
Gravity	0.53×10^{-38}	graviton	G	massless	0	$2\hbar$

Table 2.2: *Mediators of the fundamental forces*

Dynamics (QFD) is based on the $SU(2) \otimes U(1)$ gauge group.

The strong interaction description is based on the $SU(3)_C$ algebra of Quantum Chromodynamics (QCD). Besides the fractional charges each quark flavour carries a "colour (charge)","red","green" or "blue" (r,g,b), the anti-quarks the corresponding anti-colour "anti-red" ($\bar{r} = g + b$),"anti-green" ($\bar{g} = r + b$) or "anti-blue" ($\bar{b} = r + g$). Hence the index C for "Colour"[1] in $SU(3)_C$ and the name "Chromodynamics". The strong force is responsible for binding the quarks into hadrons, quark-antiquark (meson) or three-quark (baryon) colour singlet bound states. The force proceeds via colour exchange, mediated by gluons that carry a colour and an anticolour at the same time. This allows direct interactions between the gluons (in QED $\gamma\gamma$ interactions are only a higher order perturbative effect). The colour hypothesis explains the notion of confinement, *i.e.* that quarks and gluons are confined inside hadrons and restores the consistency with the Pauli Exclusion for particles like the fermions Δ^{++} or Ω^-. No evidence for free quarks or gluons and other colour non-singlet states (*e.g.* qq or $qqqq$ states) has been found so far.

[1]The name "colour" for this quantum number has been chosen in analogy to the additive colour model in optics, where the superposition of red, green and blue light leads to a white light; it is just a name for an additional internal degree of freedom. However, this picture is only a "pedestrian approach" to the complicated mathematical formalism.

2.2 The Quark Parton Model and Structure Functions

By analogy to Rutherford's scattering experiments (α particles on atoms in 1911), which led to the nuclear atom model, in the mid 1950's electron nucleon scattering experiments ([McA56] were done in order to probe the electromagnetic structure of the nuclei. In the late 1960's, with an electron energy of $7 - 17\,GeV$, the SLAC-MIT experiment ([Blo69], [Bre69]) confirmed a partonic substructure inside the proton. The differential cross section of the ep scattering process was then formulated in terms of two structure functions $F_{1,2}$:

$$\frac{d^2\sigma}{dQ^2dx} = \frac{4\pi\alpha^2}{xQ^4}[y^2xF_1(x,Q^2) + (1-y)F_2(x,Q^2)] \tag{2.1}$$

where Q^2,x and y are the kinematic variables as described in section 4.1. The structure functions F_i are considered to be dimensionless functions of two independent variables x and Q^2. Measurements of the structure function F_2 showed "scaling behaviour", $F_2(x,Q^2) \rightarrow F_2(x)$ which was evidence for a scattering process with a pointlike "parton" inside the proton ([Bjo69]). In this parton model a fast moving proton looks like a bunch of partons with small transverse momentum with respect to the proton direction. The partons share the momentum of the proton and interact as free particles. The experimental proof of the Callan Gross relation ([Cal69]) $F_2(x) = 2xF_1(x)$, derived for spin 1/2 partons, allowed one to identify the partons with the earlier proposed quarks. In this picture, referred to as quark parton model (QPM), the structure function F_2 is interpreted as :

$$F_2(x) = x\sum_i e_i^2 q_i(x) \tag{2.2}$$

where the sum is over the quark flavours $i = u, \bar{u}, d, ..$ of the partons in the proton, e_i are the corresponding charges of the partons and $q_i(x)$ is the number of partons of flavour i with a fraction between x and $x + dx$ of the proton momentum.

2.3 QCD Improved QPM and Perturbative QCD

From the beginning of the 1970's the study of structure functions was the subject of a variety of lepton-nucleon scattering experiments. With electrons, muons and

neutrinos as probes and different targets the functions $F_2^{(en)}$,$F_2^{(ep)}$, $F_2^{(\nu p)}$, $F_2^{(\bar{\nu}p)}$, etc. were measured, however, the direct measurement of the parton distribution functions was not possible. Using isospin symmetry considerations and the simple form of the F_2 structure functions allowed one to derive "sum rules" that made predictions for the measured values of combinations of structure functions. The test of one of these sum rules, which predicted the momentum fraction of all quarks and antiquarks in the nucleon, led to the surprising result that only around half of the proton momentum was carried by the partons considered so far. The "missing" partons were identified as the gluons of QCD. The inclusion of the gluons into the QPM explained the deviation from scaling behaviour that was observed with a logarithmic dependence on Q^2. In the QCD improved QPM this dependence is described by the evolution of the quark and gluon momentum distributions q_i and G :

$$\frac{dq_i(x,Q^2)}{dlnQ^2} = \frac{\alpha_s(Q^2)}{2\pi}\int_x^1 \left[\frac{dy}{y}\sum_{j=1}^{2N_f} q_j(y,Q^2)P_{q_iq_j}(\frac{x}{y}) + G(y,Q^2)P_{q_iG}(\frac{x}{y})\right] \quad (2.3)$$

$$\frac{dG(x,Q^2)}{dlnQ^2} = \frac{\alpha_s(Q^2)}{2\pi}\int_x^1 \left[\frac{dy}{y}\sum_{j=1}^{2N_f} q_j(y,Q^2)P_{Gq_j}(\frac{x}{y}) + G(y,Q^2)P_{GG}(\frac{x}{y})\right]$$

The "splitting functions" $P_{q_iq_j}(z)$ describe the probability that a quark of flavour q_j ($j = 1, 2N_f = u, d, s, ..., \bar{u}, \bar{d}, \bar{s}, ..$) turns under emission of a gluon into a quark q_i with a fraction z of the original momentum. $P_{q_iG}(z)$ is the annihilation probability of a gluon into a quark q_i and anti-quark $\bar{q}_i$, and $P_{GG}(z)$ describes gluon emission from a gluon. α_s is the "running coupling constant" of QCD. The contributing diagrams are ladder diagrams with gluon and quark exchange as illustrated in figure 2.1 *a*). The longitudinal momenta are ordered along the chain (*i.e.* $x_i \geq x_{i+1}$) and the transverse momenta are strongly ordered (*i.e.* $k^2_{\perp,i} \ll k^2_{\perp,i+1}$). In leading order α_s can be calculated as

$$\alpha_s(Q^2) = \frac{12\pi}{(33-2N_f)ln(\frac{Q^2}{\Lambda^2})} \quad (2.4)$$

Λ is a QCD parameter of the order $\sim 300\,MeV$. Equations 2.3 are called the DGLAP evolution equations, named by the initials of Y. L. Dokshitzer, V. N. Gribov and L. N. Lipatov and G. Altarelli and G. Parisi who have developed them independently.

These equations are derived in perturbative QCD calculations in an expansion in $(\alpha_s ln Q^2)^n$. For HERA energies the end of the validity range is reached for $Q^2 \simeq 10\,GeV^2$ and $x \leq 0.01$ (see figure 2.2). An introduction to evolution functions and a review on experimental measurements of scaling violation can be found in [Nac86].

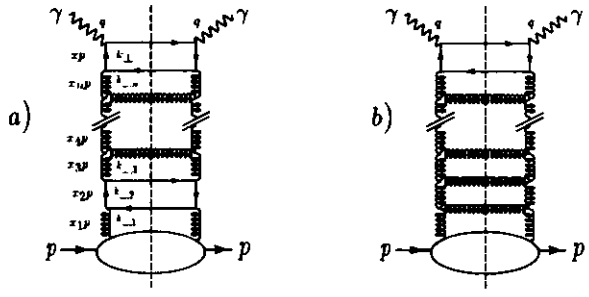

Figure 2.1: *Schematic illustration of a ladder diagram in a) leading order $ln(Q^2)$ approximation (DGLAP) and b) leading order $ln(1/x)$ approximation (BFKL).*

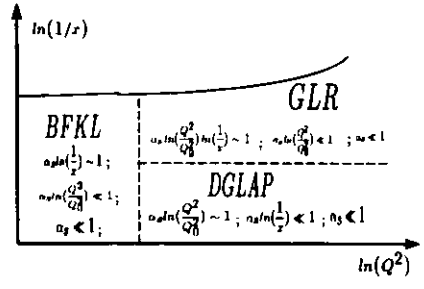

Figure 2.2: *Schematic illustration of the validity regions for the perturbative evolution equations in the $ln(Q^2)$-$ln(1/x)$ plane. $Q_0^2 \sim 4\,GeV^2$ is a reference scale.*

Retaining only the dominant terms of the DGLAP evolution equations in the small-x limit leads to the double logarithmic approximation in $(ln(Q^2)ln(1/x))^n$, as derived by V. N. Gribov and L. N. Lipatov and M. G. Ryskin (GLR). These evolution equations predict a steep rise, faster than any power of $ln(1/x)$, of the gluon

density and, since the dominant contribution for the sea-quark distributions at small x originates from $g \to q\bar{q}$ splitting. This leads to an unlimited increase of the cross section and therefore violates the Froissart bound. However, saturation effects are expected, since for sufficiently small x the partons will overlap spatially and start to recombine. This leads to nonlinear "screening corrections" in the evolution equation that effectively dampen the rise of the parton densities.

For the region of low x and at moderate Q^2 another perturbative approach in $(\alpha_s ln(1/x))^n$, has been calculated by Ya. Ya. Balitskij, V. S. Fadin , E. A. Kuraev and L. N. Lipatov leading to the BFKL equations. The small-x behaviour of F_2 is again strongly dominated by the gluon and sea-quark distributions. The gluon (and sea quark) distribution is predicted to behave like $xG(x) \sim x^{-\lambda}$ and $(xq(x) \sim x^{-\lambda})$, where λ is a parameter of $\mathcal{O}(0.5)$. As in the GLR evolution the screening corrections have to be included. This approach is equivalent to an approximation in $ln(s)$ $(1/x \sim s$ for $s \gg Q^2)$. The contributing Feynman diagrams show complicated gluon ladder structures as in figure 2.1 *b*). There is no ordering in the transverse momenta along the chain.

A more detailed review of the small x physics in deep inelastic lepton hadron scattering, relevant for the kinematic range accessible at HERA, can be found in [Bad92].

The usual strategy to extract the parton distribution functions is based on fits to the measured cross sections as a function of x at a reference scale Q_0^2. Based on the DGLAP evolution equations these distributions can then be evolved to some higher Q^2. Depending on the number of free parameters of the fit, *i.e.* depending on the constraints applied to the distribution functions, the underlying data sets and the chosen reference scale, the fit results lead to different parameterizations of the parton distributions. A variety of such different parameterizations is available, the name conventions of which usually include the initials of the physicists (*i.e.* MRS for the sets extracted from A. D. Martin, R. G. Roberts and W. J. Stirling, or GRV for M. Glück, E. Reya and A. Vogt) or an acronym for the group (*i.e.* CTEQ for

Coordinated Theoretical/Experimental Project on QCD Analysis and Phenomenology) that extracted these parameterizations.

2.4 Deep Inelastic Lepton-Nucleon Scattering

Scattering processes in high energy physics experiments are described by quantum field theory and proceed via the exchange of gauge bosons. In case of e^-p and e^+p scattering, as seen at HERA, the two lowest order Feynman diagrams of electroweak interactions which describe these interactions in the framework of the standard model are shown in figures 2.3 a) and b). Interaction processes are classified as either neutral current events (NC) or as charged current events (CC). In NC events the exchanged gauge bosons are a photon (γ) or the neutral weak vector boson (Z^0), thus leaving the lepton type and charge unchanged. In case of CC events a charged weak vector boson ($W^\pm$), changing the lepton into a neutrino, is exchanged.

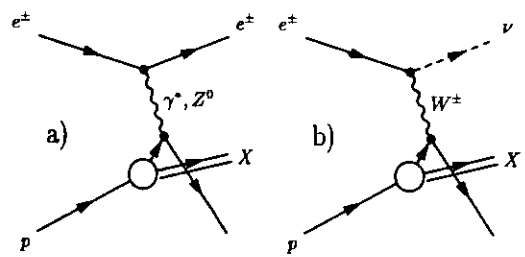

Figure 2.3: Feynman graphs for a) lowest order NC and b) lowest order CC ep scattering

This thesis concentrates on NC events where the virtuality, Q^2, of the exchanged boson is high enough to probe the structure of the proton. The definition of "high" in this context is $Q^2 \gtrsim 1 GeV^2$. These events are classified as deep inelastic scattering (DIS) events. In DIS events the photon acts pointlike and couples directly to the partons (*i.e.* valence or sea quarks) inside the proton. Since the scattered quark and the remaining diquark of the proton formed originally a colour singlet,

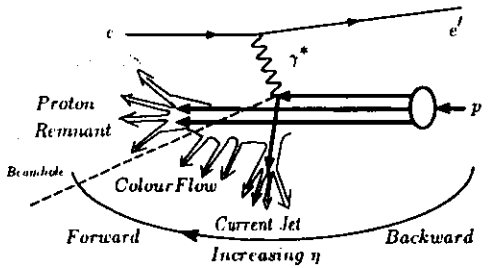

Figure 2.4: *Schematic diagram for a NC DIS event.*

the fragmentation of the two systems does not evolve independently. They are said to be colour-connected : the region between the proton remnant and the current jet (*i.e.* the fragmenting scattered quark) is filled by hadronic activity due to radiation processes that lead to local colour confinement. This region is often referred to as "Colour Flow" region. Due to the high asymmetry in the beam energies at HERA the final states are boosted strongly in the forward direction[1]. For DIS events this means that the scattered proton (or proton remnant) escapes usually undetected into the forward beam pipe ("Beamhole") while the jet associated with the scattered quark ("Current Jet") is well within the calorimeter and detected. Figure 2.4 shows a schematic diagram of the event topology for a NC DIS event at HERA, figure 2.5 shows a typical ZEUS event display for such an event.

Events with $Q^2 \lesssim 1 GeV^2$ are referred to as photoproduction events. In the vector dominance model (VDM) the quasi-real photon fluctuates into a low mass vector meson (mainly ρ^0, ω and ϕ) which in turn interacts with the proton yielding similar event shapes as in hadron-hadron collisions. The transition between DIS and photoproduction is naturally not a sharp one and studies of that transition region are of great interest.

[1] "Forward" in the ZEUS frame is defined as the direction of the incoming proton. This corresponds to positive values of the pseudorapidity $\eta = -\ln(\tan(\frac{\theta}{2}))$ (see section 4.2.2), where θ is the polar angle with respect to the incident proton direction. "Backward" is therefore associated with the incident electron or positron direction and negative pseudorapidity η.

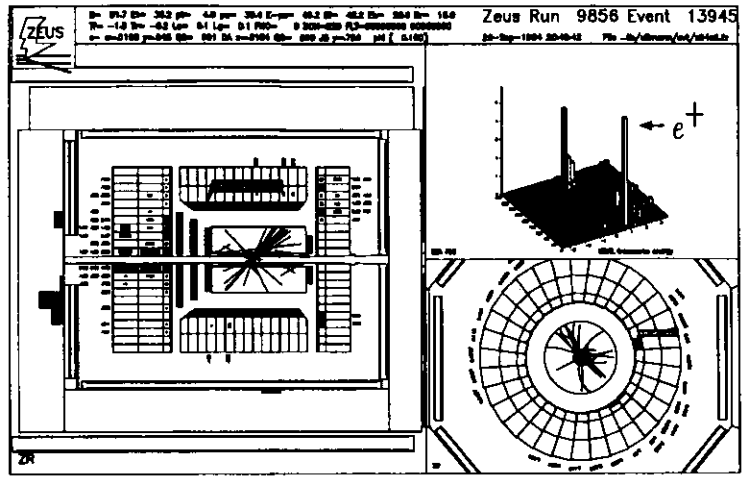

Figure 2.5: *Typical ZEUS event display of a DIS event. The scattered positron is reconstructed in the barrel calorimeter with an energy of $E_{e'} = 9.69 GeV$. The four-momentum transfer in this event is $Q^2 \sim 900 GeV^2$ at a Bjorken $x \sim 0.01$.*

In the electroweak theory the prediction of the coupling strength for the photon and the Z^0, e and g_W respectively, are of the same order $g_W \approx e$. The cross sections differ therefore only by a propagator term $\propto 1/(Q^2 + m^2_{Boson})^2$. Keeping in mind that the mass of the Z^0 is $\approx 91\, GeV$ this predicts that the interaction via γ exchange will dominate strongly up to $Q^2 \approx \mathcal{O}(10000\, GeV^2)$. In the Q^2 range studied in this thesis the contribution from Z^0 exchange is of order 1 %.

2.5 Diffractive processes in DIS

Elastic pp and $p\bar{p}$ scattering at large centre of mass energies exhibit classical diffraction patterns similar to intensity distributions of light scattered by a circular aperture. Aside from the elastic peak generated by the simplest type of elastic $pp \to pp$ scattering secondary diffraction peaks appear, associated with processes of type $pp \to pX$. The typical interaction radius of the strong interaction ($R \cong 1/m_\pi$) is in agreement

with the radius estimated from the diffraction patterns. More similarities between the elastic scattering and diffraction show up in the study of the cross section as a function of M_x^2/s (M_x is the invariant mass of the dissociated system X) which can be interpreted as the forward momentum transfer of the interaction. By analogy with optics, where the diffraction pattern gets more pronounced for wavelengths larger than the aperture radius, the cross section rises for decreasing momentum transfer q with $k = 1/q \gtrsim R$. Again R is in agreement with the typical radius of strong interactions.The rise gets more pronounced with increasing s since higher masses M_x^2 get incorporated into this "diffractive" region. From these analogies with the classical diffraction of light, events of type $pp \to pX$ were named "diffractive" events.

In early attempts to find a theory describing the results of hadron scattering processes the Regge theory was developed based on the study of the partial wave scattering amplitudes T in the complex angular momentum plane. The behaviour of the (differential) cross section as functions of s (and t,M_x^2) could be expressed in terms of Regge trajectories. The Regge trajectories are universal functions (*i.e.* independent of the scattered hadrons) depending only on the quantum numbers (angular momentum L , Isospin I (I_3), Spin S and Baryon number B) of the particle exchanged in the scattering process. This framework provides a simple explanation for the diffractive processes in identifying them with the "Pomeranchuk trajectory". This trajectory carries the internal quantum numbers of the vacuum and represents the exchange of a colourless virtual particle called the "pomeron". Besides the explanation for the behaviour of the diffractive cross sections as mentioned above it predicts a constant contribution to the total cross section of the scattering process while non-diffractive processes fall with inverse powers of s. Later on the definition of diffraction was generalized to all events that proceed via the exchange of a pomeron. Therefore double diffractive processes, where both hadrons dissociate are included too. The nature of the pomeron and its QCD structure - if existing - remain unknown and has to be measured by experiments. The observed rise of the total cross sections for centre of mass energies above $\sim 200\,GeV$ can be attributed to the contribution of diffractive

processes (including double diffractive processes).

See [Gou83] for a more comprehensive review of related pp scattering studies and the introduction to the diffractive theory. [Per74] gives an introduction to Regge theory.

The diffractive nature of a scattering event is not always immediately apparent from the measurement since it is difficult to fully contain the event in the detector and therefore to resolve the hadronic content of the scattered systems. However, the requirement that the diffractive scattering processes have to proceed via a colourless pomeron (whether of Regge type or not) gives rise to a property that helps to distinguish them from non-diffractive scattering processes. The two interacting hadrons that exchange the pomeron are not colour-connected and their dissociation proceeds independently. This leads usually to two well separated final state systems with a "gap" of very low or no hadronic activity in between. The gap width is usually measured as an angular separation in units of pseudorapidity η. In case of the exchange of a coloured object, on the other hand, the two systems are colour-connected and radiation processes fill this gap region. Diffractive processes are therefore much more likely to have a large rapidity gap than non-diffractive processes. Often diffractive events are referred to as "Large Rapidity Gap events" and non-diffractive events as events with no rapidity gap. This classification is not completely correct since statistical fluctuations might lead to non-diffractive events with a large rapidity gap while not all diffractive events will have one.

At HERA the two experiments H1 and ZEUS study the properties of diffractive processes in either DIS ([Der95e], [Ahm94a], [Ahm94b], [Der95a]) or in photoproduction ([Der95d],[Der96b], [Der95b]).

In DIS events at HERA the scattered proton (or proton remnant) escapes usually undetected in the forward beam pipe. The rapidity gap events are therefore observed as events with no hadronic activity in the forward region and the width of the rapidity gap is defined as η_{max}, the angle of the most forward energy deposition in the calorimeter in units of pseudorapidity. Figure 2.6 shows a schematic diagram for the

event topology for a diffractive type event, figure 2.7 shows a ZEUS event display of a typical event with a large rapidity gap.

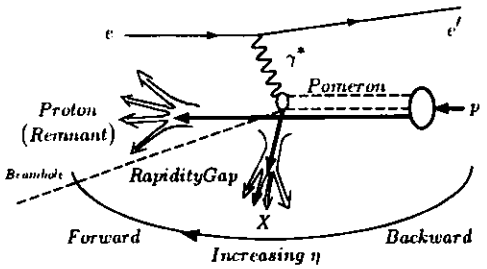

Figure 2.6: *Schematic diagram for a diffractive DIS event.*

HERA kinematics allow diffractive scattering processes with high momentum transfers in which the photon probes the structure of the pomeron. The study of properties of diffractive processes in DIS with the ZEUS detector thus will help to understand the nature of the pomeron.

Two models for the diffractive (pomeron) scattering in DIS have been tested extensively and found useful in order to reproduce properties of diffractive properties as measured at HERA. They are based on different assumptions about the structure of the pomeron and the scattering mechanism, as explained in the following sections 2.5.1 and 2.5.2.

2.5.1 Ingelman-Schlein

In the Ingelman-Schlein-model the diffractive process is understood as the interaction between a hadron-like quasi-particle which is emitted from the proton and a virtual photon, coming from the electron. Figure 2.8 shows a schematic illustration of this picture . The hadron-like quasi-particle is identified as the pomeron of the Regge theory. The pomeron-emission from the proton is considered as being independent of the subsequent pomeron-photon interaction and is described by a universal pomeron flux. The proton may or may not dissociate after emission of the pomeron. The

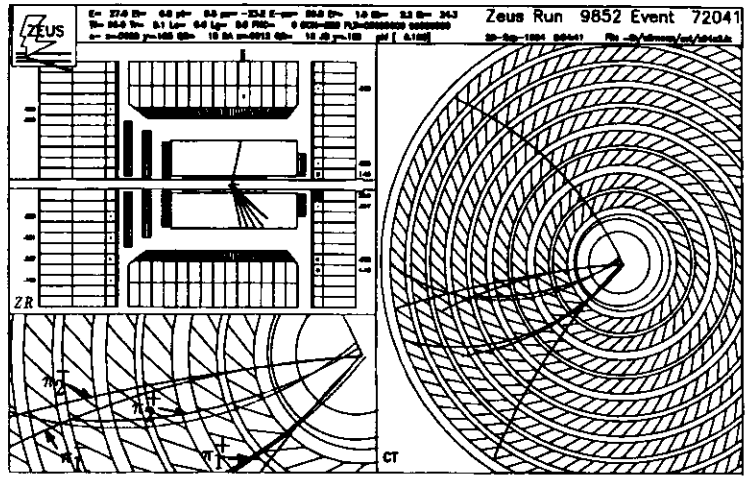

Figure 2.7: *Typical ZEUS event display of a diffractive DIS type event. A positron with energy $E_{e'} = 22.5\,GeV$ is reconstructed in the rear calorimeter close to the beam pipe. The measured rapidity gap is $\eta_{max} = -0.17$.*

photon emission by the electron is described by a photon flux. With increasing virtuality of the photon the internal structure of the pomeron can be probed. The idea of the pomeron structure function is introduced by analogy to the proton structure function. The hard scattering sub-process can then be interpreted as the interaction between the exchanged photon and a parton, carrying a fraction $x_{\mathcal{P}}$ of the pomeron momentum. The remaining pomeron momentum fraction $(1 - x_{\mathcal{P}})$ is carried by the pomeron remnant X. For the parton distribution inside the pomeron different assumptions can be made. One can postulate a hard distribution, where only few partons carry the pomeron momentum or a soft one, where many partons share the momentum of the pomeron. The former case is often referred to as a "valence-like", the latter as a "sea-like" momentum distribution.

This model has been suggested by G. Ingelman and P. E. Schlein ([Ing85]). First evidence for partonic structure was thereafter detected by the UA8 experiment ([Bon88])

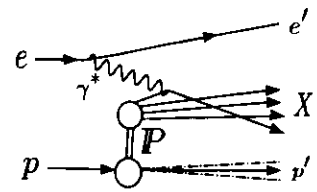

Figure 2.8: *Schematic illustration of a diffractive DIS scattering in the Ingelman-Schlein picture.*

at the CERN SPS collider facility, using $p\bar{p}$ collisions at centre of mass energies of $\sqrt{s} = 630\,GeV$. The model has been tested with different assumptions on the momentum distribution of the partons inside the pomeron, suggesting a hard parton distribution. However, the experiment could not distinguish between gluonic or quarkonic parton content of the pomeron[1]. Recent results from the ZEUS experiment found evidence for gluonic content of the pomeron and indicate that between 30 % and 80 % of the pomeron momentum carried by partons is due to hard gluons ([Der95b]). Other studies ([Bar94]) have ruled out the soft parton distribution for diffractive ep scattering.

2.5.2 Nikolaev-Zakharov

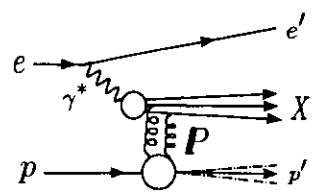

Figure 2.9: *Schematic illustration of a diffractive DIS scattering in the Nikolaev-Zakharov picture.*

The Nikolaev-Zakharov-model is often referred to as photon diffractive dissociation on the proton : the incoming γ fluctuates into $q\bar{q}$ or $q\bar{q}g$ Fock states that interact through

[1]The result is based on jet analysis. However, it is not possible to distinguish between a quark jet or gluon jet.

their colour dipole moment with a pomeron. Here the pomeron is understood not as a particle but rather as a coupling mechanism. To lowest order it can be pictured as a colour singlet system of two noninteracting and seemingly uncorrelated gluons emitted with different flux factors from the proton ([Low75],[Nus75],[Nik92]). Figure 2.9 shows a schematic illustration of this picture. The factorization and the idea of a pomeron structure function are not applicable in this theory. The diffractive DIS scattering is described in perturbative QCD by the BFKL equation (see section 2.3). In this frame it has been shown ([Nik94]) that the hadron-like behaviour of the pomeron ((virtual) photon-pomeron scattering exhibits typical features of hadronic two body reactions) can be understood as an asymptotic feature allowing one to derive an equivalent to a pomeron structure function:

$$\beta P_{NZ}(\beta, Q^2) = C \cdot (A \cdot \beta(1-\beta)^2 + B \cdot (1-\beta)^3) \tag{2.5}$$

where $\beta = x/x_{\mathcal{P}}$. Here, in contrast to the Ingelman-Schlein-model, $x_{\mathcal{P}}$ is the fraction of the proton longitudinal momentum carried by the pomeron. x is the Bjorken scaling variable. The first term of this two component structure function is referred to as a "hard" component. It can be interpreted as the interaction with the $q\bar{q}$-state of the photon. The second term reflects the "soft" contribution of the interaction with the $q\bar{q}g$-state of the photon. The factors A and B give the relative size of their contribution and are predicted by the model to be 65% and 35% respectively[1]. C represents an overall normalization factor.

An important aspect of this model is the prediction that photon dissociative diffraction contributes $\sim$ 15% to the DIS cross section.

Deep inelastic scattering events of non-diffractive and diffractive type have been observed with the ZEUS detector at HERA. The aim of this dissertation is to study in detail the production of neutral strange particles in these events in order to shed light on the underlying production mechanisms.

[1]These calculations include an integration over Q^2 and incorporate an uncertainty of about 30%

3

THE EXPERIMENT

3.1 The HERA Collider Facility

The hadron electron storage ring HERA[1] is situated in Hamburg, Germany, at the high energy physics research institute DESY[2]. The facility is designed to collide counter-rotating beams of 820 GeV protons and 30 GeV electrons or positrons, resulting in a center-of-mass energy of $\sqrt{s} = 314\ GeV$. The beams are bunched into 220 equidistant buckets, which are brought to collision at a bunch crossing rate of $\sim 10.5\,MHz$. A varying number of buckets, so called pilot bunches, are left empty for background studies. HERA kinematics allow four-momentum transfer squares in scattering processes up to $Q^2_{max} = 10^5\,GeV^2$. Compared to existing lepton-nucleon fixed target experiments this means an increase of two orders in magnitude. A $50\,TeV$ electron beam on a fixed proton target would be required to reach such high transfers of Q^2. HERA is the first and only ep collider in the world and a whole new kinematic range is now accessible for detailed studies.

The HERA collider facility is installed in a 6.3 km circumference tunnel, $10-25\ m$ underground. The large difference between the electron and proton masses urged to use two different magnet and RF systems to guide the beams in separate storage rings. Charged particles of mass m traveling with relativistic energies E in a circular orbit of radius R suffer energy loss $\propto E^4 m^{-4} R^{-1}$ per revolution due to synchrotron radiation. While this effect is negligible for the proton beam, the cost to compensate

[1] Abbreviation for German : Hadron Elektron Ring Anlage

[2] Abbreviation for German : Deutsches Elektronen SYnchrotron

the resulting energy loss limits the electron or positron beam energy. On the other hand, superconducting magnets are necessary to bend the proton beam on the circular orbit while for the lower energy electrons, conventional magnets are sufficient. This limits the proton beam energy.

A highly sophisticated preacceleration and injection scheme, as shown in figure 3.1, is needed for HERA. It uses other already existing accelerator facilities of former lower energy experiments :

- The electrons (positrons) are accelerated from 50 MeV to 450 MeV in the linear accelerator LINAC-II (LINAC-I), then injected into the storage ring PIA where they are accumulated into a single bunch ($\sim 60\,mA$). From there they get injected into DESY-II synchrotron where they reach energies of $\sim 7\,GeV$. The PETRA-II ring brings them up to $\sim 14\,GeV$, which they need to be finally transferred into the HERA ring.

- To produce a proton beam, H^- ions are accelerated in LINAC-III to $\sim 50\,MeV$ and injected into the (rebuilt) DESY-III synchrotron whereupon the electrons are stripped, leaving bare protons. These are then accelerated to $7.5\,GeV$ and transferred to PETRA-II. Here they attain an energy of $40\,GeV$ before they are injected into the HERA ring.

The HERA project was approved in 1983 and construction began with contributions from many countries including Canada. The electron ring was finished in July 1989, the proton ring was commissioned in November 1990. In October 1991 the first ep interactions were observed, regular data taking started in summer 1992 with two experiments H1 and ZEUS located in the north and south interaction region respectively, where the beams collide head-on. Since then an ongoing progress in completing the machine and understanding its performance has led to a steady increase in delivering luminosity to the experiments, giving the basis for a lot of exciting studies in a wide range of topics. HERA luminosity delivery to the experiments is assigned for a 6 to 8 month run period each year, followed by a winter shutdown. For most of the

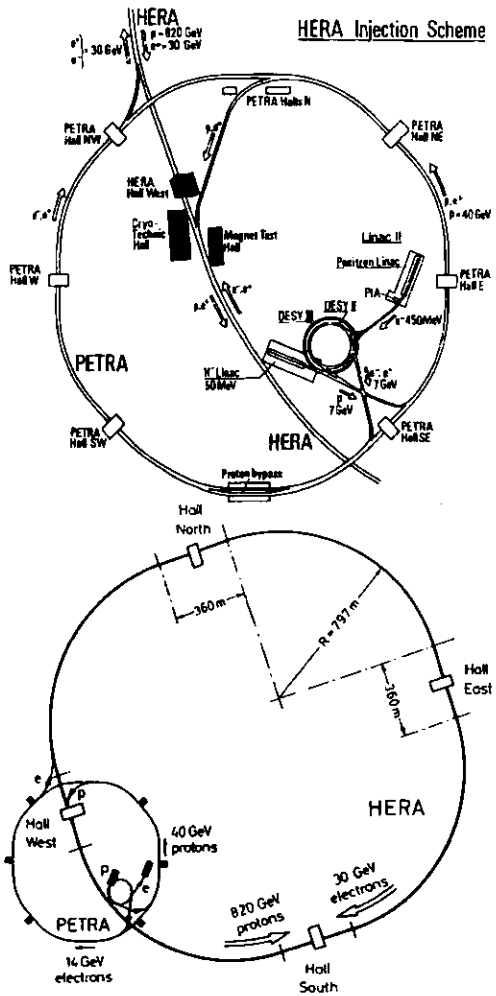

Figure 3.1: *The HERA injection scheme*

1994 run period, a positron beam was used instead of an electron beam (in fact the data underlying the studies in this thesis are using the data of the 'positron runs'). Some of the design parameters and their values achieved for the different run periods are summarized in table 3.1.

Parameter	Design	1992	1993	1994 e^-p	1994 e^+p
ep CM energy $[GeV]$	314	296	296	300	300
Proton energy $[GeV]$	820	820	820	820	820
Electron (Positron) energy $[GeV]$	30	26.67	26.7	27.5	27.5
Number of buckets	220	220	220	220	220
Number of colliding bunches	~ 200	9	84	110	153
Number of pilot bunches ($e + p$)	10+10	1+1	10+6	15+17	15+17
e circulating current (mA)	58	2	7-15	5-20	20-33
p circulating current (mA)	160	2	12-15	20-40	30-55
Maximum luminosity $(10^{30} cm^{-2} s^{-1})$	16.0	0.22	1.5	1.5	5.23
Integrated luminosity $[pb^{-1}]/year$	100.0	0.06	1.1	1.1	5.1

Table 3.1: ***HERA design and progress table***

Two further experiments, HERMES ([HER90]) and HERA-B ([HER94]) using the east and west experimental areas respectively are in construction or testing phase. Both these experiments are designed as fixed target experiments. HERMES uses interactions of the HERA electron beam halo and internal targets to study the spin dependent structure functions of proton and neutron. HERA-B on the other hand will use internal targets and the HERA proton beam halo as a B hadron factory in order to study possible CP violation in the B system.

3.2 *Overview of the ZEUS Detector*

The highly asymmetric colliding beam energies imply a strong boost of the final state particles into the the direction of the incident proton which is therefore called

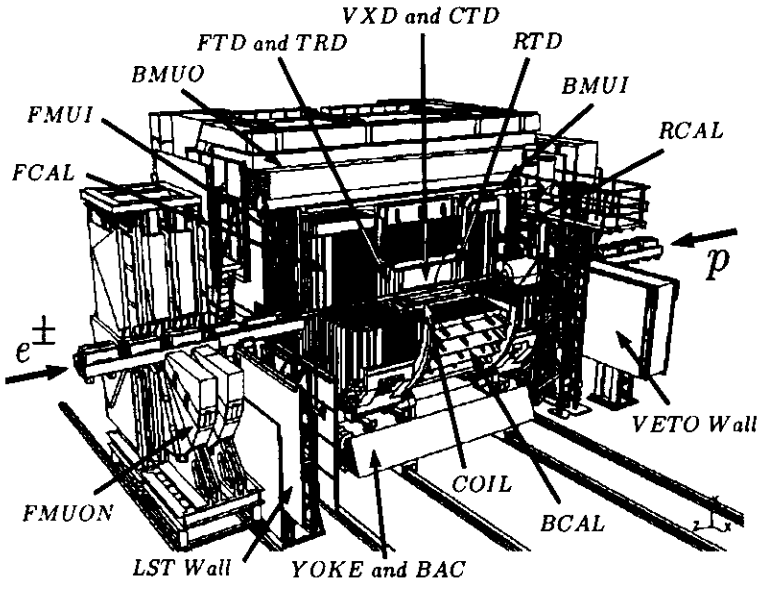

Figure 3.2: *Schematic view of the central components of the ZEUS detector.*

the forward direction (or downstream). To allow measurements of the kinematic variables accurately over the whole kinematic range offered by the HERA machine a special emphasis is placed on the forward direction reflected in the asymmetric layout of the ZEUS detector. To be able to give descriptions of event topologies in an unambiguous way a right handed coordinate system has been defined for the ZEUS analyses : the positive z-axis is defined as the incident proton beam direction, the x-coordinate points towards the ring centre and the y-coordinate upwards. Polar angles θ and azimuthal angles ϕ are measured with respect to the z-axis and x-axis respectively.

Figure 3.2 shows a schematic picture of the main components of the ZEUS detector. In this view the proton beam enters the detector from the right side while the electron (positron) beam comes from the left. The detector components are built

hermetically around the interaction point minimizing particle losses. In the following subsections I will give a short overview of the detector components and their purpose. Abbreviations follow the standard ZEUS naming convention.

3.2.1 *The Inner Tracking System*

At the interaction zone the beam pipe is surrounded by a tracking system consisting of the following components :

- The central tracking detector (CTD) is a drift chamber which can reconstruct charged particle paths within an angular range $15° < \theta < 164°$. This detector part is essential to the analysis in this thesis and therefore will be described in more detail in section 3.3.

- The vertex detector (VXD) is a cylindrical drift chamber with an active length of $159\,cm$. It is build from carbon fiber and has an inner and outer radius of $9.9\,cm$ and $15.9\,cm$ respectively. It consists of 120 cells with 12 sense wires each. DME (dimethyl ether) has been chosen as working gas because of its drift and quenching properties. The achieved spatial resolution is around $50\,\mu m$ reaching roughly $35\,\mu m$ in the central drift region. The purpose of the VXD is to improve the momentum and angular resolution of the charged tracks in conjunction with the other tracking devices. This improves also the measurement of the interaction point and of the distance of closest approach to the interaction point by a factor of $2 - 3$ compared to the CTD measurement alone. The latter allows one to reconstruct secondary vertices close to the interaction point which are associated with the decay of short lived particles.

- The forward and rear tracking detectors (FTD and RTD respectively) are planar drift chambers perpendicular to the beam. There are three FTD modules and one RTD module with identical design. Each module has 3 layers of wires with orientations of $-120°, 0°$ and $120°$ with respect to the x-axis providing different stereo views. The FTD covers the angular range (with respect to the nominal interaction point) from $7.5° < \theta < 28°$, the RTD from $160° < \theta < 170°$.

In the 1994 run period these detectors were not yet fully instrumented and were in the readout chain for testing purposes only. Thus no FTD and RTD data are available for the analysis in this thesis. In the 1995 running period the complete tracking is expected to provide tracking information over the maximum available angular range.

- The transition radiation detectors (TRD) are sandwiched in pairs between the three FTD modules. Each of the 4 modules is 10 cm deep and consists of a 7 cm deep radiator of polypropylene fleece followed by a planar drift chamber. The purpose of the TRD is the separation of electrons and pions. The design efficiency to identify electrons with energies between 1 and 30 GeV is around 90 % with a purity of around 95 %. Like the FTD and RTD modules the TRD detectors were not completed for the 1994 run period but are included in the 1995 data taking.

The tracking system is surrounded by a cylindrical superconducting solenoid (COIL) providing a 1.43 T magnetic field. The latter forces the charged particles on helix paths while they traverse the tracking system. The curvature of these helices is used to calculate the particle momenta. Particle identification can proceed via specific energy loss, dE/dx, in the CTD. To calculate the specific energy loss, information about pulse heights for the hits along the track, as well as information about the gas pressure and temperature is required. In the 1994 running period this information was only partly available (CTD only) and therefore dE/dx is not used in this analysis.

3.2.2 The Calorimeter

To measure the energies of the particles the tracking system is surrounded hermetically by the high resolution uranium-scintillator sampling calorimeter (UCAL) leaving only a 20 $cm \times 20$ cm hole in the forward and backward region where the beampipe enters the inner detector. It is subdivided into three main building blocks FCAL, BCAL and RCAL denoting forward, barrel and rear calorimeter. Each of these blocks is built up from modules, divided into towers with a surface area of 20 $cm \times 20$ cm for the

FCAL and RCAL and 20 $cm \times 24$ cm for the BCAL, respectively. In the longitudinal direction each BCAL and FCAL tower is subdivided in 3 sections, the inner EMC (electromagnetic calorimeter) section and the two outer HAC (hadronic calorimeter) sections. The RCAL towers are divided into one EMC and one HAC section. Towers at the edge of FCAL and RCAL that are shadowed by BCAL EMC sections have only HAC sections. The EMC sections are segmented into 4 cells of 5 $cm \times 20$ cm for FCAL, 4 cells of 5 $cm \times 24$ cm for BCAL and 2 cells of 10 $cm \times 20$ cm for RCAL. Two wavelength shifter light guides at both (x-) boundaries of each EMC cell and each HAC section transport the scintillator light output to photomultipliers. A total of over 11 thousand readout channels provide information about energy depositions and their absolute positions. The angular coverage (again with respect to the nominal interaction point) is $2.2° < \theta < 39.9°$ for the FCAL, $36.7° < \theta < 129.1°$ for BCAL and $128.1° < \theta < 176.5°$ for BCAL. The depths of the calorimeter components have been chosen such that they will contain 95% of the energy of 90% of the jets. This corresponds to 7 λ (FCAL), 5 λ (BCAL) and 4 λ (RCAL), where $\lambda \simeq 21$ cm denotes 1 hadronic interaction length for the agglomerate of scintillator and absorber materials. The depth of the EMC section corresponds to about 25 radiation lengths X_0 ($1\,X_0 \simeq 0.75$ cm), enough to fully contain electromagnetic showers. The ZEUS calorimeter is a compensating calorimeter. In tests at the X5 test beam of the CERN-SPS a ratio $e/h = 1.00 \pm 0.05$ and an energy resolution of $\sigma/E = 18.0\%/\sqrt{E}$ for electromagnetic showers and $\sigma/E = 35.5\%/\sqrt{E}$ for hadronic showers have been determined ([And91]), where E is measured in GeV. Half of the FCAL and RCAL system was constructed by the participating Canadian groups.

To identify electrons inside jets and to improve the position resolution of showers an additional device called HES (hadron electron separator) is built into the calorimeter. It consists of a plane of silicon diode arrays, each diode having an active surface of 3 $cm \times 3$ cm. The plane is inserted at 3.3 X_0 in the RCAL. The insertion of HES planes in FCAL and BCAL are foreseen at 6.3 X_0 and 3.3 X_0, respectively. At this depth the narrow electromagnetic showers reach their maximum and therefore give rise to large

signals in the HES diodes. Hadronic showers, however, are much wider and generally reach their maximum at greater depths. The signal in the HES resembles more a signal from minimum ionizing particles.

3.2.3 *Resolution Improving Devices*

Particles on their way from the interaction point towards the calorimeter have to pass inactive material, such as the beam pipe, the superconducting solenoid, detector support structures, readout electronics and cablings of the tracking detectors. This will generally give rise to energy loss and pre-showering in case of interactions with this material. Electrons from converting photons can be used to study inactive material ([Koe94]) that can reach a depth of up to $\sim 4.4\,X_0$. A complete modeling of all of these inactive materials in the detector simulation is neither possible (*i.e.* cable bundles will never keep their exact position after closing the detector) nor intended. Therefore the event reconstruction cannot correct for these effects and the calorimeter will measure too low energies. Furthermore the effect will be energy dependent and different for hadronic and electromagnetic particles. This therefore will cause an effective degradation of the e/h ratio and lead to systematic effects in the reconstruction of the kinematic variables. To cope for this deficiency a PRESAMPLER has been designed ([Der94c]), consisting of a layer of scintillator tiles. They are installed in front of the FCAL (RCAL) and cover the area that is not in overlap with the BCAL. This corresponds to roughly 60% (70%) of the inner towers for FCAL (RCAL). The segmentation of the scintillators follows the tower scheme of the modules, each segment is read out via a wave length shifter fibre connected to a photomultiplier. The energy correction is done on an event to event basis, using the energy dependent correlation between true energy and energies measured in the presampler and calorimeter. Different corrections are applied for hadronic and electromagnetic particles or showers, identified as such with the help of HES, CTD or UCAL information. Tests with Monte Carlo simulations showed that a significant improvement in the energy resolution and reconstruction of the kinematic variables can be achieved ([Vre94]). In 1994 an FCAL prototype presampler was partially in

the readout for testing purposes only, with the beginning of the run period 1995 both FCAL and RCAL presamplers were included in the standard readout configuration. An equivalent device for BCAL is under discussion.

Since the 1994 run the SRTD (small angle rear tracking detector) has been installed. It consists of two orthogonal layers of SCSN-38 scintillator strips arranged in 4 quadrants covering a total of $68\,cm \times 68\,cm$ minus the $20\,cm \times 20\,cm$ hole of the beam pipe. This corresponds roughly to the ring of the 8 innermost towers of the RCAL. The angular coverage is $170° < \theta < 175°$. Each strip is $10\,mm$ wide, $5\,mm$ thick and either $240\,mm$ or $440\,mm$ long leading to a total of 272 channels that are connected to photomultipliers using optical fibres. The SRTD fulfills several purposes. First of all it allows the electron position reconstruction with a resolution $\sigma_{x,y} = 2.7\,mm$, allowing an accurate reconstruction of the kinematic variables in the low x and Q^2 region. Furthermore it can be used in combination with the tracking detector to extend track reconstruction towards large angles. Like the PRESAMPLER it can be used to correct for energy loss in inactive material and recognizes preshowering of particles. For the trigger it provides a fast timing information.

Since 1995 a further small angle detector is included into the central detector : the BPC (beam pipe calorimeter). It consists of two tungsten-scintillator electromagnetic sampling calorimeters BPC North and BPC South, positioned directly behind the RCAL ($z = -300\,cm$) aside the beam pipe. Both are $26\,X_0$ deep, with a veto counter at the back. The scintillator strip planes alternate in x,y orientation to allow a position measurement with 15 readout channels in x for BPC North, 11 channels for BPC South and 16 channels each in y. Due to its position it allows one to identify electrons at very small scattering angles of interactions at low Q^2 and x (roughly $0.1\,GeV^2 < Q^2 < 1\,GeV^2$ and $10^{-5} < x < 10^{-4}$)

3.2.4 *Backing Calorimeter and Muon Detectors*

To return the flux of the COIL the calorimeter is surrounded by an instrumented iron return YOKE. It consists of an octagonal cylinder that is closed with endcaps on either side. The BAC (backing calorimeter) consists of aluminium proportional tubes

filled with $Ar : CO_2$ inserted in cutouts of the YOKE. Its purpose is to measure the leakage energy of hadron showers from UCAL. The achieved energy resolution is around $\sim 100\%/\sqrt{E(GeV)}$. Furthermore the YOKE itself is magnetized ($1.6\,T$, field lines along beam line axis). Therefore it forces the muons that pass through UCAL onto curved paths allowing a momentum measurement in the muon detectors, another conglomerate of tracking chambers. There are muon detectors on the inside of the YOKE. Depending on their location, in the forward, barrel and rear region, they are called FMUI, BMUI and RMUI, respectively. On the outside of the YOKE there are are (with similar name convention) BMUO and RMUO of similar type and the FMUON system in the forward direction. The latter consists of a combination of planar drift chambers, LST (limited streamer tubes) planes, a time of flight counter and two magnetized iron toroids and allows muon identification down to very small angles. There are no muon chambers around the bottom part of the YOKE, here the BAC is instrumented with special cathode pads that allow the measurement of the muon trajectories.

3.2.5 Background Vetoing Devices

The VETO WALL is located upstream near the tunnel exit (centre at $z = -727\,cm$). Its main purpose is to protect the detector from the high background of particles produced in beam gas interactions. The main part therefore consists of an iron wall as passive absorber. To be able to veto events initiated from particles passing through the VETO WALL the iron wall is sandwiched between two scintillator hodoscopes. Each of the hodoscopes is built up from scintillator strips arranged in 2 planes perpendicular to the beam axis. The relative orientation of the strips in the two planes is perpendicular. At both ends of each strip is a photomultiplier, a coincidence of their signals is required to be accepted as a trigger signal. The VETO WALL vetoes an event if corresponding areas in both hodoscopes have a trigger signal.

To reduce high rates due to events originating from synchroton radiation, beam gas or beam wall related interactions a set of colliminators is installed at various positions close to the beam pipe. In order to monitor beam characteristics and to reject

proton beam gas related background events the C5 counter is installed downstream the RCAL. The C5 consists of four scintillators which measure the arrival time of particles with an accuracy better than $1\,ns$.

3.2.6 Luminosity Detectors (LUMI)

Beside the central components mentioned so far there are more detector components located inside the HERA tunnel. Essential to any cross section calculation is the knowledge of the integrated luminosity corresponding to the acquired data. The luminosity $\mathcal{L}$ at collider experiments is defined as :

$$\mathcal{L} = fn\frac{N_1 N_2}{A}$$

where f is the bunch crossing rate, n is the number of bunches in either beam, N_1, N_2 are the numbers of particles in each bunch and A is the cross-sectional area of the beams (assuming them to overlap completely). Common units for luminosities at collider experiments are $\sim pb^{-1}/year$, where $1\,pb = 10^{-40}m^2$. For a known luminosity the cross section σ of a process under study can be calculated from its measured rate R :

$$\sigma = \frac{R}{\mathcal{L}}$$

ZEUS uses the inversion of this formula to measure the luminosity from the rate of hard bremsstrahlung photons at small angles from the well understood Bethe-Heitler process $ep \rightarrow e'p\gamma$. The photons travel in the proton beampipe until the latter curves at $z = -92\,m$. The photons exit the beampipe through a window and are detected at $z = -108\,m$ in a lead scintillator calorimeter (LUMIG) which has an energy resolution of $\sigma(E)/E = 18.5\%/\sqrt{E(GeV)}$. To absorb the large flux of synchrotron radiation photons with energies usually lower than $50\,MeV$ a carbon filter is placed in front of LUMIG. To detect the scattered electron, another electromagnetic calorimeter, LUMIE, is positioned at $z = -35\,m$. Electrons with energy lower than the nominal beam energy are bent differently by the magnets and leave the orbit. Scattered electrons with energies between 35 and 65 % of the nominal beam energy

can leave the beam pipe through a window and fall within the geometric acceptance of the LUMIE.

3.2.7 Small Angle Detectors

In the forward direction there are three more detectors to measure the scattered proton or its remnant at small angles.

1. The LPS (leading proton spectrometer) consists of 6 stations of Roman Pots at $z = 24, 41, 44, 63, 81, 90\,m$ that form together with the bending magnets of the HERA ring a high precision spectrometer for forward scattered protons.

2. The PRT (proton remnant tagger, [Des95]) consists of 7 pairs of rectangular scintillation counters surrounding the beam pipe. Two pairs, forming PRT1, are installed at $z = 5.15\,m$ in the gap between FCAL and the beam pipe. They cover an angular range of $6\,mrad < \theta < 26\,mrad$. The PRT2 consists of four pairs of scintillators that are installed at $z = 24.4\,m$ and a fifth pair at $z = 23.1\,m$. The latter covers a gap in the geometric acceptance due to a flange attached to the beam pipe. The overall acceptance of PRT2 is about $1.5\,mrad < \theta < 8\,mrad$. This detector was installed since the 1994 running period and is used to detect highly energetic charged particles that escape the central detector through the forward beam pipe.

3. To detect neutrons produced in the proton beam direction the FNC (forward neutron calorimeter) is installed at $z = 105\,m$ since the 1993 run period. Again, as in the case of LUMIG, the proton beam pipe curves and the charged particles are bent by magnets, neutrons exit the beam pipe undeflected.

3.3 The Central Tracking Detector CTD

The CTD is a cylindrical wire chamber with inner and outer radii of $16.2\,cm$ and $85.0\,cm$ respectively and a length of $241\,cm$. The active volume of the chamber, with inner and outer radii of $18.2\,cm$ and $79.4\,cm$ and a length of $205\,cm$ (range from

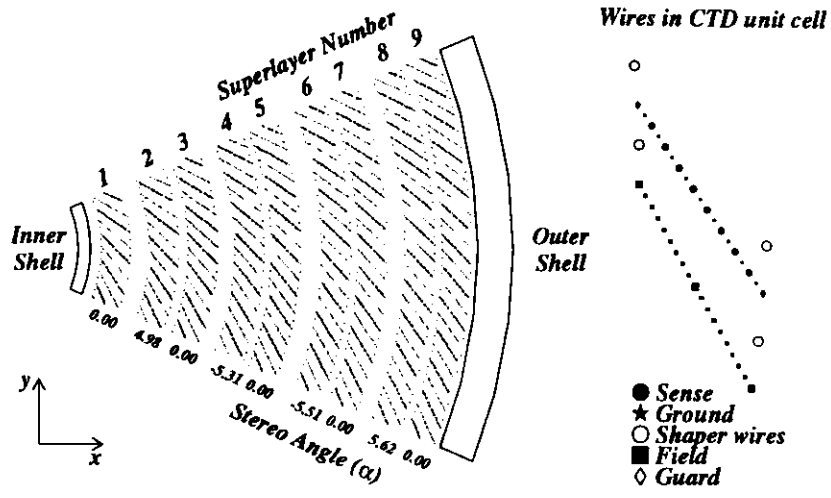

Figure 3.3: *xy-view of the wire arrangement in one octant of the CTD and the layout of one unit cell. The numbering conventions of the superlayers and the stereo angles of the wires within the superlayers are shown.*

$z = -100\,cm$ to $z = 105\,cm$ in the ZEUS coordinate system), is filled with a gas mixture of $Ar/CO_2/C_2H_6$. A total of 24192 wires, 19584 field wires and 4608 sense wires, are grouped into 72 cylindrical layers arranged into 9 so called superlayers. Each superlayer is divided into cells with 8 sense wires. The arrangement of field wires in each cell and the applied voltages are optimized to provide an uniform electric field vector over a mesh of points in the drift volume while minimizing electric forces on the sense wires. As charged particles pass through the CTD they ionize the gas mixture. The ionization electrons drift in the electric field of a cell towards the sense wires creating an avalanche of ionization near the wire. This induces an electric pulse in the sense wire (a "hit") which establishes that a charged particle has passed close by. All sense wires are read out and digitized with FADCs (Flash Analog to Digital Converter), providing drift times and pulse heights which are used to calculate a spatial coordinate on the charged particle's drift path. In the odd-numbered

"axial" superlayers the wires are parallel to the beam axis, even-numbered "stereo" superlayers are tilted by a stereo angle of about $\pm 5°$ in order to provide an additional z-measurement on the drift path. The achieved position resolution in the 1994 run period is $\sim 200\,\mu m$ in $r\phi$ and $\sim 2\,mm$ in z. The transverse momentum resolution for full length tracks in CTD and VXD is $\sigma(p_t)/p_t = \sqrt{(0.005 \cdot p_t(GeV))^2 + (0.016)^2}$. The sense wires in superlayer 1 and half of the sense wires in superlayers 3 and 5 are read out at both ends, providing a measurement on the z coordinate from the difference in the arriving time of the signals. The achieved resolution in "*ZbyT*" (z by timing) is $\sim 3\,cm$. Figure 3.3 shows the layout of wires of one octant of the CTD chamber. Table 3.2 summarizes some important specifications of the CTD.

3.4 *Finding Tracks and Event Vertex*

The analysis presented in this thesis is based on the measurement of charged tracks. This section will give a brief introduction to the parts of the track finding program VCTRAK, which are used in this analysis to find and reconstruct CTD tracks and the primary event vertex. More details about this program, which was originally developed for the online trigger system TLT (see section 6.2) and later adapted for offline physics reconstruction, can be found in [Har96].

The reconstruction of the tracks is done in three steps. In the first step, the "pattern recognition", tries to find arc trajectories in the xy-plane. A track candidate is started with a "track seed" in the outer part of the CTD. This seed can either consist of three hits in one axial superlayer or, towards large angles, an SRTD signal, three hits in the innermost axial superlayer SL1 and at least one *ZbyT*-measurement. For the run periods with a completed inner tracking detector, track seeds using hits in the FTD and RTD are foreseen. A broad "virtual hit" at the beam line is used to guide the trajectory inwards. On the way, additional hits are included to update the trajectory parameters with increasing precision. The resulting arc is then used for *ZbyT* and stereo pattern recognition. For arcs with *ZbyT* measurements along the trajectory, the latter are used for a coarse first estimate of the 3D trajectory, limiting

Volume, radius :	16.2 – 85.0 *cm* (overall)	18.2 – 79.4 *cm* (active)
length :	241.0 *cm* (overall)	205.0 *cm* (active)
Gas mixture :	$Ar/CO_2/C_2H_6$	85/8/7

9 superlayers, each with eight layers of sense wires
576 cells with 4608 sense wires and 19584 field wires

Superlayer	No. of cells	Mean stereo angle (°)	Cell center radius (*cm*)	θ range (°)
1	32	0	20.97	11.3 - 162.8
2	40	4.98	27.23	14.5 - 164.8
3	48	0	35.00	18.4 - 160.7
4	56	-5.31	41.30	21.5 - 157.3
5	64	0	48.73	24.9 - 154.0
6	72	-5.51	55.52	27.9 - 151.0
7	80	0	62.74	30.9 - 147.9
8	88	5.62	69.46	33.5 - 145.2
9	96	0	76.54	36.1 - 142.6

Table 3.2: *Parameters of the CTD*

the region to be searched for stereo hits. The *ZbyT* and stereo hits which superimpose on this trajectory provide the needed z information to describe the track as an ideal helix.

The second step, the "track prefit", corrects for systematic effects on the drift distance. The raw drift times are calculated assuming a planar drift approximation. However, variations in the magnetic field propagate into variations in the Lorentz angle, drift velocity and position. Correcting for these systematic effects improves the hit resolution and usually leads to the inclusion of more hits to a trajectory, thus improving the measurement of the track.

In the third step, the "track fit", each track candidate found in the previous pattern recognition (improved by prefit) is iteratively fitted to a 5 parameter helix model. The first iteration uses an estimation of the track momentum from the slope and curvature at the innermost hit and swimming through the magnetic field, therefore establishing a trajectory. The residuals of the hits along this trajectory are then calculated which are used to adjust the fit parameters for the next iteration. Usually one iteration suffices since the pattern recognition is fairly accurate.

The parameters of each reconstructed track (and further information as number of axial hits, *ZbyT* hits, etc.) are stored in the ADAMO[1] table VCTRHL.

To reconstruct the event vertex, only those reconstructed tracks are used that are compatible with the beam line (*i.e.* extend inwards to SL1 or VXD). An initial vertex position is obtained from a fit to the weighted mean of the distances of closest approach of the remaining tracks. Trajectories which contribute too much to the χ^2 of this fit are discarded until an acceptable fit quality is obtained. The resulting vertex position is then used as starting point for the full vertex fit which does not only determine the final vertex position but simultaneously constrains the remaining tracks to it, refitting direction and curvature. The coordinates of the event vertex as well as covariance matrix, χ^2 and number of degrees of freedom are stored in the VCTVTX tables, the parameters of the refitted tracks associated with the event vertex are stored in the VCTPAR tables.

[1] Aleph DAta MOdel : Entity-Relationship model for defining tabular data structures and for manipulating and validating them from analysis programs. This model has been adapted to the ZEUS data structure.

4

KINEMATICS IN DIS

4.1 *Event Kinematics*

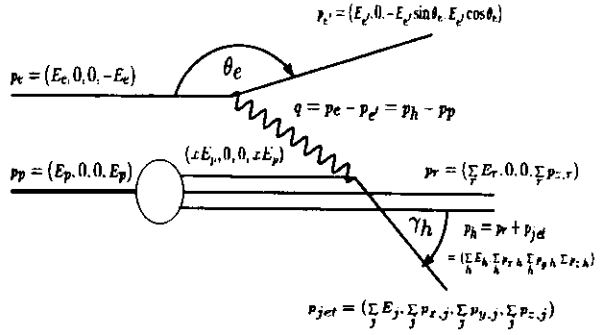

Figure 4.1: *Definitions of four-momenta and angles for basic NC DIS processes.*

The event kinematics in NC DIS can be fully described by three independent variables. The first is the *ep* centre of mass energy squared or total invariant mass squared

$$s = (p_e + p_p)^2 = m_p^2 + m_e^2 + 2 \cdot p_e \cdot p_p \tag{4.1}$$

where p_e and p_p denote the initial four-momentum vectors of the electron (or positron) and the proton respectively. Neglecting the masses, which is a very good approximation at HERA energies, leads to

$$s \simeq s - m_p^2 - m_e^2 = 2p_e \cdot p_p \sim 4E_eE_p \tag{4.2}$$

E_e, E_p refer to the colliding beam energies. Together with the energy of the scattered electron (positron) $E_{e'}$ and its scattering angle θ_e the process is unambiguously defined in terms of (double-differential) cross sections.

Still this choice of variables to describe the scattering process is very specific to the ZEUS experiment. $E_{e'}$ and θ_e are frame dependent and therefore don't allow an easy comparison with results from other experiments. It is therefore very common and convenient to describe the kinematics by Lorentz invariant variables Q^2, Bjorken x and y as introduced below:

Q^2 denotes the virtuality of the exchanged gauge boson and therefore defines the energy scale of the interaction. It can be expressed as either the negative square of the four-momentum difference of initial and final state electron (positron) or the negative square of four-momentum difference of incoming proton and the hadronic final state.

$$Q^2 = -q^2 = -(p_e - p_{e'})^2 \tag{4.3}$$
$$= -(p_h - p_p)^2$$

$$Q^2_{max} \simeq s \tag{4.4}$$

The so called Bjorken scaling variables x and y are defined as

$$x = \frac{-q^2}{2p_p \cdot q} \tag{4.5}$$

$$y = \frac{p_p \cdot q}{p_p \cdot p_e} = \frac{2p_p \cdot q}{s} \tag{4.6}$$

As easily verified x,y and Q^2 are related through

$$Q^2 = xys \tag{4.7}$$

In the quark-parton model x can be interpreted as the fraction of the proton's momentum carried by the struck quark, if one assumes that the parton transverse momenta inside the proton and the parton masses can be neglected compared to the Q^2. y can be interpreted as the fraction of the relative energy transferred from the electron to the proton in the proton rest frame. This becomes more obvious if one uses a different

notation, using ν, the lepton's energy loss in the proton rest frame:

$$\nu = \frac{p_p \cdot q}{m_p} \tag{4.8}$$
$$\nu_{max} = \frac{s}{2m_p}$$

With this y can be rewritten as

$$y = \frac{\nu}{\nu_{max}}$$
$$x = \frac{Q^2}{2m_p \cdot \nu}$$

By construction x and y (and Q^2) are scalars and can only vary in the limits $0 \leq x, y \leq 1$.

Considering the hadronic final state useful variables are the invariant mass squared of the total hadronic final state W^2:

$$W^2 = (p_p + q)^2 = m_p^2 - Q^2 + 2m_p \cdot \nu = m_p^2 + Q^2(\frac{1}{x} - 1) \tag{4.9}$$

and γ_H, the scattering angle of the scattered quark. Since the scattered quark will fragment into hadrons γ_H is equivalent to the scattering angle of the current jet.

4.2 *Reconstruction Methods of Kinematic Variables*

Several methods were developed to reconstruct Q^2,x and y based on the knowledge of the initial state and either the final state hadron and/or electron side. In the following subsections the three most common methods used in the ZEUS analysis will be introduced. In section 6.5 the resolution for the different methods will be discussed. The definitions of four-momenta and angles are as seen in figure 4.1.

The incoming four-momenta are given by the HERA collider (except for initial state radiation) whereas the four-momenta of the outgoing electron and hadrons have to be calculated from energy deposits in the calorimeter, possibly including particle identification. The actual values of the electron variables are calculated using so called electron finder algorithms which utilize electron specific shower properties in the calorimeter to distinguish electrons from other (hadronic) energy depositions. The

individual hadrons are often contained in jets and deposit their energy in the form of clusters. The energies E_h in the calorimeter cells and their position relative to the event vertex (θ_h) are used to determine the four-momentum of the hadronic system.

4.2.1 The Electron Method

For the electron method, only knowledge of the final state electron parameters is required, in addition to the energies of the initial states. Using the four-momentum of the outgoing electron and the scattering angle θ_e, as shown in figure 4.1, in combination with equations (4.3), (4.5) and (4.6) one easily finds the following reconstruction formulae :

$$Q^2_{el} = 2E_e E_{e'}(1+\cos\theta_e) = 4E_e E_{e'}\cos^2(\frac{\theta_e}{2}) \tag{4.10}$$

$$x_{el} = \frac{E_e}{E_p}\frac{E_{e'}(1+\cos\theta_e)}{2E_e - E_{e'}(1-\cos\theta_e)} = \frac{E_e}{E_p}\frac{E_{e'}\cos^2(\frac{\theta_e}{2})}{E_e - E_{e'}\sin^2(\frac{\theta_e}{2})} \tag{4.11}$$

$$y_{el} = 1 - \frac{E_{e'}}{2E_e}(1-\cos\theta_e) = 1 - \frac{E_{e'}}{E_e}\sin^2(\frac{\theta_e}{2}) \tag{4.12}$$

This method is very sensitive to initial state radiation where a photon is emitted by the incident electron, taking part of its four-momentum and therefore shifting the overall energy scale of the event.

In figure 4.2 a) and b) one sees several lines of constant $E_{e'}$ and θ_e, respectively, in the (x,Q^2) plane (lines of constant y are also included). A rough idea about the sensitivity of the reconstruction method to the reconstruction of $E_{e'}$ and θ_e can be deduced : in areas where the isolines are close together, errors in the electron energies or scattering angles do not have big effects, however, in areas where the isolines are separated, small errors might lead to relatively big errors in the reconstructed kinematic variables.

4.2.2 The Jaquet Blondel Method

In the Jaquet Blondel method (see [Jac79]) only knowledge of the energy of all final state hadrons is required in addition to the energies of the initial states. The formulae

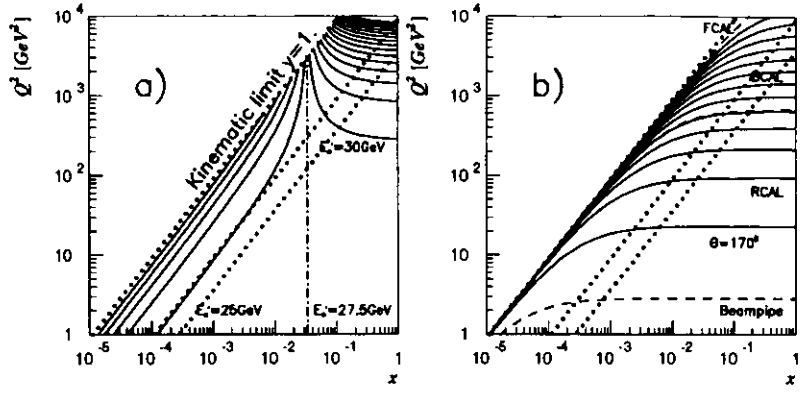

Figure 4.2: *Isolines of a) constant scattered electron energy $E_{e'}$ and b) constant scattering angles θ_e in the (x,Q^2)-phase space for electron and proton beam energies of 27.5 GeV and 820 GeV, respectively. The dotted lines are lines of constant y=1.0, 0.1, 0.04. The energy-isolines are drawn in steps of 5 GeV, the dashdotted line shows the special isoline for $E_{e'} = E_e = 27.5$ GeV, where x is independent of Q^2. The θ_e-isolines are shown in steps of 10°. The dashed lines indicate the coverage of the different calorimeter components.*

to calculate the kinematic variables read as follows :

$$y_{JB} = \frac{\sum_h (E_h - p_{z,h})}{2E_e} \tag{4.13}$$

$$Q^2_{JB} = \frac{(\sum_h p_{x,h})^2 + (\sum_h p_{y,h})^2}{1 - y_{JB}} \tag{4.14}$$

$$x_{JB} = \frac{Q^2_{JB}}{s y_{JB}} \tag{4.15}$$

where $\sum_h$ sums up all energy depositions in UCAL that are not associated with the scattered lepton. The advantage of this method is that it is robust against the missing energy due to proton remnant particles lost in the beam pipe since they only contribute to the sums as $\sim E_h(1-\cos(\theta_h))$ with $\theta_h \sim 0$. For the same reason, particles lost in the backward direction contribute strongly, however, they are also strongly suppressed due to the asymmetry of the colliding beams. Generally, y_{JB} will be shifted to lower values if particles are lost in the beam pipe.

Expressing these formulae in terms of energy and scattering angle, γ_H, of the

current jet one gets :

$$y_{JB} = \frac{E_{jet}}{E_e} \sin^2(\frac{\gamma_H}{2}) \tag{4.16}$$

$$Q^2_{JB} = \frac{E^2_{jet} \sin^2 \gamma_H}{1 - \frac{E_{jet}}{E_e} \sin^2(\frac{\gamma_H}{2})} \tag{4.17}$$

$$x_{JB} = \frac{\frac{E_{jet}}{E_p} \cos^2(\frac{\gamma_H}{2})}{1 - \frac{E_{jet}}{E_e} \sin^2(\frac{\gamma_H}{2})} \tag{4.18}$$

E_{jet} is the energy of the current jet and γ_H corresponds to the angle of a massless particle balancing the momentum vector of the outgoing electron (*i.e.* satisfying four-momentum conservation). In the naïve quark-parton model this angle corresponds to the angle of the struck quark. γ_H can be calculated from hadronic energies :

$$\cos \gamma_H = \frac{(\sum_h p_{x,h})^2 + (\sum_h p_{y,h})^2 - (\sum_h (E_h - p_{z,h})^2}{(\sum_h p_{x,h})^2 + (\sum_h p_{y,h})^2 + (\sum_h (E_h - p_{z,h}))^2} \tag{4.19}$$

In terms of y_{JB} and Q^2_{JB} (formulae 4.13 and 4.14) γ_H reads :

$$\cos \gamma_H = \frac{Q^2_{JB}(1 - y_{JB}) - (2E_e y_{JB})^2}{Q^2_{JB}(1 - y_{JB}) + (2E_e y_{JB})^2} \tag{4.20}$$

Also used in this thesis is γ_H in units of pseudorapidity :

$$\eta_H = -\ln(\tan(\frac{\gamma_H}{2})) \tag{4.21}$$

The pseudorapidity is an approximation ($p \gg m$) for the (true) rapidity Y which is defined as :

$$Y = \frac{1}{2} \ln(\frac{E + p_z}{E - p_z}) \tag{4.22}$$

E and (p_z) p denote the energy and (longitudinal) momentum of a particle or object of mass m. The (pseudo-) rapidity shows a simple behaviour under longitudinal transformations into a system which moves with velocity β :

$$Y^* = Y + \frac{1}{2} \ln(\frac{1 + \beta}{1 - \beta})$$

The transformation causes a shift $\Delta Y = Y^* - Y$, but leaves the shape of the rapidity distribution unchanged. This allows an easy comparison of rapidity distributions as measured in fixed target experiments with results from collider experiments.

A simple way to reconstruct E_{jet} from the hadronic energies (all energy depositions that are not associated with the scattered lepton) is to remove the proton remnant through a cone cut around the forward beam pipe. As mentioned above, contributions from particles with small angles with respect to the beam pipe are strongly suppressed, but depending on the opening angle of the cone a significant systematic effect might be introduced. A thorough study of the latter is necessary. A more sophisticated determination of E_{jet} and γ_H could proceed via jet finding algorithms.

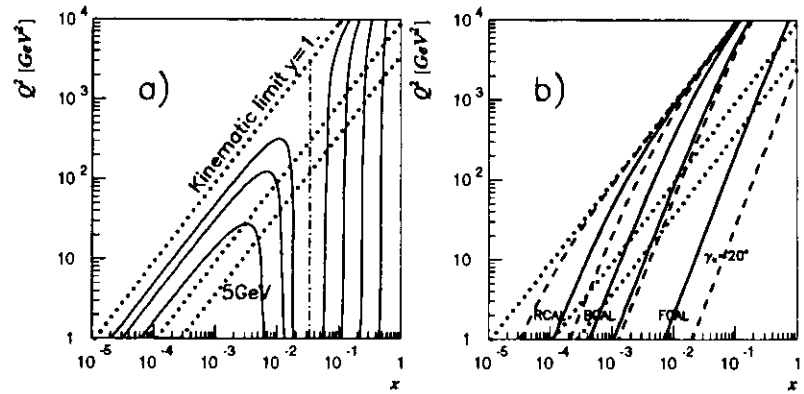

Figure 4.3: *Isolines of a) constant current jet energy E_{jet} and b) constant current jet scattering angle γ_H in the (x,Q^2)-phase space for electron and proton beam energies of 27.5 GeV and 820 GeV respectively. The dotted lines are lines of constant y=1.0,0.1,0.04. The energy-isolines of the current jet are drawn for E_{jet} = 5, 10, 15, 50, 100, 200 and 400 GeV, the dashdotted line shows the isoline for $E_{jet} = E_e = 27.5\,GeV$, where x is independent of Q^2. The γ_H-isolines are drawn for γ_H = 20, 70, 120 and 170°. The dashed lines show the coverage of the different calorimeter components.*

In figure 4.3 a) and b) one sees several lines of constant E_{jet} and γ_H, respectively, in the (x, Q^2) plane (lines of constant y are also included).

4.2.3 *The Double Angle Method*

The double angle method is based on the knowledge of both scattering angles θ_e and γ_H. From simple four-momentum conservation (neglecting the rest masses of the electron and the quarks) the scattered electron energy can be obtained in terms of

these 2 angles :

$$E_{e'} = \frac{2E_e \sin\gamma_H}{\sin\gamma_H + \sin\theta_e - \sin(\gamma_H + \theta_e)}$$

Eliminating $E_{e'}$ in formulae (4.10)-(4.12) this leads to the following formulae :

$$Q^2_{DA} = \frac{4E_e^2 \sin\gamma_H(1+\cos\theta_e)}{\sin\gamma_H + \sin\theta_e - \sin(\theta_e + \gamma_H)} \tag{4.23}$$

$$x_{DA} = \frac{E_e \sin\gamma_H + \sin\theta_e + \sin(\theta_e + \gamma_H)}{E_p \sin\gamma_H + \sin\theta_e - \sin(\theta_e + \gamma_H)} \tag{4.24}$$

$$y_{DA} = \frac{\sin\theta_e(1-\cos\gamma_H)}{\sin\gamma_H + \sin\theta_e - \sin(\theta_e + \gamma_H)} \tag{4.25}$$

Since the calculation of γ_H (see formula 4.19) relies only on ratios of energies it is, in first order, independent of the energy calibration and scale uncertainty of the detector. For the double angle method the precision of the reconstruction of the kinematic variables depends only on the achieved angular resolution.

5

The Monte Carlo Simulation

Monte Carlo (MC) simulations in high energy physics experiments have become an (almost) indispensable tool. Generally they consist of two major parts, the first of which simulates the selected physical processes, generating four-momentum vectors that describe the complete final states. Section 5.1 will give a short introduction to the Monte Carlo generators used for this analysis. The second part uses these four-vectors and simulates the response of the detector used for the measurements. This will be covered briefly in section 5.3. In contrast to the first part, the second is strongly dependent on the experiment. Naturally, the aim of the Monte Carlo is to generate events that describe the physics measured in the detector.

The power of Monte Carlos can be visualized by listing a few of their uses in an experiment:

- In the planning and designing phase, MCs are used to optimize the design of the experimental apparatus for the intended studies. The same applies for later detector upgrades, where they are extensively used to test the modifications. This avoids the high costs of building and modifying several test detectors (although modifications of the "final" design might still be necessary).

- In the running phase of the experiment, MCs are used to develop and test strategies to extract the desired signal from background noise or at least optimize the signal-to-background ratio. Naturally for very specific searches very accurate MC models have to be used.

- In the recent decade the collider technology has improved strongly, leading to

very high luminosity experiments with high interaction frequencies. Readout electronics, data transfer and storage space set limits to the experiment. To select interesting or rare events out of the huge amount of background or well understood events, highly sophisticated signal triggers have to be developed and tested. Again, before the triggers are included into the readout logic, they have to be tested extensively on MC simulations in order to avoid unnecessary losses of luminosity.

- MCs allow a direct comparison of uncorrected data with theoretical models simulated in the MC. This is often referred to as comparison on the "detector level".
- MCs are needed to estimate efficiencies and acceptances of the detector for the measured process. Knowing these allows one to correct the measured distributions for detector effects and to extract the underlying physics that can then be compared to other experiments or the theoretical model underlying the MC (comparison on the "particle level").
- Often the MCs are used for a further correction, unfolding the fragmentation processes from the hard interaction. Here one attempts to measure directly the interacting partons, hence this is referred to as comparison on the "parton level".

As a last and general remark I would like to mention that despite the usefulness and necessity of MCs one should not forget that the main aim of an experiment should not be the comparison with the MC but rather the comparison of data with other experiments and test of the theory in new regimes.

5.1 Phenomenological Description of Parton Cascades

As already mentioned in section 2.1, the presently accepted model in high energy particle physics is the standard model and the underlying field theory, QCD, should in principle formally describe all observed processes involving quarks and gluons. The

basic scattering processes are well understood and calculable in the framework of the quark parton model QPM. In addition, higher order QCD corrections are calculated (either exactly or as numerical approximations). However, it is not known how to calculate completely a process that creates a multiplicity of partons in a so called parton shower. Furthermore there is no exact theory to describe the transition between these partons and the final state hadrons which are observed in the experiment. For these so called hadronization processes the energies involved are very small. Therefore the coupling constant α_S is too large to allow perturbative approaches. To describe the different stages in the event evolution phenomenological models have been invented and implemented in Monte Carlo generators. Combined, these MC generators simulate the complete scattering process.

There is an increasing variety of MC generators available to model the physics of different categories of collider experiments. The aim of this thesis is the study of ep NC DIS scattering processes. Therefore the overview will be restricted to the modeling of this class of processes, although in most of the cases an extension to other processes is existing or possible.

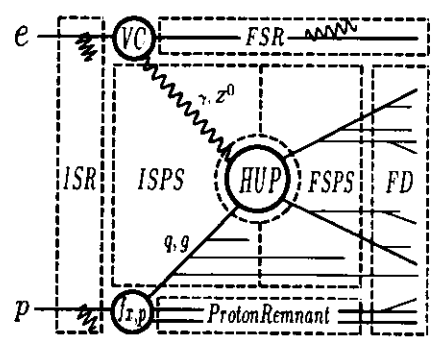

Figure 5.1: *Schematic illustration of the different stages in the event evolution simulation of a NC DIS ep scattering process. Legend (in alphabetical order):*
FD: fragmentation and decay; $f_{x,p}$ proton parton distribution function, HUP: Hard underlying process, ISPS/FSPS: initial/final state parton shower, ISR/FSR: initial/final state radiation, VC: vertex correction.

Figure 5.1 shows a schematic illustration of the different stages in the phenomenological description of the event evolution of an ep NC DIS scattering process. In the initial state radiation phase, ISR, the incoming proton and electron can radiate photons. Thereafter the (virtual) photon or Z, emitted from the e interacts with a parton, either a quark or gluon, of the proton. This parton can initialize an initial state parton shower ISPS. The scattered partons evolve into a final state parton shower FSPS. Finally the partons (of the parton shower and proton remnant) fragment into observable particles. The last step, FD, includes decays of instable particles.

The borderline between the different stages is not as clean as emphasized in this figure, *i.e.* nobody knows where to draw the transition line between final state parton showers and the fragmentation process. Furthermore, the processes are not completely independent, *i.e.* the calculation of the cross section of the scattering process as a function of the kinematic variables (which is usually done in the MC modeling stage denoted as "hard underlying process") requires the knowledge of the radiative corrections (initial state radiation ISR and final state radiation FSR) as well as the parton momentum distribution of the proton. In the process of event simulation the different stages are interlinked.

The following sections will describe the principles of the MC generators used in this analysis for modeling the individual stages.

5.1.1 Hard Underlying Process

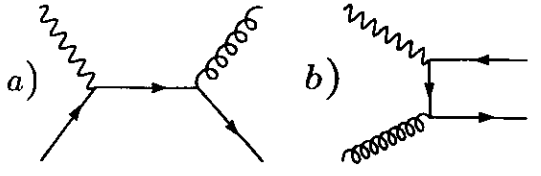

Figure 5.2: *Basic hard underlying processes in ep NC DIS scattering: a) QED Compton scattering; b) boson gluon fusion BGF*

The basic step in the MC simulation of ep DIS scattering is the calculation of the so called hard underlying process HUP (central circle in figure 5.1). Figure 5.2 shows the two basic elastic scattering processes $\gamma^*(Z^0)q \to qg$ (QED Compton) and $\gamma^*(Z^0)g \to q\bar{q}$ (boson gluon fusion BGF). Folding in the parton distribution function $f_{x,p}$ and taking into account QED and QCD radiation effects as described in sections 5.1.2 and 5.1.4, respectively, allows one to calculate the cross sections for the processes $ep \to e'X$. Adding final state radiation FSR (section 5.1.4) allows one to include processes of the type $ep \to e'X \to e''\gamma X$.

For $e^{\pm}p$ at HERA energies the event generator HERACLES (see [Kwi91]) generates DIS events at the parton level, PYTHIA (see [Sjö94]) is adapted and modified to generate diffractive photon-pomeron interactions. Both generators calculate the corresponding cross sections as functions of x, y, Q^2 and W. The implementations allow an easy switch between different sets of parton density functions or structure functions of the proton (or pomeron). The input to the event generators proceeds via control cards which provide information about the incoming beam energies, the selected processes and the kinematic regime of the simulation. The output contains the 4-momentum vectors of the final state partons as well as the calculated cross section and luminosity of the generated event samples.

The production of strange quarks in the final state of NC DIS $e^{\pm}p$ scattering is included as *a*) the scattering of a photon off a s ($\bar{s}$) quark from the proton quark sea or *b*) in $s\bar{s}$ pair production in boson gluon fusion processes (figures 5.3 *a*) and *b*) respectively).

5.1.2 Parton Showers

As mentioned above, the parton multiplicity cannot be reproduced from the hard underlying process alone, a further parton production mechanism is needed. The two following subsections give a brief introduction to two existing models.

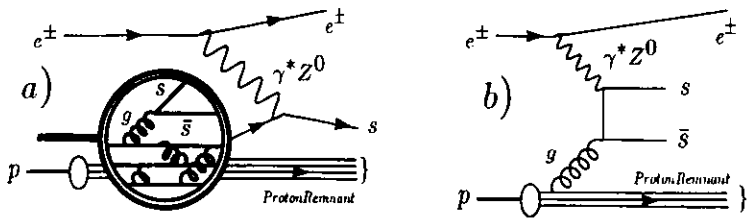

Figure 5.3: *Production of final state strange quarks in a) scattering off a strange sea quark and b) boson gluon fusion.*

The Colour Dipole Model

In the Colour Dipole Model the parton production is based on gluon emission from colour dipole antennae. The cross section for such a gluon emission is given by the dipole-like formula

$$d\sigma \approx \alpha_s \frac{dp_t^2}{p_t^2} dY\, d\phi \tag{5.1}$$

where p_t,Y and ϕ denote the transverse momentum, rapidity and azimuth angle of the emitted gluon with respect to the dipole axis. Depending on the underlying hard or other preceding processes there are four different production mechanisms to be considered : gluon emission from $q\bar{q}$, qg, $\bar{q}g$ and gg dipoles. The resulting 3 parton system is then treated as a system of two independent colour dipoles that can radiate gluons again. As a competing mechanism for further gluon emission the splitting $g \to q\bar{q}$ is taken into account. The energy splittings in the emission processes can be calculated from the relevant Feynman diagrams and are in agreement with the equivalent Altarelli-Parisi splitting functions (see section 2.3). The case of boson gluon fusion (BGF) as the underlying hard process can not be described easily with the dipole emission. Therefore, this process is either generated separately as hard underlying process or a matching procedure is introduced that regulates the emission of the antipartner of the struck quark, off the initial dipole between hadron remnant and struck quark, according the BGF matrix element. In each case both of the created q and $\bar{q}$ form a colour dipole together with the proton remnant. Photon emission from a $q\bar{q}$ EM dipole can be included optionally.

Figure 5.4 shows a schematic illustration of two subsequent gluon emissions.

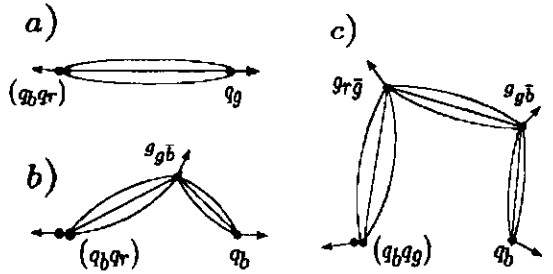

Figure 5.4: *Schematic illustration of gluon radiation off a colour dipole between the struck quark and the remnant diquark of the proton. a) the diquark of the proton remnant and the struck quark fly apart in their centre of mass frame, forming a (qq)-q colour dipole. b) a gluon is emitted and the dipole splits into two dipoles. c) a second gluon is emitted from the (qq)-g dipole.*

Strictly this model is only valid for two pointlike colour sources forming the antenna. In DIS however, the proton remnant is an extended object leading to a suppression of high energy gluon emission. This is modeled in reducing the available phase space.

Intrinsic to this approach is the angular ordering which decreases the opening angles for subsequent splittings. This reproduces "coherence", a quantum mechanical effect suppressing wide angle emissions. Furthermore a strong ordering in the p_t^2 scale (decrease in p_t^2 for subsequent emissions) which reduces the successive phase space region is included. A restriction of this model is that it does not include initial state radiation off the interacting parton (which therefore has to be simulated already at the stage of the hard process), *e.g.* a gluon emission from a quark, and their interference with the final state radiation.

The implementation of this model in a MC program is called ARIADNE (see [Lön92] and its unpublished Revision 6). The production of strange quarks is steered via input parameters defining the number of allowed quark flavours participating in the shower development and the mass dependence of the splitting functions.

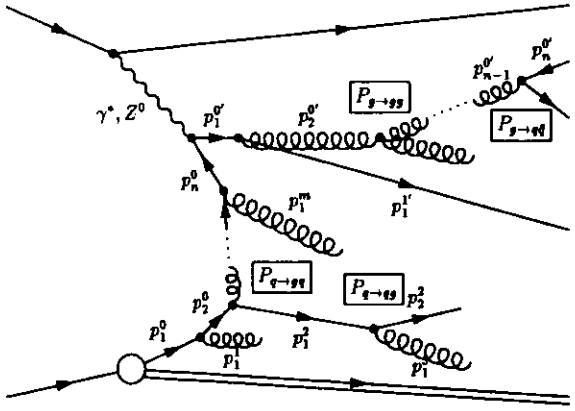

Figure 5.5: *Schematic parton shower process including initial and final state QCD radiation. p_m^n ($p_m^{n'}$) denotes the four-momentum of the n-th shower particle before the m-th splitting process in the initial (final) state radiation shower. $P_{q\to qg}$, $P_{g\to gg}$, $P_{g\to q\bar{q}}$ and $P_{g\to gg}$ represent the Altarelli-Parisi splitting functions of the corresponding vertex*

The Parton Shower Model

The parton shower model is strongly based on the fact that initial and final state partons of the interaction process have to be on mass-shell ($\sim \mathcal{O}(1\,GeV)$). Since DIS proceeds via the exchange of a highly spacelike virtual boson this implies that the interacting parton at the boson vertex has to absorb this virtuality. A mechanism to produce a parton shower and fulfill this requirement at the same time is pictured in figure 5.5 and can be separated into three stages :

1. In the first stage an initial parton (with four-momentum p_1^0) initiates a cascade (initial state radiation) where at each branching point one daughter parton acquires an increasing spacelike virtuality while the second parton is on-shell or timelike. This spacelike shower is characterized by increasing spacelike virtuality $-(p_n^0)^2 > -(p_{n-1}^0)^2 > ... > -(p_1^0)^2$, decreasing parton energies and, on average,

increasing opening angles at the branching points.

2. At the boson vertex the spacelike shower evolution ends, the parton absorbs the spacelike virtuality of the boson and turns thereby into an on-shell or timelike parton ($\Rightarrow (p_1^{0'})^2 = (p_n^0 + q)^2 \geq 0$).

3. In case of a timelike outgoing parton at the boson vertex a timelike shower is initiated (final state radiation), characterized by decreasing timelike virtuality ($(p_1^{0'})^2 > (p_2^{0'})^2 > ... > (p_n^{0'})^2 = \mathcal{O}(1\,GeV)$), decreasing parton energies and decreasing opening angles at the branching points. The last feature is introduced by strict angular ordering of the consecutive branchings simulating coherence effects. The shower evolution will stop when all the daughter partons are close to their mass-shell. Generally at each branching point with a timelike parton such a cascade will be initiated.

Both initial state and final state radiation are based on the same branching processes and are therefore very similar. The parton splitting probabilities into gluons or different quark flavours and their four-momentum splitting at each branching point are the same for both processes and described by the Altarelli-Parisi splitting functions. The overall scale dependence on x and Q^2 is expressed through the Altarelli-Parisi evolution equations, which are in leading logarithm approximations in perturbative QCD. From these, a probability factor can be calculated expressing the probability that a parton does not branch within some virtuality range or m^2 range for initial and final state radiation respectively.

A technical problem arises for the initial state radiation since usually one wants to generate events in a known kinematic range. The kinematic variables on the other hand can only be reconstructed knowing the evolution of the initial spacelike shower, mainly the spacelike virtuality of the final interacting parton (p_n^0 in 5.5) has to match the timelike virtuality of the exchange boson to be in agreement with the hard interaction cross section. Naturally this is very difficult starting with some initial parton and evolving the spacelike shower with increasing spacelike virtuality.

Instead an approach starting at parton p_n with an appropriate virtuality evolving the shower backward with decreasing spacelike virtuality avoids this problem. The Altarelli-Parisi evolution equations describe the probabilities of a branching process as a function of increasing virtuality but they can as well be interpreted in the "backward direction", describing the probabilities for merging processes as a function of decreasing virtualities. Calculating these merging probabilities allows one to trace the spacelike shower back to the initial virtuality of p_1^0.

A more complete description of the method and its implementation in the LEPTO 6.1 MC program can be found in [Ben87] and [Ing91] respectively.

5.1.3 Hadronization and Decay

To describe the transition from partons to final state hadrons only phenomenological models exist. The hadronization starts when the partons of the parton shower are close to their mass shell. This implies that the process is independent of the underlying hard interaction. This universality allows one the use of the Lund model approaches to hadronization that have been developed and tested on e^+e^- data.

The approach used in the Monte Carlo samples is based on the so called string fragmentation model (SF). All partons are connected by a colour string. This string can be visualized as a colour flux tube of uniform energy density. As neighboring partons move apart, the flux tube is stretched and this increases its potential energy. If the energy density becomes high enough, the string breaks, creating a new $q\bar{q}$ colour singlet pair that connect with a colour string to their neighbors. The break usually happens after a separation of $2-5\ fm$, *i.e.* at typical hadron diameters. This reproduces the notion of confinement.

The production probability for the different quark flavours of the $q\bar{q}$ pairs is derived from classical considerations that predict that massive quarks must be produced at a certain distance. Quantum mechanically they may be created in one point and tunnel out into the classically allowed region. The tunneling probability is then given as:

$$P_{tunneling} = e^{-\frac{\pi m^2}{\kappa}} e^{-\frac{\pi p_t^2}{\kappa}} \tag{5.2}$$

where $\kappa \sim 1\ GeV/fm \sim 0.3\,GeV^2$ is a string constant giving the amount of energy per unit length inside the string, m the mass and p_t the transverse momentum of the produced quark (and antiquark). Assuming constituent masses of $m_u = m_d = 0.3\,GeV$, $m_s = 0.5\,GeV$, $m_c = 1.6\,GeV$ this predicts a relative production rate of $P_u : P_d : P_s : P_c \sim 1 : 1 : 0.3 : 10^{-11}$. Charm and heavier flavour production is hence strongly suppressed and not part of the fragmentation process. The ratio P_s/P_u is henceforth referred to as strange quark suppression factor since strange quarks will be less likely to be formed in parton fragmentation. The string is assumed to have no transverse excitation so the p_t of the quark-antiquark pair is locally compensated. This leads to a flavour independent Gaussian p_t distribution. The determination of $P_s/P_u = 0.3$ is based on studies of strange quark production in e^+e^- experiments and is in agreement with the classical estimate above. Assuming that the fragmentation process of a scattered quark is independent of the underlying scattering process (jet universality), this parameter should be the same in any DIS experiment.

If the invariant mass of the new system is high enough, further breaks can occur. Hadrons are then formed by the quark from one break and an antiquark from the adjacent break forming a colour singlet, starting at one end of the string system. The production of (anti-) baryons is not as simple. One mechanism is to produce diquark-antidiquark pairs (colour triplet-antitriplet) in the string, following the same tunneling idea as for $q\bar{q}$ pairs. However, diquark masses carry large uncertainties that prevent predictions about the relative production probabilities. A second approach is the consecutive production of two $q\bar{q}$ pairs of different colour, where the two quarks (or antiquarks) drift towards each other forming a diquark. The effective colour of the diquark follows from the colour of the individual quarks (*i.e.* $q_r + q_b \rightarrow (qq)_{\bar{g}}$). From e^+e^- data a relative probability for diquark to quark production of $P_{qq} : P_q \sim 1 : 10$ has been determined. The production of strange baryons is then regulated by the probability of creating a strange diquark. The ratio $(P_{qs}/P_{qu})/(P_s/P_u)$ is referred to as extra suppression of strange diquark production compared to the normal suppression of strange quarks. As P_s/P_u, $(P_{qs}/P_{qu})/(P_s/P_u) = 0.4$ has been determined in studies

of strange quark production in e^+e^- experiments.

The hadrons that are produced in the fragmentation process may be be unstable and decay. For strong and electromagnetic decays the branching ratios are known and the momentum distributions are generated by phase space considerations. The weak hadronic and leptonic decays are implemented according to the weak mixing between the quark generations and lepton families.

A more complete description of string fragmentation can be found in [And83] and its implementation in the JETSET program can be found in [Sjö86].

5.1.4 Radiative Corrections

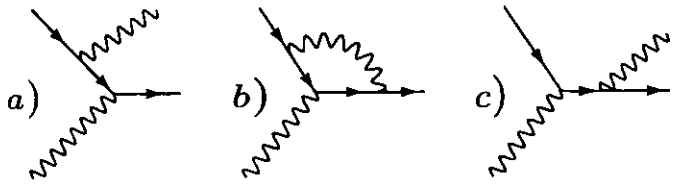

Figure 5.6: *Lowest order Feynman graphs for QED radiative corrections : a) initial state radiation ISR ; b) vertex correction VC c) final state radiation FSR.*

Figures 5.6 a)-c) show the lowest order Feynman graphs leading to radiative corrections as indicated in figure 5.1 (ISR,VC and FSR). The event generator HERACLES (see [Kwi91]) allows photon radiation from a) initial and c) final state positron and/or quark. The vertex corrections of type b) are included optionally, allowing also weak virtual interactions (exchange of a Z^0 instead of a γ). Furthermore, interference effects of leptonic and quarkonic radiation are modeled.

Initial state photon radiation will decrease the energy of the interacting positron (parton) and thereby reduce the centre of mass energy for the scattering process. Final state radiation will fake a higher four momentum transfer. The vertex corrections modify the interaction vertex. In any case it will lead to a wrong reconstruction of the true kinematic variables. Therefore these corrections have to be included in the MC in order to allow a study and/or correction of their influence.

5.2 Simulation of Deep Inelastic Scattering

To describe the neutral current DIS data sample under investigation in this thesis four different sets of Monte Carlo event samples have been used. First there are two event samples generated with models describing the "standard" non-diffractive DIS. Due to the fact that these models fail to reproduce the contribution of peripheral scattering processes (observed at ZEUS as events with very low energy deposition in the forward region and comprising $6-10\%$ of the total sample), one of these two models includes a pomeron-like part in the structure function. Both of these models will be described in subsection 5.2.1. Two further event samples are used, according to models as described in subsection 5.2.2 to model the purely diffractive scattering processes.

5.2.1 Nondiffractive Models for DIS

The two non-diffractive DIS MC models differ only in the modeling of the parton showers as described in section 5.1.2 and have been named after these models :

Matrix Element with Parton Shower (ME+PS)

Several sets of MC samples of type ME+PS have been used for this analysis. All of them used HERACLES 4.4 to generate the hard process on the parton level. The output is interfaced to DJANGO 6.1 calling routines from LEPTO 6.1 to simulate the QCD cascades. JETSET 7.3 is used to simulate the fragmentation process.

The MRSD'- ([Mar93]) parameterization was used to describe the parton distribution inside the proton.

For most of the analysis only the MC sample with $Q^2 > 4\,GeV^2$ is used. The "high Q^2" samples are included for the study of the Q^2-dependence of the strange particle production rates.

Colour Dipole Model + Boson Gluon Fusion (CDM+BGF)

Several sets of MC samples of type CDM+BGF have been used for this analysis. All of them used HERACLES 4.4 to generate the hard process at the parton level. The

Generator Chain	HERACLES → DJANGO → LEPTO,JETSET		
Proton SF	MRSD'-		
Number of events	300 000	79 000	80 000
$Q^2_{min}[GeV^2]$	4	40	100
Cross Section $[nb]$	387	23.7	6.5
Luminosity $[nb^{-1}]$	775	3330	12300

Table 5.1: *Specifications for ME+PS MC samples*

output is interfaced to DJANGO 6.1 calling routines from ARIADNE 4.06 (simulating the parton cascades) and JETSET 7.3 (simulating the fragmentation process). Diffractive interactions are included as hard scattering processes between a pomeron-like particle which is part of the proton structure function (modified MRSD'- parameterization).

Generator Chain	HERACLES → DJANGO → ARIADNE,JETSET	
Proton SF	MRSD'- + Pomeron	
Number of events	377 000	271 000
$Q^2_{min}[GeV^2]$	3.3	4
Cross Section $[nb]$	444	391
Luminosity $[nb^{-1}]$	758	693

Table 5.2: *Specifications for CDM+BGF MC samples*

5.2.2 *Diffractive Models for DIS*

POMPYT

The current implementation of the Ingelman-Schlein-model (see section 2.5.1) in a MC generator is called POMPYT. The hard scattering processes between the partons of the pomeron and the photon are simulated within the frame of the PYTHIA 5.7

([Sjö94]) MC generator. The pomeron dynamics and structure are included with additional routines as described in [Bru94]. The hadronization is modeled with JETSET 7.4.

A hard version for the parton density parameterization of the pomeron is chosen. For this study it is important to mention that no strange quark content of the pomeron is assumed so far and thus the production of strange particles is restricted to the fragmentation processes.

The events within this MC sample have been generated using a weighting procedure in order to produce events more efficiently, *i.e.* events are produced equally over a wide kinematic range. In order to get correct results, each event has to be weighted by its probability as calculated from the kinematics. However, this means that the cross-section and the luminosity are strongly dependent on the equivalent number of selected events.

Generator Chain	PYTHIA → JETSET
Pomeron SF	$f_q(\beta) = \frac{6}{4}\beta(1-\beta)$
Number of events	120 000 (weighted)
$Q^2_{min}[GeV^2]$	4

Table 5.3: *Specifications for the POMPYT MC sample*

NZ

The implementation of the NZ (referring to the initials of the authors N. N. Nikolaev and B. G. Zakharov) model in a MC generator is called EPDIFFR (author A. Solana, no manual existing so far). The current version incorporates both "hard" and "soft" components of diffractive scattering. The relative admixture for photon fluctuation into $u\bar{u} + d\bar{d}$, $s\bar{s}$ and $c\bar{c}$, is given approximately as 89:10:1 for $u\bar{u} + d\bar{d} : s\bar{s} : c\bar{c}$. For the parton shower and fragmentation processes the LUND model as implemented in JETSET 7.3 is used.

As for the POMPYT MC, the events are generated using a weighting procedure.

Generator Chain	EPDIFFR → JETSET
Effective Pomeron SF	$f_{\mathbb{P}}(\beta) = A\beta(1-\beta)^2 + B(1-\beta)^3$
Number of events	50 000 (weighted)
$Q^2_{min}[GeV^2]$	4

Table 5.4: *Specifications for the NZ MC sample*

5.3 *Detector Simulation*

The simulation of the detector response for ZEUS proceeds in the MOZART software package. It is based on the GEANT ([GEA]) package that has been developed continually over the last 2 decades at CERN. The detector is described in form of geometrical volumes, to each of which a filling medium or material is assigned. The program contains lookup tables for the properties of the different media (such as radiation lengths, etc.) as well as of the particles (such as life times, etc.) that pass through the detector. It allows one to transport particles through the detector and its geometrical boundaries, taking into account physical effects according to the nature of the particles, their interaction with matter and magnetic fields. It also contains code to describe the evolution of electromagnetic and hadronic showers in materials. As input it accepts events that have been simulated by Monte Carlo generators. A graphical representation of the detector and the particle trajectories is supported.

MOZART is the adaption for the ZEUS detector. It contains a very detailed description of the ZEUS detector in form of a data base. Obviously great care has to be taken in simulating all the different materials and structures that build up a complex detector as ZEUS in order to simulate the response a real particle would produce passing through this detector. The output of MOZART are data banks that have exactly the same structure as the data banks that get created from the "real" ZEUS detector read out when events are measured. They contain information like energy deposits in calorimeter cells or scintillators, or hits in the CTD, etc. thus reflecting the detector response. In addition, further data banks are filled that keep

all the information of the generator level.

The simulation of the trigger logic which is used for the data taking (see 6.2) is done in the program ZGANA. It permits easy testing of new trigger criteria and the calculation of the trigger acceptance with MC events that have been passed through the detector simulation MOZART. It determines for each event which subtriggers are satisfied and stores the result as "trigger bits".

6

THE DIS DATA SAMPLE

6.1 *1994 Data Taking*

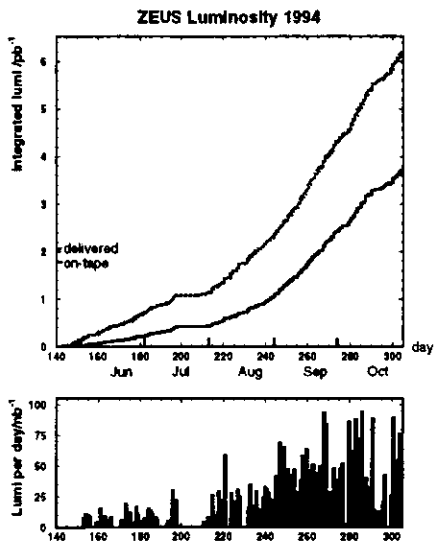

Figure 6.1: Luminosity history for the 1994 run period. The upper picture shows the integrated luminosity as delivered from HERA and as accumulated and written to tape by the ZEUS experiment. The lower picture shows the accumulated integrated luminosity on a daily basis.

Figure 6.1 shows the data taking history for the 1994 run period. The upper picture shows the integrated luminosity as delivered from HERA and as accumulated and written to tape by the ZEUS experiment. In the e^-p run period between mid May

and mid July HERA delivered around $1.2\,pb^{-1}$ out of which the ZEUS data acquisition system wrote $\sim 0.5\,pb^{-1}$ to tape. In the positron run period, from the beginning of August until end of October, HERA delivered another $\sim 5\,pb^{-1}$ out of which ZEUS archived $\sim 3.2\,pb^{-1}$. The difference between HERA delivered and ZEUS acquired luminosity indicates an overall efficiency of $\sim 60\,\%$ for the data taking procedure. This efficiency includes periods where the detector readout is inactive due to experimental procedures that have to be followed after new beam fills, *e.g.* the closing of the detector and the ramping of the high voltage system of the CTD. The efficiency of the ZEUS detector and the data acquisition system at stable beam conditions is usually better than 80 %. The lower picture shows the accumulated integrated luminosity on a daily basis.

6.2 *Online Event Selection*

The online event selection is meant to provide a basic data sample for a wide variety of studies of physics processes while reducing the huge background arising from interactions other than *ep* scattering (*i.e.* beam gas events) and *ep* events of no interest. Furthermore, the readout electronics, the digitization procedure and the data transfer to storage areas are limited in their capability of handling the high rate of interactions in the detector.

For the ZEUS detector a trigger system has been designed that decides in three subsequent levels, called GFLT, GSLT and TLT (abbreviations for Global First/Second Level Trigger and Third Level Trigger, respectively) whether to keep or to reject an event. On the lowest level, the GFLT, the time constraint is tightest and a fast decision is necessary in order to avoid dead times in the data acquisition. Therefore very simple algorithms are used here, while algorithms with increasing sophistication are used on the subsequent GSLT and TLT levels. Furthermore, on the GFLT and GSLT level each participating component has its own local trigger system (referred to as local FLT or SLT) and intermediate buffer (so called pipelines for the FLT). The local trigger systems process in parallel their trigger calculations and send the

trigger decisions to the global trigger box where they are combined into global trigger decisions. Until a decision is made on these levels, the data are stored in the buffer. In case of a positive trigger decision the data are passed on and subjected to the decision on the next level. In case of a negative trigger decision the buffers are cleared and the procedure starts for the next event. The data from all detector components of events that pass the GSLT trigger conditions are combined into the final data structure in the Event Builder (EVB) and transferred into the event buffers of the TLT.

6.2.1 GFLT

The trigger decisions of the local FLT are based on simple activity threshold conditions in subranges (so called trigger regions) of the corresponding detector part. The GFLT has 64 "trigger slots" corresponding to 64 different logical combinations of local trigger decisions. Any of the trigger slots can be individually prescaled (or switched off) by a factor of n, meaning that only every nth event passing this subtrigger condition will lead to a positive trigger decision. The GFLT trigger decision is a logic OR of the individual trigger slots.

The aim of the GFLT is a rate reduction to an output rate of $500\,Hz - 100\,Hz$. In 1994 a usual input rate (as measured with the C5 counter) was of the order of $20kHz$. The actual definition of the individual triggers (thresholds and/or logical combinations and/or prescale factors) has to cope with the luminosity conditions and is therefore subject to changes over the run period. The "trigger history" is documented and accessible in form of data bases.

6.2.2 GSLT

The GSLT consists of 8 subtriggers that are run in parallel, only 5 of which were active in the 1994 run period :

st0 Environmental and test triggers.

st1 Passthrough and calibration triggers.

st2 Runs veto algorithms.

st3 Runs physics filters.

st7 Fills reference histograms.

An event is accepted if it fulfills a logic OR of the subtriggers **st0** to **st3**. The histograms provided from **st7** do not contribute to a trigger decision but are used by the shift crew in order to detect problems in the detector performance. Events accepted by **st0** provide information such as the detector status and beam conditions, events accepted by **st1** are used for trigger and background studies and to test the electronic readout of the calorimeter. The rates from these subtriggers are low during physics runs. The subtriggers **st2** and **st3** use the information provided from the local SLT triggers.

There are 8 veto algorithms implemented in **st2** in order to reject beam gas events, cosmic muon events and so called spark events. All these algorithms use solely information provided from the calorimeter (CAL) SLT. The most powerful tool is the CAL event timing. CAL provides a time resolution better than $1\,ns$ (see [Fre94]) for cells with an energy above $1\,GeV$. For ep collisions at the nominal interaction point the CAL timing is calibrated to be zero in the whole calorimeter. Events related to interactions between the proton beam and residual gas in the beampipe arrive early in the RCAL, events originating from electron interactions with beampipe gas arrive early in the FCAL. Furthermore, the timing difference between FCAL and RCAL is large for beam gas related events and around zero for ep interactions. Beam gas events are rejected if $\mid T_{RCAL} \mid > 8\,ns$, or $\mid T_{FCAL} \mid > 8\,ns$ or $T_{FCAL} - T_{RCAL} > 8\,ns$. Cosmic muons passing through the calorimeter will show a large time difference between the upper and lower half of BCAL and are therefore rejected with the requirement $T_{up} - T_{down} < -10\,ns$ (and no energy in FCAL and RCAL). The calorimeter times are determined as energy weighted averages (the time resolution improves with energy) of the individual cell times. Spark events are triggered by a discharge in the base of single photomultiplier tubes, leading to a high imbalance between the two photomultipliers in one cell. Two "spark algorithms" are used to veto such events. Kinematics in ep interactions restrict the maximum observable $E - p_z$ to twice the

electron beam energy, where $E - p_z = \sum_i E_i(1 - cos(\theta_i))$. The sum runs over all calorimeter cells, E_i is the energy deposited in a calorimeter cell, θ_i the corresponding angle of this cell with respect to the reconstructed interaction point. Therefore a veto $E - p_z > 75\,GeV$, based on CAL energy sums, is used to reject beam gas events. Finally an "empty trigger veto" rejects events that were triggered by CAL FLT and have only very little energy in CAL.

st3 consists of a total of 28 physics filters that use GFLT trigger information as well as (already performed) energy calculations of the LUMI and CAL and tracking information of the CTD. NC DIS events are selected by :

DISSF : a logic OR on a subset of FLT filter bits (energy threshold in CAL sections and isolated energy depositions in combination with vetoes from C5, Veto Wall and SRTD). This insures a minimum activity in CAL associated with a DIS event.

DIS1 : a threshold $E - p_z + 2 \cdot E_{LUMIG} > 24\,GeV$ for events that pass DISSF or have a transverse energy in CAL $E_t > 25\,GeV$. This cut indicates a reconstructed scattered electron in the calorimeter with a possible initial state photon with energy E_{LUMIG} detected in the photon calorimeter of the LUMI system.

The overall rejection is typically around $80\,\% - 90\,\%$, leading to an aimed acceptance rate of $50\,Hz - 10\,Hz$. Similar to the GFLT, the GSLT is adjusted to changes in the run conditions over the run period. Changes in the triggers (as well as more detailed information about the trigger definitions) can be found in [Chl94].

6.2.3 TLT

On the TLT level the input rate is already strongly reduced (to $\sim 0.1\,\%$ of the initial rate) leaving more processing time per incoming event. Furthermore, the complete information of all detector components is available, in addition to the trigger information of the GFLT and GSLT. This allows the implementation of more sophisticated and physics oriented trigger algorithms, using, for example, electron finders (routines

that look for the scattered electron) or tracking algorithms. This allows the physics groups to perform a preselection of the event class under study already at this stage and this speeds up the analysis. The TLT provides 96 trigger slots out of which ~ 80 have been used in the 1994 run period. The algorithms are implemented in Fortran code and often have their origin in former offline analysis codes. The output rate of the TLT is $10\,Hz - 1\,Hz$. Events that pass any of the active trigger slot conditions are transferred to mass storage on IBM tape cartridges.

The preselection of the NC DIS data sample uses 5 trigger slots :

DIS01 : (GSLT filter DISSF).AND.$(E - p_z + 2 \cdot E_{LUMIG} > 25\,GeV)$.AND.(electron found with the electron finders ELECT5 or LOCAL).AND.$(E_{e'} > 4\,GeV)$.

DIS02 : $(E - p_z > 25\,GeV)$.AND.$(E_t > 40\,GeV)$.AND.(not a cosmic muon event, identified with ISITAMU). The $E - p_z$ cut reduces the contribution from photoproduction events, where the scattered electron leaves CAL undetected.

DIS05 : DIS01, but without electron requirement.

DIS06 : DIS01, but without $E - p_z$ requirement.

DIS07 : (GSLT filter DISSF).AND.$(E - p_z > 20GeV)$

The analysis routines ELECT5, LOCAL and ISITAMU are part of the PHANTOM library, a ZEUS software library for analysis routines.

The TLT consists of a farm of 36 Silicon Graphics (SGI) workstations, divided into 6 branches. Each branch consists of a master machine and five processing nodes. The master machines accept events from the Event Builder and distribute them to the processing nodes that run, in parallel, identical reconstruction and analysis code (simplified versions of the ZEUS offline reconstruction code). The TLT was designed at the University of Toronto as part of the Canadian group contribution to the ZEUS experiment.

6.3 Event Reconstruction and Offline Selection

Before the data are available for further analysis, all events stored on the mass storage are "reconstructed" with ZEPHYR (abbreviation for ZEus PHYsics Reconstruction program). This program is logically divided into three phases.

Phase1 corrects the raw data using the detector calibration constants operative at the time the data were taken. The responses of the different components, such as energy deposits in calorimeter cells or tracks in the CTD, are reconstructed.

Phase2 The Phase1 data are used and combined in order to reconstruct more complex objects such as energy clusters or electrons in CAL.

DST The data are subject to a set of physics filters using Phase1 and Phase2 information as well as the online trigger bits set by GFLT,GSLT and TLT. The output of these physics filters is included in the data set of the reconstructed event and allows one an easy access to the events of interest later in the individual analysis.

This analysis is based on events classified by the "Clean NC DIS" bit B14 :

DIS01.OR.DIS02.OR.DIS05.OR.DIS06.OR.DIS07	.AND.
$E - p_z + 2E_{LUMIG} > 35GeV$	.AND.
Spark event rejection	.AND.
Beam halo muon event rejection	.AND.
Electron outside $32\,cm \times 32\,cm$ box around beampipe	.AND.
$E_{e'} > 5\,GeV$	.AND.
$y_{JB} > 0.02$	

The spark rejection uses the RMSPARK algorithm from the PHANTOM library. It recalculates the energy sums in the FLT trigger regions excluding cells with high energy imbalance. If the recalculated energy falls below a certain threshold the event is rejected.

Beam halo muons travel parallel to the beam line. The PHANTOM routine ALHALO2 checks for "peculiar" structures, such as many consecutive BCAL towers with

energy depositions but no tracks in the CTD.

The "box cut" around the beam pipe is essential for the reconstruction of the electron kinematics. A scattered electron with an impact point too close to the edge of the $20\,cm \times 20\,cm$ hole in RCAL, where the beam pipe enters the inner detector, (*i.e.* less then $6\,cm \sim 3$ Molière radii) will lose part of its shower energy into the beam hole, leading to a systematic shift in the energy and angular reconstruction.

The cut in the reconstructed electron energy insures a high efficiency and purity for the electron finding algorithms. A correctly reconstructed scattered electron is very effective in removing photoproduction events.

The cut in y_{JB} removes events with low y that would move to low x when using the double angle method and therefore improves the resolution in x.

The information from the environmental triggers (*i.e.* beam condition, detector configuration, etc.) and results from the component data quality monitoring are used to reject events or runs that were taken with bad running conditions. The list of events or runs with such bad conditions exist in the form of a data base in the PHANTOM routine EVTAKE.

6.4 The Final DIS Data Sample

The data sample passing the DIS preselection with B14 as discussed in the previous sections is still contaminated with background and photoproduction events. Furthermore, the reconstruction of the event kinematics depends on the method (see section 4.2) used and varies for the different regimes. Figure 6.2 shows for a DIS Monte Carlo sample (ME+PS) the migration of the kinematic variables in the $x - Q^2$ plane for four reconstruction methods. The $x - Q^2$ plane is divided into equal bins in $log_{10}(x)$ and $log_{10}(Q^2)$. The tail of each arrow is the average value of the generated x and generated Q^2 inside such a bin. The head of the arrow is the average value of the reconstructed x and reconstructed Q^2 originating from the same bin. Long arrows indicate a poor measurement of the kinematic variables due to acceptance or resolution limitations of the detector.

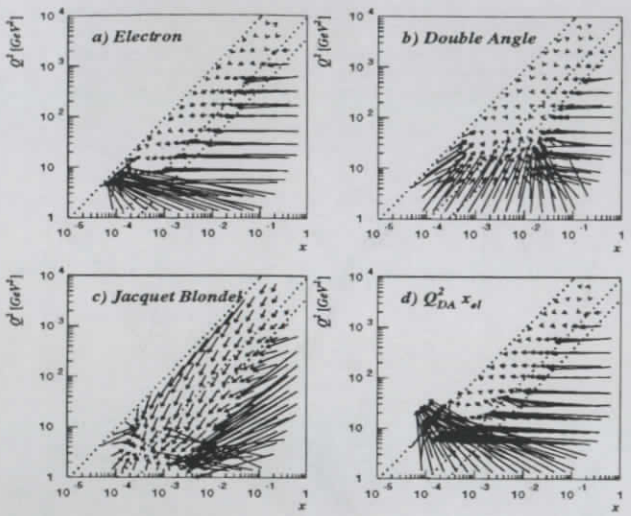

Figure 6.2: Migration in x and Q^2 for ME+PS DIS MC events with a reconstructed positron with energy $E_{e'} > 5\,GeV$. The dotted lines are lines of constant $y = 1, 0.1, 0.04$ (from left to right). The $x - Q^2$ plane is divided into equal bins in $log_{10}(x)$ and $log_{10}(Q^2)$. The tail of each arrow is the average value of the true x and true Q^2 inside such a bin. The head of the arrow is the average value of the reconstructed x and reconstructed Q^2 originating from the same bin. For the reconstruction of the kinematical variables the different methods as introduced in section 4.2 are used: a) The electron method; b) the double angle method; c) the Jacquet Blondel method; d) a hybrid of double angle method (Q^2) and electron method (x).

To improve the purity of the DIS sample further event selection criteria have been applied to the data sample :

1. The reconstructed event vertex is restricted to the range $-42\,cm < z_{VTX} < 48\,cm$ ($\sim \pm 45\,cm$ around the nominal vertex of the ep interaction). This rejects further beam gas and cosmic ray events.

2. A tightened cut $35\,GeV < E - p_z < 60\,GeV$ is applied. The lower boundary removes photoproduction and hard initial state bremsstrahlung events, the upper boundary cuts off beam gas events.

3. The electron is reconstructed with EEXOTIC, an algorithm based on ELECT5, but tuned to improve the angular resolution and purity. The reconstructed electron angle together with the reconstructed Q^2 (double angle method) are used to recalculate the electron energy $E_{e'}$ (inversion of equation 4.10). Events with $E_{e'} < 5\,GeV$ are rejected.

4. $y_{el} < 0.95$ removes events with an incorrectly identified electron. This cut affects only fake electrons in FCAL arising primarily from photoproduction events. The $E_{e'} > 5\,GeV$ selection criteria corresponds to $y_{el} < 0.82$ in RCAL and therefore does not influence electrons in RCAL.

In order to ensure that the MC samples reflect the DIS nature of the data, the distributions of some characteristic variables have been compared on the detector level. The agreement between the data and the MC is generally very good (see figures 6.3 *a*) – *k*)). The differences between data and MC in the Bjorken y (figure 6.3 *d*), reconstructed with the electron method (see section 4.2.1), is attributed to a known CAL energy scale problem. Not all of the inactive material, such as cables, support structures, etc., present in the real detector is included in the MC detector description. Therefore, particles in the detector will lose more energy in the ZEUS detector than in the MC detector simulation. From formula 4.12 it is easy to see that this effect leads to a shift of y_{el} to higher values, more pronounced for data than for MC. In figure 6.3 *e*) the shift is not visible, since the positron energy has been corrected with the Q^2_{DA}. Correcting y_{el} with the Q^2_{DA} converts the electron method into the double angle method. However, the rejection of fake positrons is best with the use of y_{el} and the agreement between data and MC is good for $y_{el} \gtrsim 0.6$. Again the shift to lower energies in the $E - p_z$ distribution of the data, compared to the MC, is based on the CAL energy scale problem. However, this shift of $\sim 5\,\%$ only affects events in the tail of the distribution and does not influence the results on the production rates of strange particles.

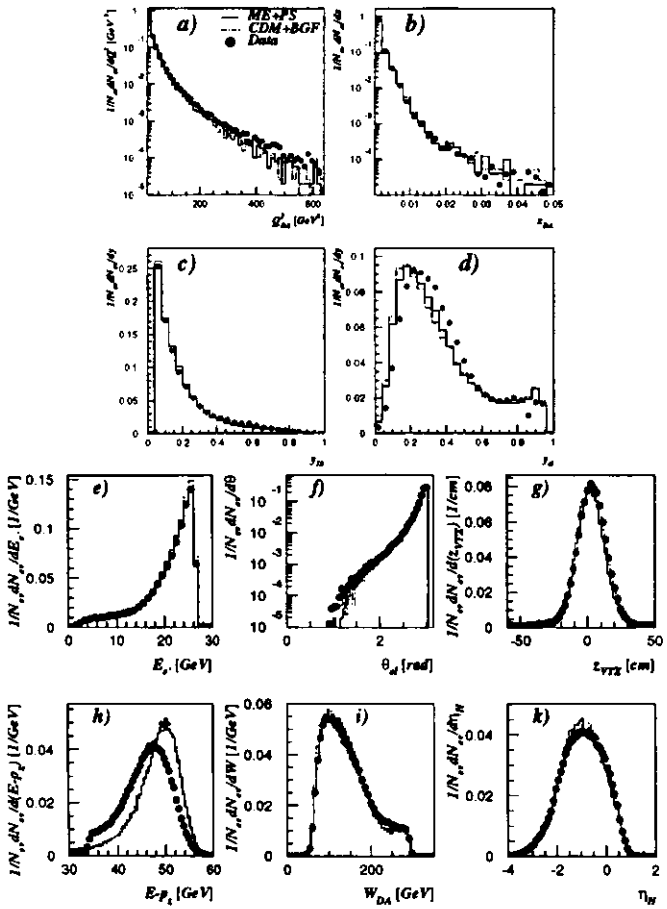

Figure 6.3: *Comparison of event rates of DIS characteristic variables for data (black circles) and ME+PS (line) and CDM+BGF (dash-dotted line) Monte Carlo : event rates as function of the reconstructed Bjorken variables (a) - (d), the scattered positron energy $E_{e'}$ (e), the scattering angle θ_{e1} of the positron (f), the z-coordinate of the event vertex z_{VTX} (g), $E - p_z$ (h), hadronic centre of mass energy W_{DA} (i) and the pseudorapidity of the struck quark η_H (k).*

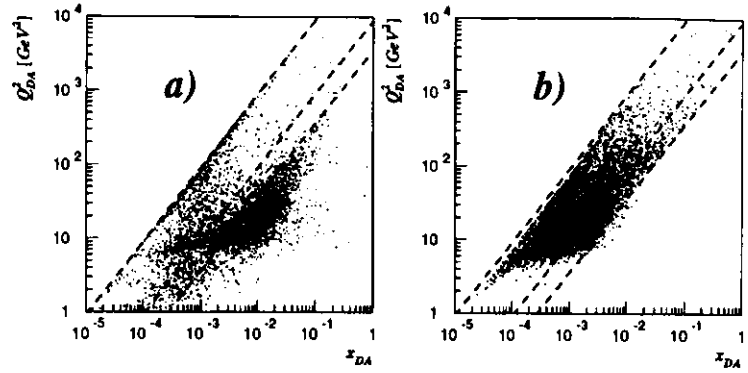

Figure 6.4: *Event distribution in the x–Q^2 plane of the DIS data sample. a) shows the distribution for events that fail the DIS event selection cuts, the events in b) are a subsample of events that passed the final event selection cuts. The dashed lines are lines of constant $y = 1, 0.1, 0.04$ (from left to right). The double angle method was used in order to reconstruct the kinematic variables.*

Figure 6.4 shows for a subsample of the DIS data the distribution in the x–Q^2 plane for events *a*) failing and *b*) passing the event selection criteria. The bulk of events failing the cuts are found at low y, reaching to higher values of y only for $Q^2 < 10\,GeV^2$. The central kinematic region with $Q^2 > 10\,GeV^2$ and $y > 0.04$ is relatively free from the effects of the cuts. However this central region is where events passing the event selection criteria accumulate. A total of 275352 events of the data sample remain after the DIS selection cuts.

6.5 *Event Migration in x, y, Q^2*

Figure 6.5 shows for the ME+PS DIS Monte Carlo sample the migration of the kinematic variables in the $x - Q^2$ plane for all events that pass the final DIS event selection criteria. The bin definitions and reconstruction methods are identical to that in figure 6.2. A comparison with 6.2 shows a suppression of events that would migrate from $Q^2 < 5\,GeV$ to values $Q^2 > 10\,GeV^2$. Furthermore event migration from high to lower x is reduced. Using the CDM+BGF sample instead of the ME+PS sample reproduces identical migration behaviour.

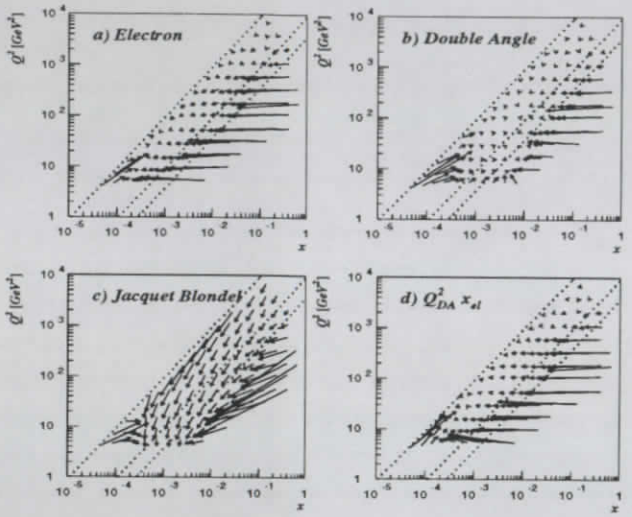

Figure 6.5: Migration in x and Q^2 for ME+PS DIS MC events that pass the final event selection cuts. The dotted lines are lines of constant $y = 1, 0.1, 0.04$ (from left to right). The $x - Q^2$ plane is divided into equal bins in $log_{10}(x)$ and $log_{10}(Q^2)$. The tail of each arrow is the average value of the true x and true Q^2 inside such a bin. The head of the arrow is the average value of the reconstructed x and reconstructed Q^2 originating from the same bin. For the reconstruction of the kinematical variables the different methods as introduced in section 4.2 are used: a) The electron method; b) the double angle method; c) the Jacquet Blondel method; d) a hybrid of double angle method (Q^2) and electron method (x).

The double angle method exhibits the best reconstruction resolution for the kinematic variables x and Q^2, and has therefore been chosen for this analysis. However, for the reconstruction of y the Jacquet Blondel method provides the best reconstruction accuracy and has therefore been chosen. Migration effects are small for events in the region $Q^2 > 10\,GeV^2$, $x > 0.0003$ and $y > 0.04$. Statistics are low for $Q^2 > 1280\,GeV^2$ and $x > 0.1$. Therefore this analysis is restricted to the central kinematic range defined by these cuts.

The acceptance of the event selection cuts for DIS events in the selected kinematic range has been determined to be $\sim 87.7\,\%$ with ME+PS and CDM+BGF MC sample

(87.6 % and 87.8 % respectively). 147934 events of the data sample remain after the final DIS selection cuts. The final DIS event selection cuts are summarized in table 6.1.

Event Selection Criteria	
DST selection	NC DIS bit B14
Vertex cut	$-42\,cm < z_{VTX} < 48\,cm$
$E - p_z$ cut	$35\,GeV < E - p_z < 60\,GeV$
Electron cuts	EEXOTIC electron with $E_{e'} > 5\,GeV$
	$y_{el} < 0.95$
Selected Kinematic Range	
$10\,GeV^2 < Q^2_{DA} < 1280\,GeV^2$	
$0.0003 < x_{DA} < 0.1$	
$y_{JB} > 0.04$	

Table 6.1: *DIS Event Selection Cuts.*

7

RECONSTRUCTION OF K^0_S AND Λ

Neutral strange particles are detected in the decay channels $K^0_S \to \pi^+\pi^-$ and $\Lambda \to p\pi^-$ ($\bar{\Lambda} \to \bar{p}\pi^+$) by reconstructing the tracks of their charged decay products inside the tracking detectors. The K^0_L has a longer lifetime than the K^0_S, in fact only less than 10 % of the K^0_L decay inside the ZEUS detector. Furthermore, the main K^0_L decay branches are 3 body decays (see A.1.1) including neutral pions or neutrinos in the decay products. This makes the reconstruction very complicated and not feasible within the 1994 DIS data sample.

This analysis uses the VCTRAK tracking package (see section 3.4). It determines the event (or primary) vertex and the parameters defining the trajectory and momentum of the charged particles traversing the CTD and VXD and stores this information in ADAMO tables. Of importance for this analysis are the tables VCTVTX containing the coordinates of the primary vertex, VCTRHL and VCTPAR where the information for the individual tracks are stored. The difference between VCTRHL and VCTPAR is that the former contains all reconstructed tracks while the latter is restricted to tracks emanating from the primary vertex.

In the following sections the naming convention as below is used.

Daughter Track: All tracks are assumed to originate from particle decays and are henceforth referred to as daughter tracks.

Daughter Particle: A mass hypothesis assigned to a daughter track defines a daughter particle.

Mother Particle: Daughter particles are combined to form mother particles. Most

of these combinations are completely random. But still they will, for simplicity, be henceforth referred to as mother particles although they are not connected to a physical particle (*i.e.* the tracks are not associated with the same particle decay and/or to a decay at all).

Candidate: A candidate is defined as any mother particle that passes all reconstruction and selection criteria applied to it.

True Particle/Background: Depending on the quality of the reconstruction and selection criteria the candidate sample is contaminated by a certain amount of background. The background can originate either from decays of particles other than the ones under study or from random combinations. In MC samples the nature of each candidate is known and therefore a further distinction of the candidates into the true particles (*i.e.* K^0_S, Λ^0) and background is possible.

7.1 *The Reconstruction of Candidates*

To find candidates for neutral strange particle (or any other decaying neutral particle) the V0FIND (see [Mat94]) routine from the PHANTOM library is used. The lifetime of the neutral strange particles is of the order $\mathcal{O}(10^{-10}\,s)$ which implies that they should decay well away from the primary vertex. V0FIND combines pairs of tracks to find these secondary decay vertices.

The algorithm used by V0FIND needs the magnetic field information of the central tracking area. A mapping of the field is provided in form of a data base (see [Cor92]). The axial magnetic field in the central tracking detector forces the charged particle on helical trajectories along the z-axis. Therefore in a projection onto the xy-plane these trajectories appear as circles. From the information stored in the VCTRHL table the radii and centers of these circles can be determined and an attempt to calculate their intersects is done. The intersection of circles in a plane gives 4 different classes of solutions :

1.) The circles touch each other leading to one "crossing point" that is identified

as the secondary vertex.

2.) The circles intersect at two crossing points. To decide which of these two defines the secondary vertex the longitudinal separations Δz at the crossing points are calculated. The crossing point with the smaller Δz is taken as the secondary vertex.

These are the uncritical solutions that are obviously expected for a decay process. However, there are two additional possibilities where the circles do not intersect.

3.) One circle is completely inside the other circle.

4.) The two circles are completely separate.

Because of resolution effects, these non-intersecting tracks might still belong to a valid combination. Therefore V0FIND calculates for these cases the closest approach of the circles and uses this point as the intersect. The momenta of the daughter tracks are then calculated at the intersect. In addition the four-momentum of the mother particle is evaluated, assuming specific mass hypotheses for each daughter track.

The output of V0FIND contains the momenta of the daughter tracks at the intersect, the coordinates of the intersect in the xy-plane, the two z positions of the intersect of each daughter track and the four-momentum of the mother particle. Furthermore a control flag is returned which provides information on the vertex finding procedure (*i.e.* whether the tracks intersected, or whether the tracks had opposite charge, etc.).

Since the daughter particles must have opposite charge, V0FIND is used to calculate for each event only the intersects of all possible combinations of oppositely charged tracks. As a further requirement, the daughter tracks must have a polar angle in the range $20° < \theta < 160°$ ($|\eta| < 1.75$) and a minimum transverse momentum p_t of 150 MeV. These requirements are henceforth referred to as "Foster cuts" and were recommended for the 1994 run period by the ZEUS tracking group ([Fos95]). They ensure that the reconstruction is restricted to an area where the detector performance as well as the reconstruction efficiency and resolution are well understood. To form

K^0_S candidates for both tracks the pion mass is used as the mass hypothesis. In case of the Λ^0 decay the mass hypothesis is not unambiguous. The positive (negative) charged track might belong to the p (π^-) from a Λ decay or to the π^+ ($\bar{p}$) of the $\bar{\Lambda}$ decay. However, if the Λ^0 has a momentum higher than 300 MeV the maximum momentum of the pion is always lower than the minimum momentum of the proton. Therefore the higher momentum track is given the proton mass hypothesis while the other track is assigned the pion mass hypothesis. With this a distinction between a Λ and a $\bar{\Lambda}$ is possible too : if the higher momentum track has positive charge it belongs to a Λ.

MC studies showed that around 25% of all track combinations do not intersect. These studies also showed that less than 5% of the reconstructed K^0_S and less than 8% of the reconstructed Λ^0 have non intersecting tracks. Therefore combinations that do not intersect are excluded in this analysis.

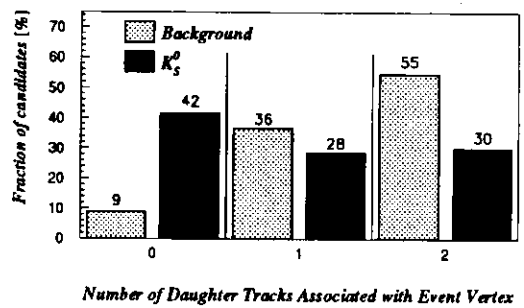

Figure 7.1: *Fraction of K^0_S candidates as function of the number of daughter tracks associated with the event vertex for K^0_S and background with invariant mass $0.4\,GeV < m(\pi^+\pi^-) < 0.65\,GeV$. Candidates with two daughter tracks associated with the event vertex are rejected.*

Most of the tracks in an event are related to strong interactions in the fragmentation process following the hard interaction. The vertex finding algorithms are not able to resolve their separation from the event vertex. Therefore, these tracks are associated with the event vertex, i.e. the tracks appear in both ADAMO tables VCTRHL and VCTPAR. The K^0_S and Λ^0 on the other hand decay on average a few

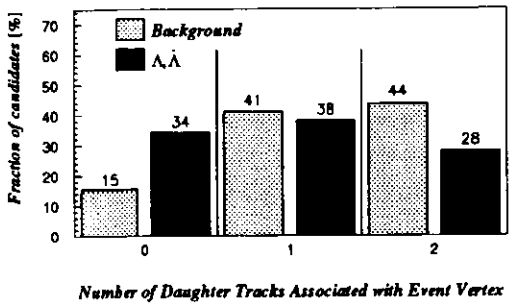

Figure 7.2: *Fraction of Λ candidates as a function of the number of daughter tracks associated with the event vertex for Λ^0 and background with invariant mass $1.08\,GeV < m(p\pi^-, \bar{p}\pi^+) < 1.18\,GeV$. Candidates with at least one daughter track associated with the event vertex are rejected.*

centimeters away from the event vertex. Their daughter tracks are only associated with the primary vertex by resolution effects and random projection accidents. Monte Carlo studies confirm that for K^0_S the daughter tracks are less likely to originate from the primary event vertex than are the daughter tracks from background. Figure 7.1 shows the percentages for K^0_S and background that have either no, one or both daughter tracks emanating from the event vertex. Rejecting all candidates that have two daughter tracks associated with the event vertex reduces the background to less than 50% while keeping $\sim 70\%$ of the K^0_S. For the Λ^0 the number of daughter tracks that are allowed to emanate from the event vertex has been reduced to zero. Figure 7.2 shows that this implies a rather drastic reduction of the signal by $\sim 66\%$ as well as of the background by $\sim 85\%$. The decay proton usually carries most of the Λ^0's momentum and therefore closely follows its original direction. This projection accident associates the proton track with the primary vertex and therefore is the reason for this strong reduction of the signal. However, this cut is retained in order to achieve a reasonable signal to background ratio.

The sample of K^0_S candidates is the set of all remaining candidates with the invariant mass restricted to $0.4\,GeV < m(\pi^+\pi^-) < 0.65\,GeV$. Similarly, the Λ^0 candidate sample contains all candidates with an invariant mass of $1.08\,GeV < m(p\pi^-, \bar{p}\pi^+) < 1.18\,GeV$. At this stage these samples are still highly contaminated by background.

The aim of the following sections, 7.2 and 7.3, is to introduce a set of selection criteria that allow extraction of a clean signal for the neutral strange particles by reducing the background. To determine reasonable cut values, the efficiency and purity of the strange particle selection is studied with the help of known MC samples.

The efficiency as a function of a cut value is defined as :

$$Efficiency(cut) = \frac{n^{part.}_{rec.}(cut)}{n^{part.}_{true}}$$

where $n^{part.}_{rec.}$ is the total number of reconstructed true particles (either K^0_S or Λ^0) and $n^{part.}_{rec.}(cut)$ is the number of reconstructed true particles passing the cut. The purity as a function of a cut value is defined as :

$$Purity(cut) = \frac{n^{part.}_{rec.}(cut)}{n_{rec.}}$$

where $n_{rec.} = n^{part.}_{rec.} + n^{backg.}_{rec.}$ is the number of all reconstructed candidates and background. $n^{part.}_{rec.}(cut)$ is as above. In choosing the number of reconstructed true particles rather than the number of generated true particles as the reference number, the global acceptance of the detector for finding these particles is unfolded.

A compromise between efficiency and purity has to be made in order to find the optimum cut value. Depending on the nature of the study, either equal or different weighting for efficiency and purity can be considered. An illustration of the gain in background reduction can then be achieved in displaying the "compromise function" $Comp(cut) = Efficiency^m(cut) * Purity^n(cut)$ where m, n denote the weights for either function. The maximum of this compromise function (if existing) indicates an optimum choice for the cut value. However, the compromise functions should merely be understood as a help in understanding the variations as function of the cut rather than as an analytical way to determine exactly the best cut value. In this analysis an equal weighting (*i.e.* $m = n = 1$) for purity and efficiency has been chosen to help finding reasonable cut values. Variations in the choice of the selected cut values are included in studies of systematic effects.

7.2 K^0_S Selection

7.2.1 The Δz Cut

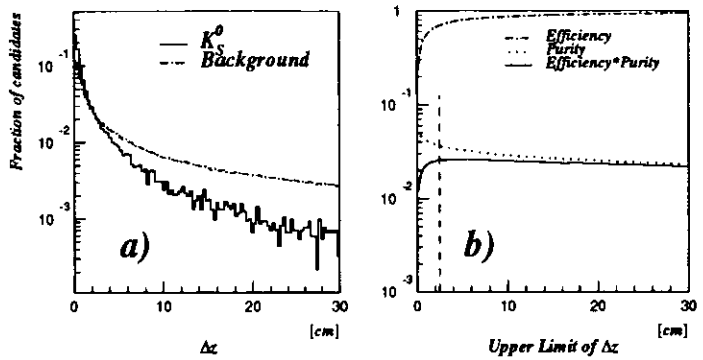

Figure 7.3: *Longitudinal separation Δz : a) Distributions for K^0_S and background with invariant mass $0.4\,GeV < m(\pi^+\pi^-) < 0.65\,GeV$. ; b) Efficiency, purity and compromise function as functions of the upper limit cut in Δz. $\Delta z < 2.5\,cm$, indicated by the dashed line, has been chosen for this analysis.*

Δz is the absolute value of the longitudinal separation between the two tracks at the intersection point. For track combinations originating from a decay vertex one would naïvely expect Δz to vanish assuming an ideal resolution for the tracking device. In real life Δz depends on the longitudinal resolution of the CTD (see 3.3). Furthermore V0FIND assumes ideal helices as trajectories for the daughter particles and therefore does not take into account deviations due to scattering processes along the path (*i.e.* interactions with gas molecules, the beam pipe, wires or the frame material). These effects lead to a smearing in Δz. However, the distribution of Δz for K^0_S is narrower than for background as can be seen from figure 7.3a). Figure 7.3b) shows the effect of changing the upper limit of the Δz cut on efficiency and purity. In addition the compromise function is shown. An upper limit of $\Delta z = 2.5\,cm$ has been chosen. This value is close to the optimum suggested from the compromise function (*i.e.* its maximum at $\Delta z \sim 5\,cm$) but far enough away from the strong drop

off at small Δz to ensure robustness (*i.e.* small dependence on small variations of Δz). The Δz distribution can be approximated fairly well with a double Gaussian centered around 0 (normalized $\chi^2 \sim 1.9$ for the full range $0\,cm < \Delta z < 30\,cm$). The first Gaussian dominates strongly for $\Delta z < 5\,cm$ and yields a rough estimate for the z-resolution $\sigma_z \sim 6\,mm$ of the CTD. This is in fair agreement with the resolution quoted in section 3.3. The second Gaussian is added in order to take care of effects due to multiple scattering, etc. . Adding more Gaussians leaves the width of the first Gaussian unchanged and therefore supports its interpretation as the resolution in z.

7.2.2 The Collinearity Cuts

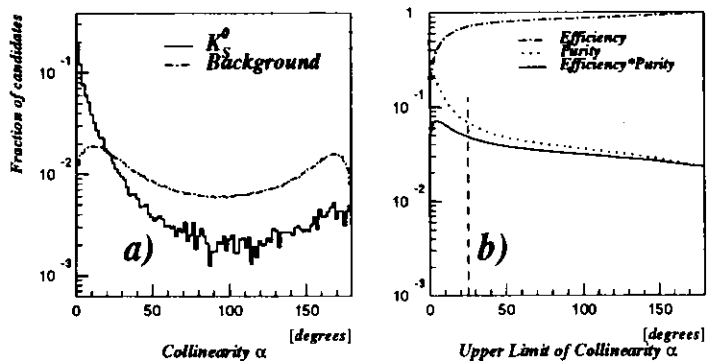

Figure 7.4: *Collinearity α: a) Distributions for K^0_S and background with invariant mass $0.4\,GeV < m(\pi^+\pi^-) < 0.65\,GeV$. ; b) Efficiency, purity and compromise function as function of the upper limit allowed for α. The requirement for this analysis is $\alpha < 25°$ as indicated by the dashed line.*

Assuming that the K^0_S is produced at the primary vertex, *i.e.* not coming from a secondary decay (*e.g.* ϕ decay), it is possible to reconstruct the direction of flight of the K^0_S : since it is a neutral particle it will pass undeflected on a straight line from the primary vertex to its decay point. Both points are reconstructed and therefore the vector of the direction of flight can be determined. For reconstructed K^0_S this direction of flight should match the direction of the 3-momentum of the mother particle

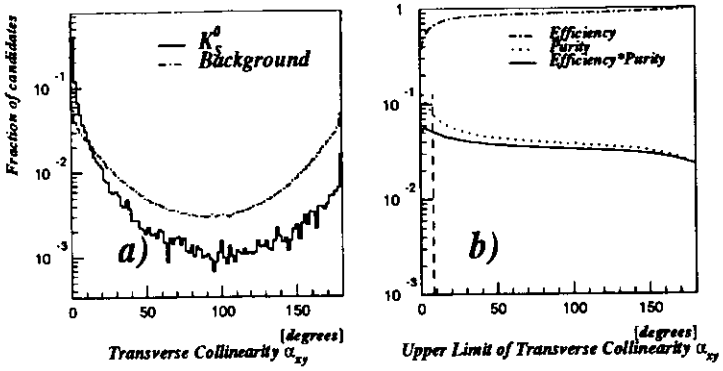

Figure 7.5: *Transverse collinearity α_{xy}: a) Distributions for K^0_S and background with invariant mass $0.4\,GeV < m(\pi^+\pi^-) < 0.65\,GeV$. ; b) Efficiency, purity and compromise function as function of the upper limit allowed α_{xy}. In this analysis $\alpha_{xy} < 8°$ (dashed line) is required.*

reconstructed from V0FIND. For background no correlation is expected. A useful variable to suppress background is therefore the collinearity α which is defined as the angle between these two vectors. Since the resolution in the transverse plane is better than in the longitudinal direction the transverse collinearity α_{xy} is introduced. It is defined as the angle between the projections of the two vectors onto the xy-plane. Figures 7.4 a) and 7.5 a) show the distributions of K^0_S and background for α and α_{xy}, respectively. As expected the collinearity angle distribution for K^0_S peaks much stronger at small angles than the distribution for the background. Figures 7.4 b) and 7.5 b) demonstrate the effect of changes in the upper limits on the efficiency and purity. For the collinearity α an upper limit of 25° has been chosen, the requirement for the transverse collinearity α_{xy} is an angle smaller than 8°.

The shape of the collinearity distributions for the background arises from combinatoric reasons. Naïvely one would expect a flat distribution if the tracks where distributed isotropically. However, in DIS the scattered quark will fragment into a collimated jet of particles defining an axis along the original direction of the quark and through the event vertex. The tracks of the charged particles within the jet will

be associated with the event vertex and therefore the intersects will be close to it, preferably on the axis. The track resolution will allow intersects on either side of the vertex, hence populating the α_{xy} distribution at values of $\sim 0°$ and $\sim 180°$ degrees. In case of the collinearity α the z-resolution of the CTD introduces an additional smearing. Combinations with tracks not associated with the jet will contribute to a continuous distribution, but with much less statistical weight. For the K^0_S the (much smaller) peak in the backward direction is also attributed to resolution effects for tracks that intersect too close to the vertex. In removing these tracks the backward collinearity region gets depopulated.

7.2.3 *The Lifetime Related Cuts*

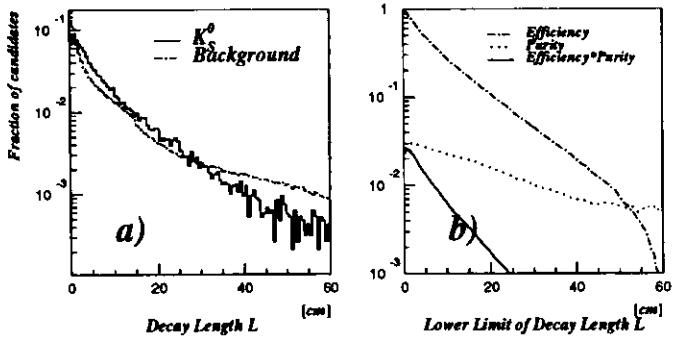

Figure 7.6: *Decay length L: a) Distributions for K^0_S and background with invariant mass $0.4\,GeV < m(\pi^+\pi^-) < 0.65\,GeV$. ; b) Efficiency, purity and compromise function as functions of a lower limit in the decay length L. No cut in L is applied in this analysis.*

Due to their lifetime the K^0_S have an average decay length L of a few centimeters which corresponds to the distance between the primary vertex and the secondary vertex found with V0FIND[1]. It turned out, however, that a cut on the decay length is not effective in suppressing background. From figure 7.6 a), which shows the decay

[1]This variable makes physical sense only for real decay particles.

length distribution for K^0_S and background, it can be seen that both distributions are very similar. Figure 7.6 b) shows the effect on efficiency and purity as function of a lower limit in the decay length L. It is obvious that there is no gain in applying this cut since both efficiency and purity are falling with increasing cut lower limit in L. A study using the transverse decay length, which is defined as the projection of the decay length onto the xy-plane, showed the same behaviour. Therefore none of these was used in this analysis.

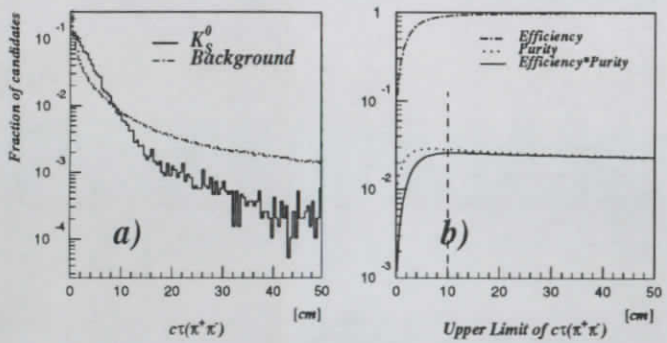

Figure 7.7: *Proper lifetime $c\tau$: a) Distributions for K^0_S and background with invariant mass $0.4\,GeV < m(\pi^+\pi^-) < 0.65\,GeV$. ; b) Efficiency, purity and compromise function as a function of an upper limit of in $c\tau$. The requirement for this analysis is $c\tau < 10.0\,cm$ as indicated by the dashed line.*

From the decay length, L, the three-momentum (both in the laboratory frame) and the invariant mass $m(\pi^+\pi^-)$ of the candidate the proper lifetime $c\tau$ can be calculated as

$$c\tau = \frac{L \cdot m(\pi^+\pi^-)}{|\vec{p}|}.$$

As for the decay length a physical interpretation is only applicable for real decay particles. Figure 7.7a) shows the $c\tau$ distribution for K^0_S and background. The lifetime distribution for K^0_S drops much faster than for background. Figure 7.7 b) demonstrates the effect of changing the upper limit allowed for $c\tau$ on efficiency and purity. A cut value of $c\tau < 10\,cm$ has been chosen for this analysis which is well above the

world average proper lifetime of $2.675\,cm$ (see appendix A.1.1).

7.3 Λ^0 Selection

The selection of the Λ^0 particles proceeds in a way similar to the K^0_S selection. In fact the same set of selection criteria has been applied in order to extract a clean Λ^0 signal. Figures 7.8 – 7.12 show the distributions for the Λ^0 study. Again no cut in the decay length L is applied, the cut values for Δz, α, α_{xy} are kept the same as for the K^0_S analysis. The cut in $c\tau = L \cdot m(p\pi)/|\vec{p}|$ has been increased to $40\,cm$ to take into account the longer mean life time of the Λ^0 ($7.89\,cm$, see appendix A.1.2).

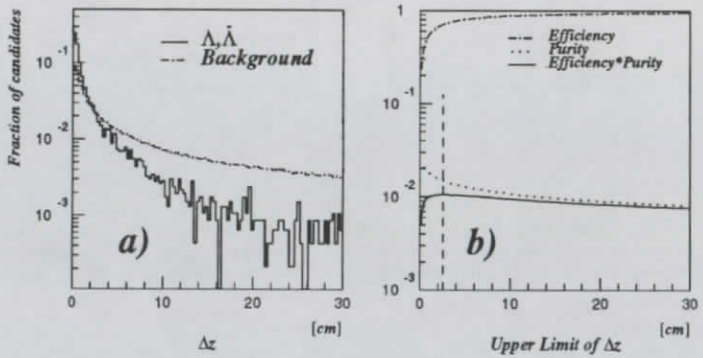

Figure 7.8: *Longitudinal separation Δz : a) Distributions for Λ^0 and background with invariant mass $1.08\,GeV < m(p\pi^-, \bar{p}\pi^+) < 1.18\,GeV$. ; b) Efficiency, purity and compromise function as functions of an upper limit allowed for Δz. $\Delta z < 2.5\,cm$ (dashed line) is required for this analysis.*

7.4 The K^0_S and Λ^0 Samples

Figure 7.13 *a*) shows the distribution of the $m(p\pi)$ versus the $m(\pi\pi)$ mass hypotheses for the candidates from the 1994 DIS data sample in the range $0.2\,GeV \leq m(\pi\pi) \leq 0.8\,GeV$ and $1.05\,GeV \leq m(p\pi) \leq 1.35\,GeV$. The candidates contributing to this figure have passed all but two of the reconstruction and selection requirements mentioned above. The exemptions are that the mass ranges are widened for both hy-

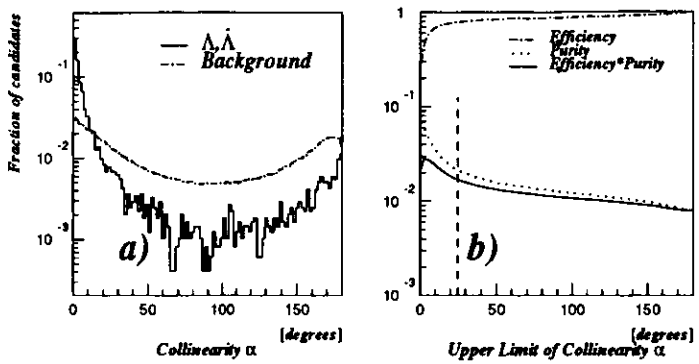

Figure 7.9: *Collinearity α: a) Distributions for Λ^0 and background candidates with invariant mass $1.08\,GeV < m(p\pi^-, \bar{p}\pi^+) < 1.18\,GeV$. ; b) Efficiency, purity and compromise function as function of an upper limit allowed for α. The cut $\alpha < 25°$ is indicated by the dashed line.*

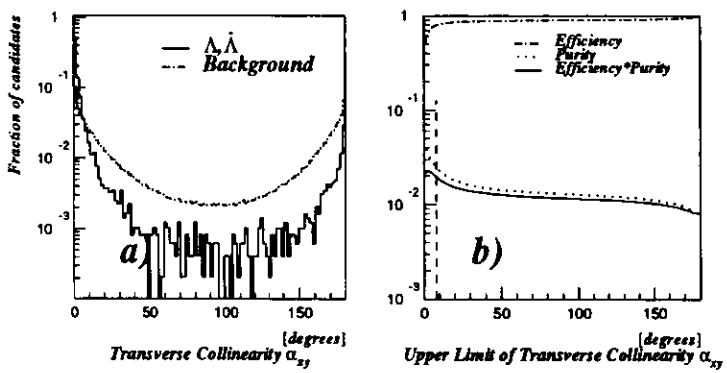

Figure 7.10: *Collinearity α_{xy}: a) Distributions for Λ^0 and background candidates with invariant mass $1.08\,GeV < m(p\pi^-, \bar{p}\pi^+) < 1.18\,GeV$. ; b) Efficiency, purity and compromise function of an upper limit allowed for α_{xy}. The requirement for this analysis is $\alpha < 25°$ as indicated by the dashed line.*

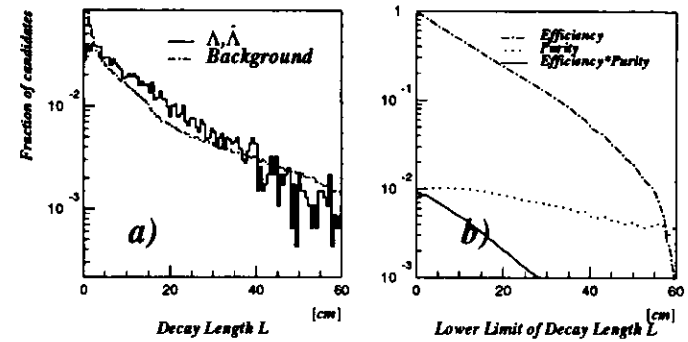

Figure 7.11: *Decay length L: a) Distributions for Λ^0 and background candidates with invariant mass $1.08\,GeV < m(p\pi^-, \bar{p}\pi^+) < 1.18\,GeV$. ; b) Efficiency, purity and compromise function as functions of a lower limit in the decay length L. No cut on L is applied in this analysis.*

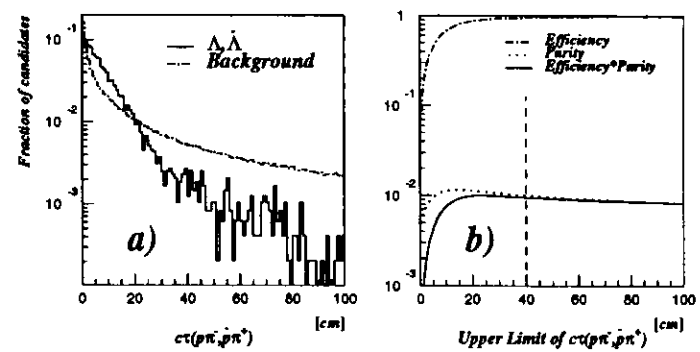

Figure 7.12: *Proper lifetime cτ : a) Distributions for Λ^0 and background candidates with invariant mass $1.08\,GeV < m(p\pi^-, \bar{p}\pi^+) < 1.18\,GeV$. ; b) Efficiency, purity and compromise function as functions of an upper limit in cτ. The requirement for this analysis is $c\tau < 40.0\,cm$ as indicated by the dashed line.*

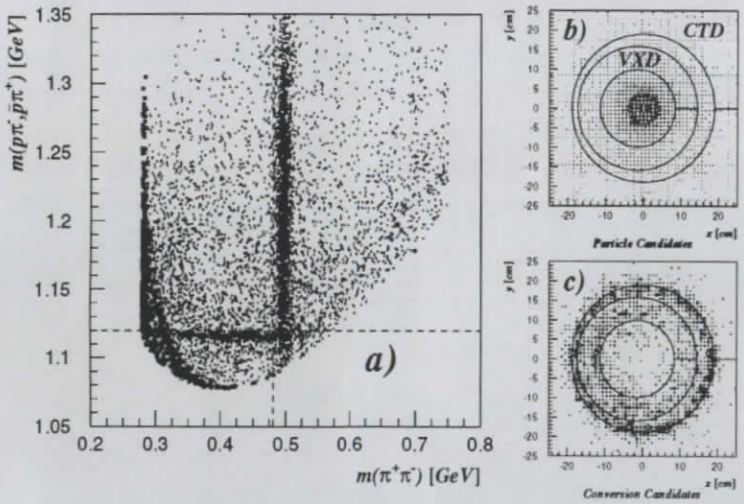

Figure 7.13: *a) Invariant masses of candidates for two daughter particle combinations assuming a $p\pi$ versus a $\pi\pi$ mass hypothesis. The dashed lines indicate the "anti-Λ^0" and "anti-K^0_S" cuts. Squares indicate candidates probably arising from photon conversion $\gamma \to e^+e^-$, which are rejected. Conversion photons can be separated with a limit in the invariant mass $m(ee) < 50\,MeV$ (electron positron hypothesis). Figures b) and c) show the distribution of the reconstructed decay vertices in the xy-plane for particle candidates and photon conversion candidates, respectively. The coordinates follow the ZEUS convention, the circles indicate the geometric boundaries of the VXD and CTD.*

potheses and the $c\tau$ cut for the K^0_S has been raised to $17.8\,cm$ (which corresponds to the $c\tau = 40\,cm$ cut for the Λ^0). A clear signal band for the K^0_S and the Λ^0 can be seen at the expected mass values. Still a lot of candidates are spread out beyond the mass peak regions and are attributed to background. It also can be seen from figure 7.13 that the sample of K^0_S candidates is contaminated by Λ^0 particles and vice versa. To reduce this contamination an "anti-Λ^0 cut" is applied to the K^0_S sample, rejecting all candidates with an invariant mass $m(p\pi) < 1.12\,GeV$. For the Λ^0 sample a cut in the invariant mass $m(\pi\pi) > 0.481\,GeV$ is applied in order to reduce the contamination with K^0_S. These cuts are shown as dashed lines in figure 7.13 *a*). A special class of background originates from photon conversion : a photon incident on the detector material can convert into an electron positron pair, $\gamma \to e^+e^-$. The reconstructed tracks of the electron positron pair can fake candidates for neutral strange particle decays. As Monte Carlo studies showed, this background can be reduced by rejecting candidates that have an invariant mass $m(ee) < 50\,MeV$. Figures 7.13 *b*) and *c*) show the distribution of reconstructed decay vertices for the candidates in a projection into the *xy*-plane (using the ZEUS coordinate convention). In this graphic representation the number of candidates in a given *xy* bin is proportional to the size of the box in this bin. The geometric borders of the VXD and CTD are indicated as circles. The decay vertex distribution for candidates with $m(ee) > 50\,MeV$, figure 7.13 *b*), is strongly peaked around the nominal vertex, where no detector material can give rise to the photon conversion process. Candidates with $m(ee) < 50\,MeV$, figure 7.13 *c*), have decay vertices that are distributed around the support structure of the VXD and CTD, confirming the photon conversion hypothesis. The photon conversion candidates, indicated as squares in figure 7.13 *a*), are rejected with the $m(ee) > 50\,MeV$ selection criteria.

Table 7.1 lists all reconstruction and selection criteria applied in this analysis to the events from the DIS data sample in order to extract a clean signal of K^0_S and Λ^0 particles.

Figure 7.14 shows the invariant mass distributions for the final K^0_S sample. The

Reconstruction Criteria	K^0_S & Λ^0	
Daughter track requirements	opposite charges tracks intersect $p_t > 0.15\,GeV$ $20° < \theta < 160°$	
Tracks associated with primary vertex	≤ 1 (K^0_S) ; 0 (Λ^0)	
Selection Criteria	K^0_S	Λ^0
Δz	$< 2.5\,cm$	$< 2.5\,cm$
Collinearity angle	$< 25°$	$< 25°$
Transverse collinearity angle	$< 8°$	$< 8°$
Proper life time $c\tau$	$< 10\,cm$	$< 40\,cm$
$m(p\pi)$	$> 1.12\,GeV$	-
$m(\pi\pi)$	-	$< 0.481\,GeV$
$m(ee)$	$> 0.05\,GeV$	$> 0.05\,GeV$

Table 7.1: *K^0_S and Λ^0 Reconstruction and Selection Criteria*

results quoted are obtained from a fit to the data of a Gaussian shaped signal plus a linear background distribution. The fitted mass is $m(K^0_S) = 497.11 \pm 0.08\,MeV$ and the width is $\sigma(K^0_S) = 6.4 \pm 0.1\,MeV$. The width is totally dominated by the resolution of the tracking system which cannot resolve the natural width of the K^0_S particles. The world average mass for the K^0_S quoted in [Par96] (or see table A.1 in A.1.1) is $m(K^0_S) = 497.671 \pm 0.031\,MeV$. The Gaussian cannot reproduce completely the shape of the signal and therefore more sophisticated methods will be discussed in section 8.1. At this point the fit suggests a total of 7468 K^0_S and 804 background candidates in the signal region. The resulting signal to background ratio is of the order 9:1. The boundaries of the signal region are given by the nearest bin boundaries of the histogram which include $\pm 2.5\,\sigma$ around the fitted centre of the mass peak.

Figure 7.15 a) shows the invariant mass distribution for the final Λ^0 sample. Again

the data points are fitted with a Gaussian shaped signal plus linear background distribution. As a result the fitted mass of $m(\Lambda^0) = 1116.0 \pm 0.1\,MeV$ and the width $\sigma(\Lambda^0) = 2.2 \pm 0.1\,MeV$ have been obtained. [Par96] (or see table A.2) quote the world average mass as $m(\Lambda) = 1115.63 \pm 0.05\,MeV$. The number of reconstructed Λ^0 particles obtained by this fit is 691 Λ^0 and 79 background candidates which corresponds to a signal to background ratio of 8:1. As mentioned before in section 7.1 the Λ and $\bar{\Lambda}$ can be distinguished. Figures 7.15 b) and c) show the invariant mass distributions for the Λ and $\bar{\Lambda}$ candidates separately. Applying the fit to each of these distributions yields the consistent masses $m(\Lambda) = 1115.9 \pm 0.1\,MeV$ and $m(\bar{\Lambda}) = 1116.2 \pm 0.1\,MeV$. The widths are $\sigma(\Lambda) = 2.3 \pm 0.1\,MeV$ and $\sigma(\bar{\Lambda}) = 2.2 \pm 0.2\,MeV$. The yield is roughly 12 % higher for Λ (371 and 36 background) than for $\bar{\Lambda}$ (329 and 31 background) candidates.

That the results for the masses are not in agreement with world average values is due to the resolution of the reconstructed daughter track momenta. However, the aim of this thesis is not a high accuracy determination of the strange particles masses. Although this resolution effect leads to a discrepancy of $\sim 7\sigma$ in the masses, the absolute discrepancy is is only a per mille effect and the overall influence on the distributions under study is negligible.

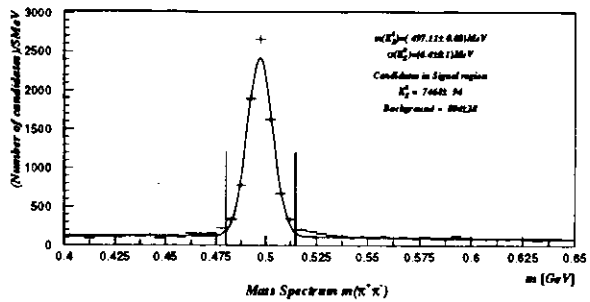

Figure 7.14: *Invariant mass distribution $m(\pi^+\pi^-)$ of reconstructed K^0_S candidates.*

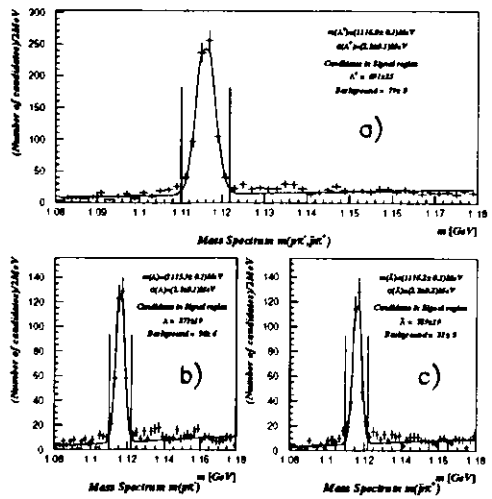

Figure 7.15: *Invariant mass distributions for a) Λ^0 candidates. b) and c) show the distributions for Λ and $\bar{\Lambda}$ candidates separately.*

8

Data Correction Technique

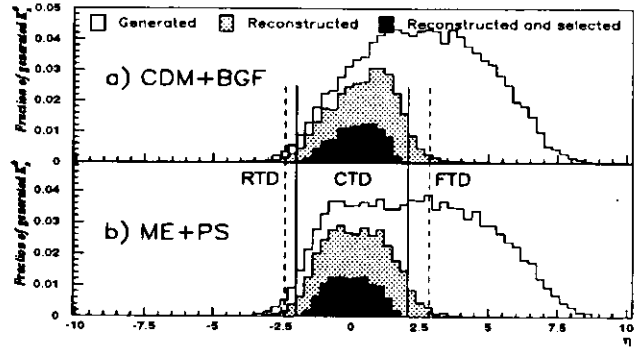

Figure 8.1: *η distributions for generated, reconstructed and selected K^0_S particles in a) CDM+BGF and b) ME+PS Monte Carlo samples. The solid lines indicate the geometrical acceptance of the CTD only, the dashed lines correspond to the widened geometrical acceptance including FTD and RTD.*

In order to be able to extract rates associated with the particle production an adequate method to count the reconstructed particles and determine the background within the sample is necessary. Different methods to extract these numbers are discussed in section 8.1. However, the numbers of reconstructed particles do not immediately reflect the true number of particles that were created in the interaction. The reconstruction of the neutral strange particles is limited by the geometric acceptance of the tracking detector, the efficiencies of the track finding algorithms and the reconstruction and selection criteria for the particles. As an illustration, figures 8.1, 8.2 and 8.3 show the influence of these factors on the pseudorapidity distributions for K^0_S, Λ and $\bar{\Lambda}$

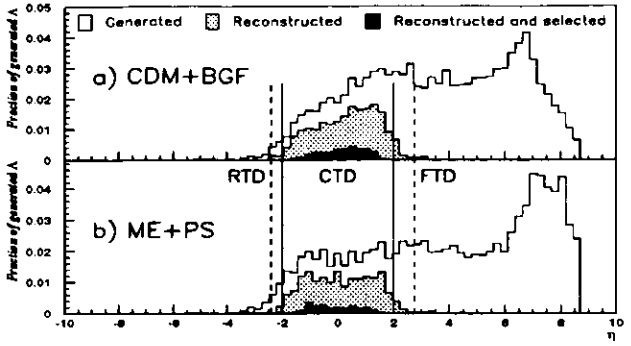

Figure 8.2: *η distributions for generated, reconstructed and selected Λ particles in a) CDM+BGF and b) ME+PS Monte Carlo samples. The solid lines indicate the geometrical acceptance of the CTD only, the dashed lines correspond to the widened geometrical acceptance including FTD and RTD.*

respectively, as simulated with the ME+PS and CDM+BGF Monte Carlo models.

The spectra are the predictions for the neutral strange particles of those MC events that pass all event selection criteria as introduced in section 6.4. The unshaded distributions are the spectra at the generator level. The geometric acceptance of the tracking detectors (including track finding efficiency), as indicated by solid and dashed lines for CTD and FTD/RTD respectively, strongly restricts the rapidity range available to reconstruct the neutral strange particles.

The comparison of figures 8.2 and 8.3 shows a different production mechanism for Λ and $\bar{\Lambda}$ in the forward direction : while the $\bar{\Lambda}$ production drops rapidly for $\eta > 5$, the Λ production rises to a peak. This difference is attributed to the different quark content of the Λ and $\bar{\Lambda}$. The Λ is a *uds* quark bound state. In the DIS scattering process it can be produced in the following production mechanisms :

1. The proton is a *uud* quark bound state. If in the hard process an *u*-quark is scattered out of the proton, the remaining *ud*-diquark can recombine with a *s*-quark to form a Λ. In this "pick-up" process the diquark carries the fraction $(1 - x)$ of the proton momentum and no transverse momentum (with respect to the proton direction). The *s*-quark is extracted from the sea and therefore

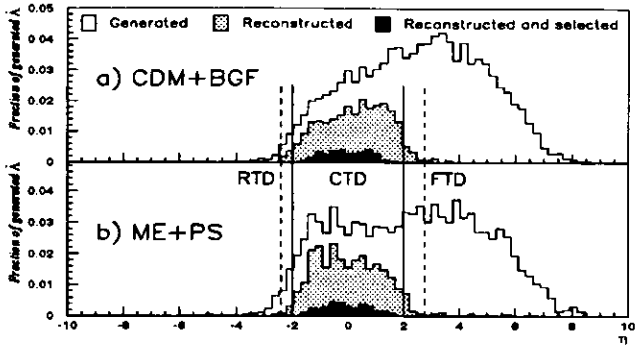

Figure 8.3: *η distributions for generated, reconstructed and selected $\bar{\Lambda}$ particles in a) CDM+BGF and b) ME+PS Monte Carlo samples. The solid lines indicate the geometrical acceptance of the CTD only, the dashed lines the widened geometrical acceptance including FTD and RTD.*

will have only a small momentum. Thus the Λ will predominantly follow the original proton direction and give rise to the peak in the very forward direction $(\eta \sim 7 \Rightarrow \theta = 0.1°)$.

2. The Λ is produced in the fragmentation process of the scattered quark. The fragmentation proceeds between the scattered quark and the proton remnant.

3. Contributions to the Λ production from the decay of heavier baryons produced in the hard process (Σ^0, Ξ, Ω^-, etc.) are negligible.

The $\bar{\Lambda}$ is an antiquark ($\bar{u}\bar{d}\bar{s}$) bound state, so no pick-up process is possible, all of its constituents have to be produced in the fragmentation process. Therefore a similar production rate as for the Λ particle is expected in the scattered quark fragmentation region, but there is no forward peak. The MC samples predict an excess Λ over ($\bar{\Lambda}$) of ~ 30 %. However, due to the strong beam energy asymmetry the ZEUS detector is blind to this excess.

The light grey shaded distributions are the MC predictions for the neutral strange particles that have both daughter tracks reconstructed within the CTD. The acceptances are ~ 34 % and ~ 32 % (K^0_S), ~ 20 % and ~ 17 % (Λ) and ~ 24 % and ~ 26 %

($\bar{\Lambda}$). The two values correspond to the CDM+BGF and ME+PS model respectively. Finally, the dark shaded distributions are the spectra of the neutral strange particles that pass all the reconstruction and selection criteria as summarized in table 7.1. These criteria reflect the efficiency of the reconstruction algorithm, which leads to a further reduction to $\sim 10.5\,\%$ and $\sim 11\,\%$ (K^0_S), $\sim 2\,\%$ and $\sim 3\,\%$ (Λ) and $\sim 2\,\%$ and $\sim 3.5\,\%$ ($\bar{\Lambda}$) with respect to the generated sample. For simplicity the reconstruction efficiency will henceforth be combined with the detector acceptance and will be called the "effective acceptance". In 8.2 further studies of the effective acceptance will be discussed in order to build a correction procedure. The effective acceptances quoted so far were extracted from MC samples using true particles only (*i.e.* the reconstruction algorithm was only applied to track pairs associated with a neutral strange particle) and therefore do not include any background (*e.g.* from random combinations of tracks with approximately the mass of the neutral strange particle under study) in the reconstructed particle sample. The correct nomenclature therefore would be "true effective acceptance", however, the word "true" is omitted for simplicity. The correction procedure applied to particle distributions and the determination of the statistical and systematic errors will be explained in section 8.4.

The predicted ratios of the number of reconstructed Λ to $\bar{\Lambda}$ is $1.13 \pm 0.12, 0.99 \pm 0.13$ for CDM+BGF and ME+PS respectively. The errors reflect the statistical error on the number of the reconstructed particles in the MC event samples. These predictions are in good agreement with the ratio of 1.02 ± 0.08 for the data sample, which is calculated from the reconstructed Λ's and $\bar{\Lambda}$'s as quoted in section 7.4.

8.1 Counting Reconstructed Particles and Background

To count the reconstructed K^0_S or Λ^0 particles, several methods based on a fit to the mass spectra of the candidate samples were tested using MC samples. Although listed here separately, the following items have been applied together but varied independently.

- For the signal shape a Gaussian as well as a double Gaussian shape have been used as fit function. Although the double Gaussian improves the normalized χ^2 from ~ 5 to ~ 2 neither assumption can reproduce completely the shape of the signal. This is mainly due to the resolution of the reconstructed daughter track momenta (the second Gaussian is supposed to absorb these effects). However, the single Gaussian fit is more robust for smaller numbers of candidates in the mass distribution and therefore has been chosen as assumption for the signal shape.

- For the background, polynomials of zeroth to third order were tested. It has been found that the assumption of a linear background is suitable for this analysis, the variation with higher order polynomials was found to be marginal.

- The bin sizes for the mass distributions as well as the fit ranges have been varied. The influence of either was negligible. However, the final choice of the bin size of $5\,MeV$ and $2\,MeV$ for the K^0_S and the Λ^0, respectively was determined from statistical considerations (*i.e.* to have the signal spread over several bins yet still obtain reasonable statistics within a given bin.)

Figure 8.4 shows the results using the fit function

$$f(x) = \frac{p(1) \cdot b}{\sqrt{2\pi} \cdot p(3)} \cdot e^{-0.5(\frac{x - p(2)}{p(3)})^2} + p(4) + p(5) \cdot x \qquad (8.1)$$

for the description of the mass spectra of *a*) K^0_S and *b*) Λ^0 of a MC sample. b is the bin width of the histogram (in MeV). The $p(i), i = 1,5$ are the fit parameters that are returned from the MINUIT ([Jam94]) fitting routine together with their errors $\delta p(i), i = 1,5$. The interpretation of the parameters is as follows :

$p(1)$ is the number of candidates in the signal (on top of the background).

$p(2)$ is the centre of the Gaussian peak.

$p(3)$ is the width of the Gaussian peak.

$p(4)$ is the intercept of the linear background function.

$p(5)$ is the slope of the linear background function.

The Monte Carlo prediction quotes the true number of reconstructed K^0_S (Λ^0) and background inside the signal region. The signal region hereby corresponds to the nearest bin boundaries of the histogram which include $\pm 3\,\sigma$ around the fitted mass peak value. Furthermore the results for two different methods to extract the number of reconstructed particles (n_{part}) and background (n_{bg}) from the fit are quoted :

Method 1 The result for $p(1)$ and its error $\delta p(1)$ from the fit are taken as $n_{part} \pm \delta n_{part}$. $p(1)$, as in equation 8.1, is simply the integral of the Gaussian function. The background, n_{bg}, is the integral over the signal region of the linear background function with parameters $p(4)$ and $p(5)$. The error on the background is simply the statistical error of this integral ($\delta n_{bg} = \sqrt{n_{bg}}$). This is a good approximation to the correct calculation using the errors $\delta p(4)$, $\delta p(5)$ and the error matrix.

Method 2 The result is obtained from an integration of all entries in the signal region, subtracting the integrated background (inside the signal) as calculated in method 1. The error of the integral ($n_{cand} = n_{part} + n_{bg}$) is given as the statistical error on the number of entries ($\delta n_{cand} = \sqrt{n_{cand}}$). The error on the background is again simply the statistical error on the calculated background. n_{part} and n_{bg} are uncorrelated, therefore $\delta n_{part} = \sqrt{(\delta n_{cand})^2 - (\delta n_{bg})^2} = \sqrt{n_{part}}$ (*i.e.* the statistical error on the calculated number of particles).

Figure 8.5 shows the fitted mass values for the K^0_S and Λ^0 as a function of p_t and η. The data points are the results of fits to the invariant mass spectra of all candidates within the corresponding bin. The errors on the data points are the uncertainties in the mass values as obtained from the fit. The dashed lines show the reconstructed invariant masses obtained from a fit to the mass spectra of all candidates in the selected 1994 DIS data sample. This choice of bins leads to approximately equal numbers of candidates within a bin. However, the ratio of signal to background varies over the bins. This variation shows a stronger dependence on p_t than on η. For the K^0_S can-

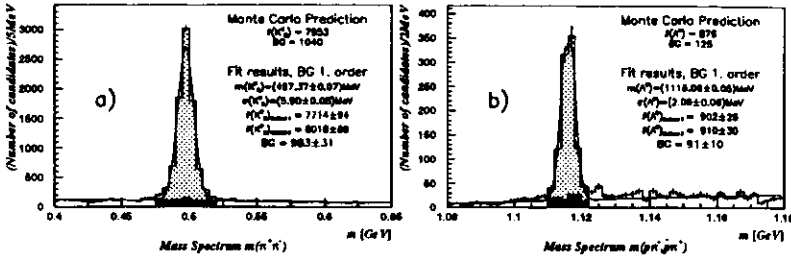

Figure 8.4: Counting *a*) K^0_S and *b*) Λ^0 from fits of the invariant mass spectra using MC events. As fit function a Gaussian signal with linear background is assumed. The MC predictions for the numbers of true particles (grey shaded signal area) and background (dark shaded signal area) as well as the results of the two counting methods are shown.

didates the ratio of signal to background decreases in the higher p_t bins, for the Λ^0 candidates the ratio is worst in the lowest p_t bin and statistics are low in the highest p_t bin. In these bins the fit quality is rather poor and the fit unstable (*i.e.* the result is very sensitive to the starting values of the fit). Disregarding these bins no clear dependence on either p_t or η is evident. The agreement is usually better than $2\,\sigma$, deviations from the "central" value are of the order 0.1 %, as indicated by the dotted lines. The variation in the peak width is smaller than the bin size of the invariant mass histograms. This allows one to keep the centre of the Gaussian peak and the width fixed (parameters $p(2)$ and $p(3)$ in equation 8.1) and thus to reduce the number of free parameters in the fit to three. This enhances the robustness of the fit in bins which have lower statistics. The chosen mass values are the results from the fits to the selected 1994 DIS data sample mass distributions, 497.11 MeV and 1116.0 MeV for the K^0_S and Λ^0 respectively. The widths are 6.4 MeV and 2.2 MeV, respectively, approximately equal to the bin size of the histograms (5 MeV and 2 MeV, respectively). With the widths fixed the signal range can now also be fixed. For the K^0_S the signal range is defined as $475\,MeV \leq m(\pi^+\pi^-) \leq 520\,MeV$. This corresponds to $-3.5/+3.6\,\sigma$. For the Λ^0 the signal range is defined as $1110\,MeV \leq m(p\pi^-, \bar{p}\pi^+) \leq 1122\,MeV$.

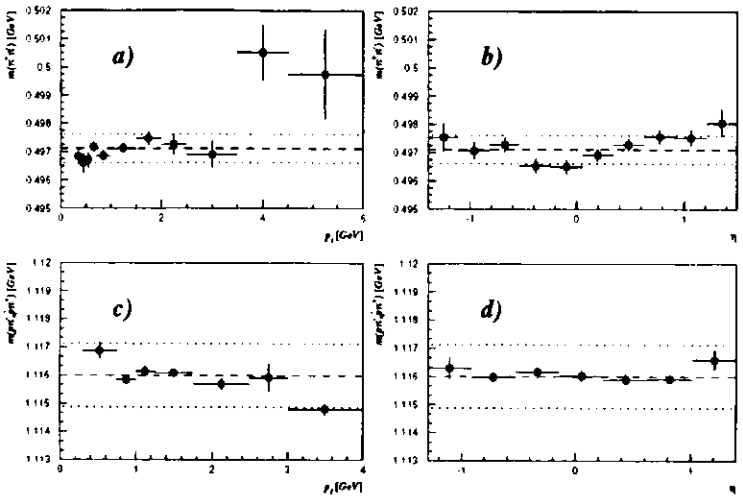

Figure 8.5: Reconstructed invariant mass $m(\pi^+\pi^-)$ as function of *a)* p_t and *b)* η. *c)* and *d)* show the corresponding distributions for the reconstructed invariant mass $m(p\pi^-, \bar{p}\pi^-)$. The data points are the results of fits to the invariant mass spectra, the errors indicate the uncertainties in these mass values. The dashed lines show the reconstructed invariant mass obtained from the fit to the candidates of the selected 1994 DIS data sample, the dotted lines indicate a deviation of 0.1%.

This corresponds to $-2.7/+2.7\,\sigma$. The signal range for the K^0_S has been slightly widened since MC studies show the tails of the signal contain more true particles than a Gaussian would suggest. For the Λ^0 the opposite is the case. However, $\sim 98\%$ of the true particles are contained within the signal ranges quoted above.

The upper parts of figures 8.6 *a)* and *b)* show the numbers of reconstructed K^0_S and Λ^0 which are now obtained from fits with fixed masses and signal widths. The MC predictions for the numbers of true particles, $n_{part,gen}$, are shown as a solid line. The reconstructed numbers, $n_{part,rec}$, for the two counting methods are indicated as triangles with error bars. The lower parts of the figures show the corresponding resolution achieved with the two counting methods. The resolution is defined as $\frac{n_{part,rec}-n_{part,gen}}{n_{part,gen}} \cdot 100\,\%$. In this graphical representation the x-labels on top of the histogram give the η ranges of the bin. The points within such an η range correspond

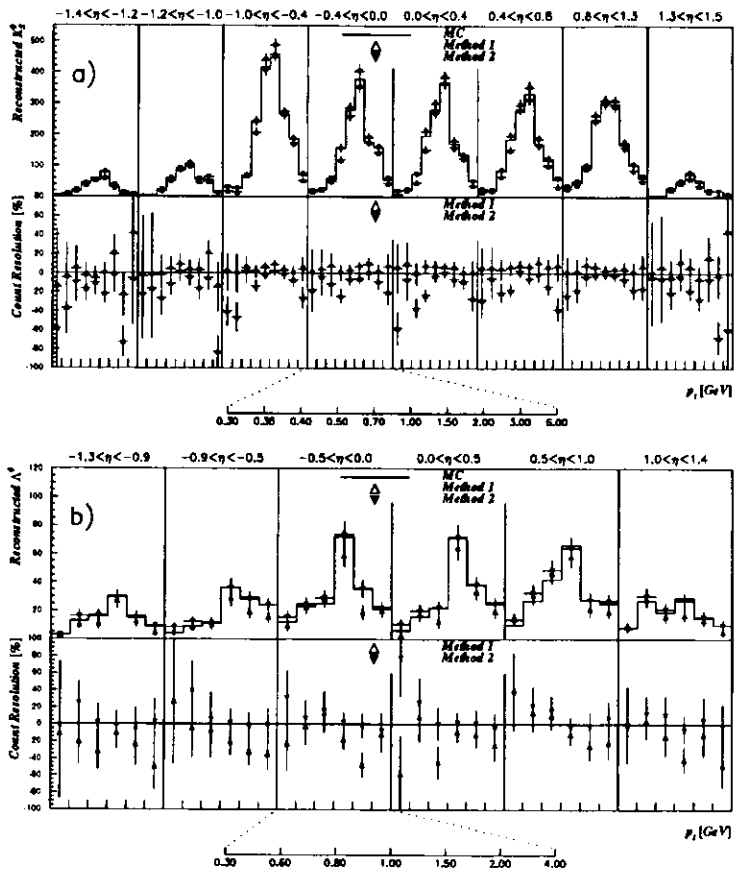

Figure 8.6: Counting *a)* K^0_S and *b)* Λ^0 inside bins of a grid in the p_t-η plane. The x-labels on top of the histogram give the η ranges of the bin. The points within such a range correspond to the p_t bins as defined in the expansion at the bottom of the histogram. As fit function a Gaussian signal with linear background is assumed. The MC predictions for the numbers of true particles as well as the results of the two counting methods are shown in the upper histograms. The lower parts of the figures show the relative error for the two methods with respect to the MC prediction.

to the p_t bins as defined in the expansion at the bottom of the histogram. Note the nonlinear scales for both p_t and η. The reason for choosing this bin definitions will be explained in section 8.4. Within the errors, method 2 shows generally good agreement (usually within 1σ, always better than 2σ) with the true numbers, while the resolution of method 1 varies strongly. Method 1 generally underestimates the true number of particles by 10 – 20% while method 2 reproduces the MC predictions better than 10%. Therefore method 2 has been chosen in this analysis.

Figure 8.7 shows the background estimation within the K^0_S and Λ^0 signal region. The graphical layout and the definition of the resolution follows that of figure 8.6. The agreement with the predictions is generally rather poor, the background is systematically underestimated. For the K^0_S the estimate is usually between 100 % and 50 %, for the Λ^0 usually ~ 50 % too low. More interesting, however, is the purity of the reconstructed particles, defined as :

$$pur = \frac{n_{part}}{n_{part} + n_{bg}} = \frac{n_{part}}{n_{cand}} \tag{8.2}$$

where n_{part} is the number of reconstructed particles, n_{bg} the number of background and $n_{cand} = n_{part} + n_{bg}$ the total number of candidates in the signal region, as before. The errors δn_{part} and δn_{cand} are strongly correlated and therefore the covariance $cov(n_{part}, n_{cand})$ has to be included in the calculation of δpur :

$$\begin{aligned} \delta pur &= \sqrt{\frac{\delta n^2_{part}}{n^2_{cand}} + \frac{n^2_{part}}{n^4_{cand}}\delta n^2_{cand} - \frac{2cov(n_{part}, n_{cand})n_{part}}{n^3_{cand}}} \\ &= \sqrt{\frac{n_{part}}{n^2_{cand}}(1 + \frac{n_{part}}{n_{cand}} - 2\rho\frac{\sqrt{n_{part}}}{\sqrt{n_{cand}}})} \end{aligned} \tag{8.3}$$

$\rho = \frac{cov(n_{part}, n_{cand})}{\delta n_{part}\delta n_{cand}}$ is the correlation between the errors $\delta n_{part} = \sqrt{n_{part}}$ and $\delta n_{cand} = \sqrt{n_{cand}}$. $\rho = 0.95$ (K^0_S) and $\rho = 0.97$ (Λ^0) have been determined from fits to the error distributions.

Figure 8.8 shows the purity estimation for K^0_S and Λ^0. Again the same graphical representation and an equivalent definition for the resolution as in figure 8.6 have been chosen. Due to the strong correlation the errors in n_{part} and n_{cand} cancel mostly. A

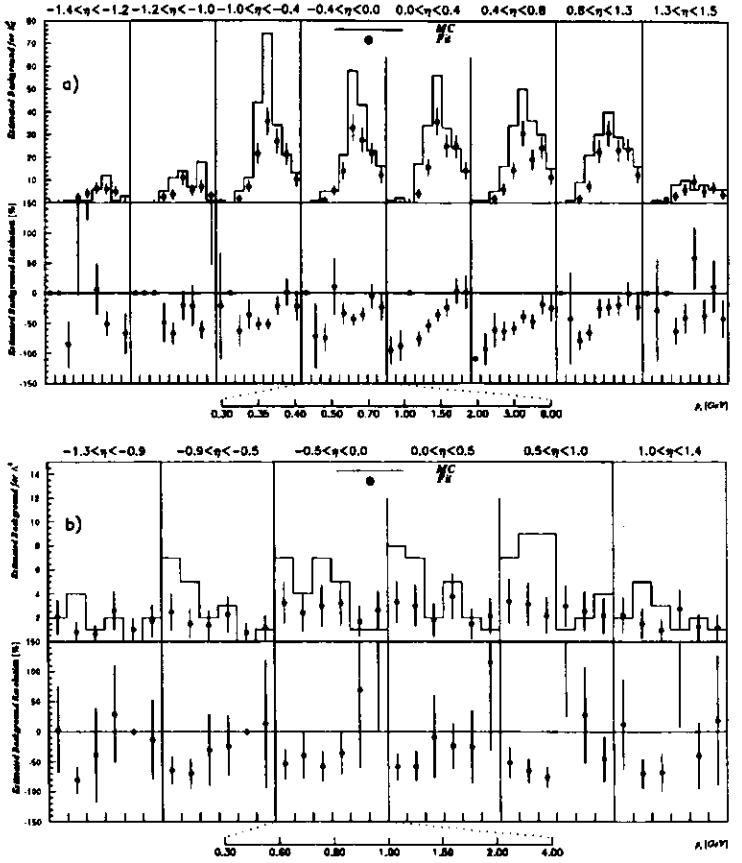

Figure 8.7: Estimated background in the signal region for *a)* K^0_S and *b)* Λ^0 inside bins of a grid in the p_t-η plane. The x-labels on top of the histogram give the η ranges of the bin. The points within such a range correspond to the p_t bins as defined in the expansion at the bottom of the histogram. As fit function a Gaussian signal with linear background is assumed. The MC predictions for the numbers of background inside the signal region as well as the result calculated from the fits are shown in the upper histograms. The lower parts of the figures show the relative error with respect to the MC prediction.

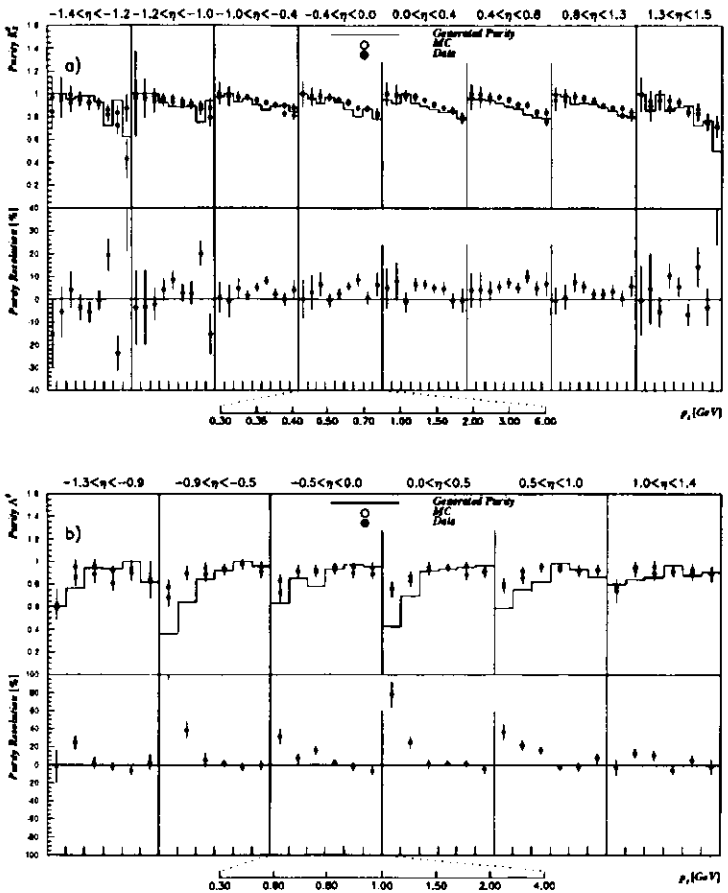

Figure 8.8: Purity of reconstructed *a)* K^0_S and *b)* Λ^0 signal inside bins of a grid in the p_t-η plane. The x-labels on top of the histogram give the η ranges of the bin. The points within such a range correspond to the p_t bins as defined in the expansion at the bottom of the histogram. The MC predictions for the purity of the signal as well as the calculated result are shown in the upper histograms. The purity as estimated from the data are shown as dark dots. The lower parts of the figures show the relative error with respect to the MC prediction.

tendency for an overestimation of the purity by $\lesssim 10\,\%$ is indicated for the K^0_S using method 2. The influence on the reconstructed multiplicities is included in the study of systematic errors (section 8.5). Also shown in the upper part of the figure is the purity as extracted from the data sample. This distribution is in good agreement with the MC prediction.

For the error calculation generally a Normal distribution was used as working hypothesis, even if in some bins a Poisson distribution would have been more accurate. However, the impact on the overall error on the purity is negligible.

8.2 *Effective Acceptance Correction*

The acceptance depends on the geometry of the tracking detector, therefore a dependence on the azimuthal angle ϕ, the pseudorapidity η and the transverse momentum p_t of the neutral strange particle might be expected in its reconstruction. Furthermore the event kinematics can influence the acceptance, *e.g.* higher momentum transfer can lead to higher particle multiplicities, implying that strange particles might be hidden in jets and therefore not be resolved.

As seen in figures 8.1, 8.2 and 8.3 no neutral strange particles are reconstructed and selected with $|\,\eta\,| > 2.0$. This coincides with the boundaries of the CTD. Therefore the additional selection criteria $|\,\eta\,| < 2.0$ will be applied in the following studies.

If ξ stands for the ϕ,η or p_t of the particle under study the effective acceptance is defined as :

$$eacc(\xi) = \frac{n_{rec.}(\xi)}{N_{event,rec.}} \Big/ \frac{n_{gen.}(\xi)}{N_{event,gen.}} \tag{8.4}$$

n_{gen} is the number of generated particles as a function of the generated ξ within the full sample of $N_{event,gen.}$ generated events. These $N_{event,gen.}$ events are generated within the selected x, y, Q^2 range and have passed the event selection cuts. Analogously n_{rec} is the number of reconstructed particles as a function of the reconstructed ξ within the full sample of $N_{event,rec.}$ reconstructed events. These $N_{event,rec.}$ events are reconstructed within the selected x, y, Q^2 range and pass the event selection cuts. If

ξ is a global event variable like Q^2 then formula 8.4 is modified to :

$$eacc(\xi) = \frac{n_{rec.}(\xi)}{N_{event,rec.}(\xi)} / \frac{n_{gen.}(\xi)}{N_{event,gen.}(\xi)} \tag{8.5}$$

n_{gen} and n_{rec} are as before but $N_{gen.}(\xi)$ and $N_{rec.}(\xi)$ are considered as functions of Q^2, too.

With this definition the effective acceptance can be interpreted as the ratio of the (true) reconstructed rate to the generated rate, both as functions of ξ. Furthermore it includes :

- statistical corrections (*i.e.* not on event by event basis) for event migration in or out of the chosen kinematical region in x, Q^2 and y (see section 6.5).
- statistical corrections (*i.e.* not on particle by particle basis) for migration effects in reconstructing p_t and η of the particle itself.

The influence of the DIS event selection cuts on the effective acceptance has been found to be negligible and is therefore not included in the determination of the correction grid but included in the systematic studies instead (section 8.5).

The effective acceptances for Λ and $\bar{\Lambda}$ are for all distributions in very good agreement within one MC model and within the statistics. Usually they differ by less than $1\,\sigma$, but the agreement is always better than $2\,\sigma$. Therefore no distinction is made in the effective acceptance correction for Λ and $\bar{\Lambda}$.

Figure 8.9 shows the effective acceptance as a function of the azimuthal angle ϕ for *a)* K^0_S and *b)* Λ^0. In both cases the effective acceptance is consistent with being completely flat over the full range, fluctuations within the distribution of one Monte Carlo model are not seen with the other and vice versa. This is expected for a CTD with cylindrical symmetry. Because of the constancy of the effective acceptance over the whole ϕ-range, a correction as a function of ϕ is not necessary. A fit with a constant (function) to the combined MC samples gives an effective acceptance of $(25.8 \pm 0.38)\%$ and $(8.31 \pm 0.36)\%$ for the K^0_S and Λ^0, the normalized χ^2's are 0.975 and 0.897, respectively. These fit results are consistent with the results obtained by fitting the individual MC distributions.

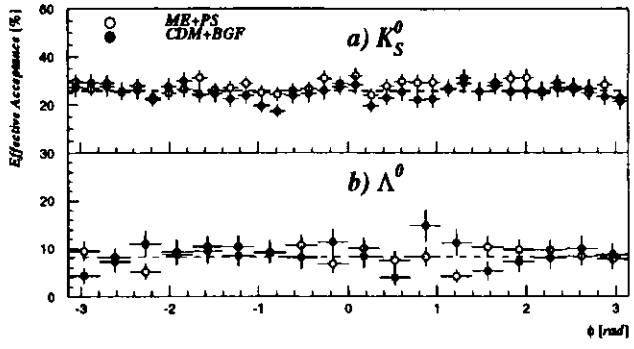

Figure 8.9: *Effective acceptance as a function of the azimuthal angle ϕ for a) K^0_S and b) Λ^0. The dashed line indicates the average value.*

Figure 8.10 shows the effective acceptance as a function of the pseudorapidity η, again for *a)* K^0_S and *b)* Λ^0. A clear drop-off of the effective acceptance towards the edges of the CTD can be seen. This is mainly due to the Foster cut (as introduced in section 7.1) that rejects tracks in the very forward or backward direction. Again, this behaviour is qualitatively reproduced by both MC models for the K^0_S and the Λ^0. Nevertheless the ME+PS MC suggests a slightly higher effective acceptance for K^0_S as compared to the CDM+BGF MC. A correction for the variation in the effective acceptance as function of η will be applied.

Figure 8.11 shows the effective acceptance as a function of the transverse momentum p_t, for *a)* K^0_S and *b)* Λ^0. For the K^0_S, the effective acceptance rises with increasing p_t from $\sim 10\,\%$ to a plateau value of $\sim 50\%$ at $p_t \sim 2\,GeV$. From thereon it stays statistically consistent with a flat distribution up to $\sim 8\,GeV$. For the Λ^0 the effective acceptance reaches a plateau of $\sim 15\%$ already at $\sim 1\,GeV$ and stays flat within the statistics up to $6\,GeV$. The production of high p_t particles is exponentially suppressed, therefore the statistical errors of the effective acceptances rise with increasing functions of p_t. Wider histogram bins have been chosen for $p_t > 5\,GeV$ to compensate

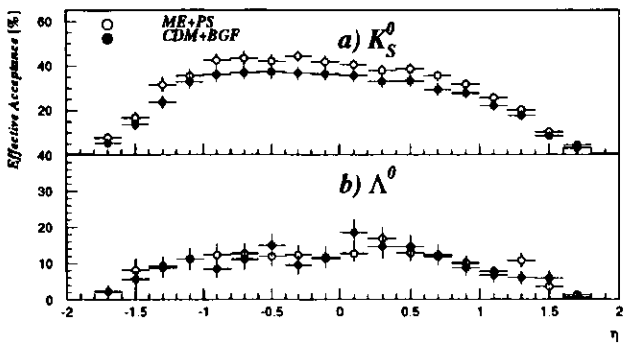

Figure 8.10: *Effective acceptance as a function of pseudorapidity η for a) K^0_S and b) Λ^0*

the lower statistics. Still, for the Λ^0 distribution no statistics are available for the highest p_t bin. No clear signals for K^0_S with $p_t > 6\,GeV$ and Λ^0 with $p_t > 4\,GeV$ have been found in the data sample, thus candidates with p_t above these limits are disregarded in this analysis. The general behaviour at low p_t is again dominated by the Foster cuts, rejecting low p_t tracks. The variation of the effective acceptance as a function of p_t is considered large enough to be corrected for.

A study of the effective acceptance as a function of the longitudinal momentum p_z has also been performed. However, p_z is strongly correlated to the polar angle θ and therefore to η. Therefore the correction for the η dependence will implicitly correct for the p_z dependence, too.

Figure 8.12 shows the effective acceptance as a function of the momentum transfer Q^2, for *a)* K^0_S and *b)* Λ^0. A slight dependence on Q^2 can be seen, however, the event sample is strongly dominated by events with low Q^2 (86 % of the events passing the event selection cut have Q^2 less than $60\,GeV$). Therefore no correction is applied.

In summary, only the variations of the effective acceptance as functions of p_t and η have been considered large enough to be corrected for. A two-dimensional effective acceptance correction, as introduced in the following section, will therefore be applied.

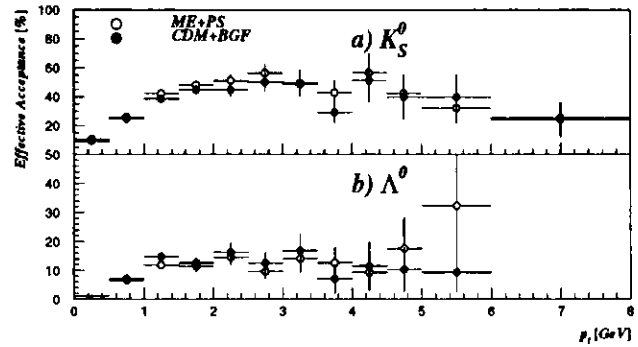

Figure 8.11: *Effective acceptance as a function of the transverse momentum p_t for a) K^0_S and b) Λ^0*

8.3 The Effective Acceptance Correction Grid

Figures 8.13 and 8.14 show the two-dimensional effective acceptance correction grids as functions of p_t and η for the K^0_S and Λ^0 respectively. The CDM+BGF MC sample (highest statistics) was used in order to determine the effective acceptance grid. A nonlinear binning has been chosen for p_t and for η. The choice of the binnings for the grids is a compromise between the following considerations :

- The ranges in p_t and η are chosen as $0.3\,GeV \le p_t \le 6\,GeV$, $-1.4 \le \eta \le 1.5$ for K^0_S and $0.3\,GeV \le p_t \le 4\,GeV$, $-1.3 \le \eta \le 1.4$ for Λ^0. Outside these ranges no clear signals for the particles are found in the data sample .

- The effective acceptance must not be zero in any bin of the chosen range in p_t and η (*i.e.* "blind" regions of the detector are excluded from the analysis).

- The binning has to reflect the variations in the effective acceptance. It has to be finest where the effective acceptance changes rapidly and can be coarse where there are only small variations.

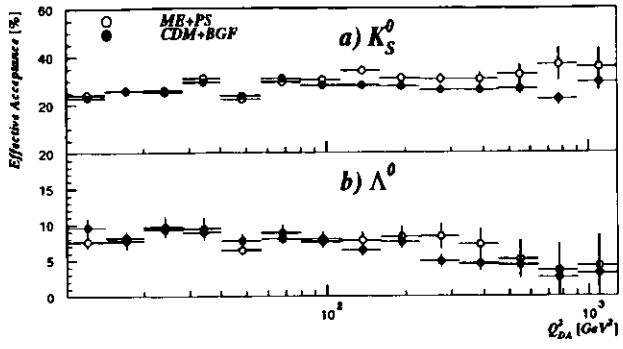

Figure 8.12: *Effective acceptance as a function of the momentum transfer momentum Q^2 for a) K^0_S and b) Λ^0*

- The granularity of the grid is limited by the statistics of the MC sample. Statistics must not be zero in any bin, when calculating the effective acceptance.

- The reconstruction resolution of p_t and η inside the bins has to be better than the bin size in order to minimize correction errors due to migration effects. Figure 8.15 shows the achieved reconstruction accuracy and resolution in η and p_t projections of the effective acceptance correction grid. In each bin the distribution $p_{t,rec} - p_{t,gen}$ (or $\eta_{rec} - \eta_{gen}$) has been fit to a Gaussian. The points correspond to the fitted peak center, the error rectangles are the error on the peak centre and the error bars are the peak widths. The use of projections rather than a fit in each bin is due to limited statistics in the individual bins. The fitted peak centers are consistent with no systematic shift in the reconstruction (except in the lowest p_t bin for the Λ^0. However, the shift is negligible compared to the bin size.) The (absolute) resolution within a given bin is always better than 10 % of the bin size.

- A clear signal in the mass distribution (data) has to be obtained in order to get a reliable number of reconstructed particles and the signal to background ratio

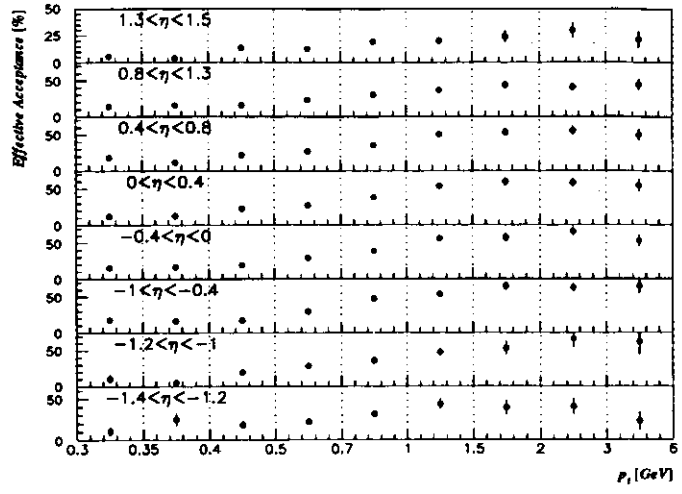

Figure 8.13: *K^0_S effective acceptance grid as a function of p_t and η.*

(see section 8.1).

Studies of fitting simple smooth functions onto this grid, such as polynomials of 3rd degree in η and functions of type $p(1) \cdot \log(p_t) + p(2)$ for the corresponding projections and a combination of these for a 2D fit, showed no improvement on the reconstruction resolution. They rather increased the systematic error on the effective acceptance correction. Therefore the latter is applied in bins as shown in figures 8.13 and 8.14.

8.4 The Correction Method

The results of studies in this thesis will be presented in form of multiplicity (or synonymous : "(production) rate") distributions, given as functions of a kinematic variable ξ (either p_t, η of the particle or Q^2_{DA}, W_{DA} of the event). The multiplicity hereby is defined as the average number of particles, either K^0 or Λ^0, produced per

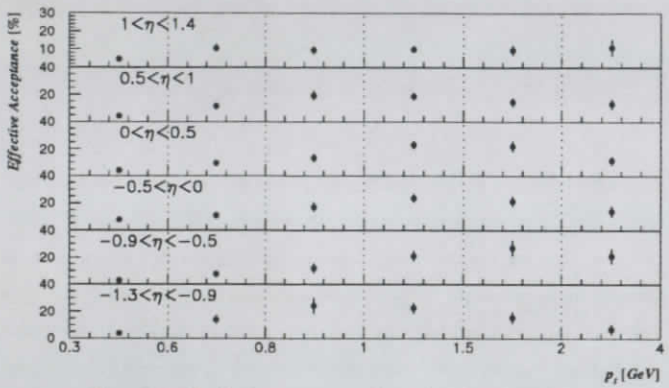

Figure 8.14: Λ^0 *effective acceptance grid as a function of* p_t *and* η.

event :

$$r(\xi) = \frac{1}{N_{event}} \frac{n_{part}}{\Delta\xi} \tag{8.6}$$

Each particle candidate contributes to the distribution in the corresponding ξ bin with a weight w. This weight is calculated as :

$$w = \frac{pur}{br \cdot eacc} \tag{8.7}$$

pur is the purity, the estimated probability (according to its p_t and η) for the candidate of being a true particle. It is extracted from the DIS data sample according to formula 8.2 in section 8.1. The choice to use the data rather than the higher statistics of the MC samples to determine the purity reduces the model dependence of the correction procedure. The distribution of *pur* as function of its p_t and η is shown as black circles in figure 8.8.

br stands for "branching ratio". This factor takes into account that we measure only one possible decay channel of the particle under study and therefore neglect all the particles that decay into a different channel. The decay $\Lambda \to p\pi^-$ ($\bar{\Lambda} \to \bar{p}\pi^+$) make up $(63.9 \pm 0.5)\,\%$ of all decays, therefore $br = 0.639$. The K^0 consists of $50\,\% K^0_S$ and $50\,\% K^0_L$. The K^0_S decays with $(68.61 \pm 0.28)\,\%$ into $\pi^+\pi^-$. Since we only measure this K^0_S decay channel, $br = 0.5 \cdot 0.6861$.

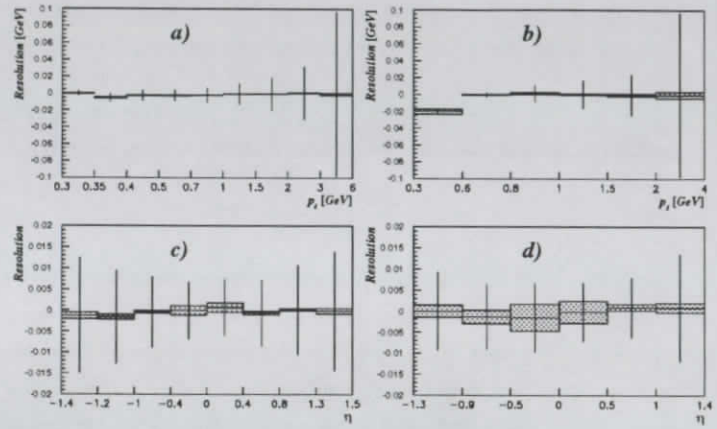

Figure 8.15: *Reconstruction accuracy (grey shaded rectangles) and resolution (error bars) as a function of* p_t *for a)*K^0_S *and b)*Λ^0*, and reconstruction and resolution as a function of* η *for c)*K^0_S *and d)*Λ^0*. The bin definitions are the same as on the corresponding axis of the effective acceptance correction grid.*

eacc is the estimated effective acceptance (according to its p_t and η) for the candidate. The distributions of *eacc* as function of its p_t and η are shown in figures 8.13 and 8.14.

The calculation of the errors in the distribution bins is solely based on the statistics of the contributing candidates, *i.e.* the statistical errors are given as the bin entries divided by the square root of the number of candidates within the bin. The influence of uncertainties in the determination of the *pur* and *eacc* are included in the calculation of the systematic errors (see section 8.5).

The purity distribution varies with p_t and η, as can be seen in figure 8.8. The effective acceptance correction factors *eacc* are based on the reconstruction of true

particles in a given (p_t,η) bin. However, in the data sample of candidates it is not possible to distinguish between true particles and background. Therefore the background will be corrected like a true particle. An effective acceptance correction for background does not make physical sense nor should it be expected to be the same as for the particles. In order not to be biased, the background has to be subtracted statistically in each bin (and therefore the number of candidates corrected to the number of true particles in this bin). Therefore it is obvious that *pur* and *eacc* have to be determined in the same grid of p_t and η bins.

8.5 Studies of Systematics

In order to understand the measured K^0 and Λ multiplicities $r(\xi)$ (*i.e.* as function of any kinematic variable $\xi = p_t$, η, Q^2_{DA},...) several sources of systematic effects have been studied :

1. The effect of the DIS event selection criteria on the production rates has been investigated using the DIS Monte Carlo samples. The production rates $r_{gen}(\xi)$ of a MC sample generated inside the selected kinematic range have been extracted and compared to the production rates $r_{rel}(\xi)$ for the subsample of events that pass the additional DIS event selection criteria. The systematic shift due to the DIS selection criteria, $\epsilon_{DIS}(\xi)$, is calculated as the average of the deviations of the MC predictions. The deviations are calculated as : $\epsilon_{MC}(\xi) = \frac{r_{MC,rel}(\xi) - r_{MC,gen}(\xi)}{r_{MC,gen}(\xi)}$, where MC denotes either ME+PS or CDM+BGF. The error on $\epsilon_{DIS}(\xi)$ is taken as half the difference of the two MC predictions.

$$\epsilon_{DIS}(\xi) = \frac{\epsilon_{CDM+BGF}(\xi) + \epsilon_{ME+PS}(\xi)}{2} \pm \left| \frac{\epsilon_{CDM+BGF}(\xi) - \epsilon_{ME+PS}(\xi)}{2} \right| \quad (8.8)$$

2. The effect of event migration on the particle production rate has been studied with the ME+PS and CDM+BGF MC samples. Both MC samples predict that $\sim$ 85% of events reconstructed within the selected kinematic range are also generated in this range. The number of events migrating in to the selected range is comparable to that of events migrating out, leading to a net gain/loss of events of +3 % for ME+PS and −3 % for CDM+BGF. The particle production rates for events migrating into the selected range is generally comparable on a 5 % level to that of events migrating out. Note that migration effects are implicitly corrected for in the effective acceptance grid. Therefore, the study of the accuracy of the reconstruction method includes the systematic shift and error due to migration effects.

3. In order to study the influence of photoproduction background, the particle production rates have been extracted from the data sample with different lower limits of $E-p_z$ ($30\,GeV$ in order to increase the contribution of photoproduction events, $40\,GeV$ to reduce the contribution). This variation also affects the amount of DIS events with hard initial state radiation (where the radiated photon escapes undetected) accepted in the final data sample. Although the latter are not background events, they will be reconstructed within the wrong kinematic regime (see section 5.1.4) and therefore contribute to event migration effects. Studies with the DIS MC sample (including initial state radiation) predict stable production rates (within 1 %) for $25\,GeV < E - p_z < 45\,GeV$, therefore a dependence of the production rates on the lower limit of $E - p_z$ for the data sample can be attributed to the contribution from photoproduction events. The resulting systematic shift, $\epsilon_{PhP}(\xi)$ is estimated as :

$$\epsilon_{PhP}(\xi) = \frac{r_{40\,GeV}(\xi) - r_{30\,GeV}(\xi)}{r(\xi)} \quad (8.9)$$

The errors in the rates $r_{30\,GeV}(\xi)$ and $r_{40\,GeV}(\xi)$ have been propagated to calculate the error in $\epsilon_{PhP}(\xi)$.

4. The accuracy of the correction method has been tested with all DIS MC samples. The particle production rates are reconstructed in treating the MC samples exactly like the data. The relative difference between the generated and

reconstructed distributions gives the individual systematic shifts :

$$\epsilon_{rec,MC}(\xi) = \frac{r_{MC,gen}(\xi) - r_{MC,rec}(\xi)}{r_{MC,gen}(\xi)} \tag{8.10}$$

For the calculation of the error $\delta\epsilon_{rec,MC}$ no error in the generated distributions is assumed. The overall systematic shift $\epsilon_{method}(\xi)$ is the average of the results for the different MC samples. The individual errors are added in quadrature.

$$\epsilon_{Method}(\xi) = \frac{\sum_{MC}\epsilon_{rec,MC}(\xi)}{n_{MC}(\xi)} \pm \frac{\sqrt{\sum_{MC}\delta\epsilon_{rec,MC}(\xi)^2}}{n_{MC}(\xi)} \tag{8.11}$$

5. The influence of the uncertainty in the determination of the purity and the effective acceptance correction grid on the particle production rates has been tested. The particle production rates $r(\xi)$ have been reconstructed from the data sample as before, but to calculate the error $\delta r(\xi)$ the errors δpur, as in figure 8.8 and the errors $\delta eacc$ as in figures 8.13 and 8.14 have been propagated into the error of the weight w of formula 8.7. The error on the branching ratios for the decays of the neutral strange particles is less than 1 % and therefore negligible. The errors in pur and $eacc$ are independent, therefore the formula for the error δw reads as :

$$\delta w = \frac{1}{br}\sqrt{(\frac{1}{eacc})^2\delta pur^2 + (\frac{pur}{eacc^2})^2\delta eacc^2} \tag{8.12}$$

The systematic error due to uncertainty in the purity is then given as :

$$\delta\epsilon_{Correction}(\xi) = \sqrt{\sum(\delta w^2)} \tag{8.13}$$

where the sum runs over the candidates in the corresponding ξ bin. There is no systematic shift due to this uncertainty in the purity.

6. The influence of particle reconstruction criteria (section 7.1) on the particle production rates has been investigated. The Foster cuts and the number of daughter tracks associated with the primary event vertex have been varied independently in order to estimate the stability of the result. The polar angle range allowed for the daughter tracks of candidates has been widened to $15° < \theta < 165°$ (*i.e.*

$|\eta| < 2.0$) and restricted to $25° < \theta < 155°$ (*i.e.* $|\eta| < 1.5$). The minimum transverse momentum allowed for the daughter tracks of candidates has been varied by $\pm 10\,\%$ (*i.e.* to $0.135\,GeV$ and $0.165\,GeV$). The number of daughter tracks of the candidates associated with the primary event vertex has been varied by ± 1 for K^0_S and $+1$ for Λ^0. However, the requirement of intersecting daughter tracks of opposite charge for candidates has not been changed.

For the K^0_S the variation in the Foster cuts affects mainly candidates with low p_t and/or in the very forward/backward regions where the weight w (formula 8.7) has large uncertainties. Neither the effective acceptance correction grid nor the corresponding purities are redetermined with the new cut value but are kept fixed. In case of the Λ^0 the effective acceptance and $Efficiency * Purity$ are more sensitive to changes in the Foster cuts, mainly on changes in the lower limit of p_t. Therefore, the effective acceptance correction grid and the corresponding purities are redetermined with the new cut values. The same applies for K^0_S and Λ^0 for the limit in the number of daughter tracks of the candidates allowed to be associated with the primary event vertex. Again, the purity of the candidate sample, the effective acceptance and $Efficiency*Purity$ change significantly over the whole p_t and η range with a change in this limit. Therefore, the effective acceptance correction grids as well as the purities are redetermined with the changed number of daughter tracks associated with the event vertex. Such a discreet change is only a "worst case" approximation for resolution effects of the tracking devices. However, a more detailed study based on the χ^2 of the vertex fit is beyond the scope of this analysis.

The rates $r_{rec}(\xi)$ are reconstructed using the new cut value and the corresponding correction.

The systematic shifts are calculated for each varied reconstruction criterion as deviations from the nominal rates :

$$\epsilon_{rec}(\xi) = \frac{r_{rec}(\xi) - r(\xi)}{r(\xi)} \tag{8.14}$$

For the error calculation on $\epsilon_{rec}(\xi)$ no error in $r(\xi)$ is assumed. The overall systematic shift $\epsilon_{Reconstruction}(\xi)$ is the average of the six individual $\epsilon_{rec}(\xi)$.

$$\epsilon_{Reconstruction}(\xi) = \frac{\sum_{rec} \epsilon_{rec}(\xi)}{6} \pm \frac{\sqrt{\sum_{rec} \delta\epsilon_{rec}(\xi)^2}}{6} \tag{8.15}$$

7. The particle selection criteria Δz, α, α_{xy} and $c\tau$ for the candidates, as introduced in sections 7.2 and 7.3, have been varied independently by $\pm 25\,\%$ in the data sample in order to estimate the stability of the result. Note that neither the effective acceptance correction grid nor the corresponding purities are redetermined with the new cut value but are kept fixed. The studies with the DIS MC samples in section 7.1 predict for such variations only a small effect on $Efficiency*Purity$, which is equivalent (except for the overall correction factor for the decay branching ratios) to the correction factors of formula 8.7 applied to the candidates. In fact, the nominal cut values were chosen such to avoid strong dependencies. The influence of the "anti-Λ^{0}" cut (on K^0 rates) and the "anti-K^0_S" cut (on the Λ^0 rates) has been investigated. The anti-Λ^0 cut rejects all candidates which have an invariant mass $m(p\pi)$ less than $\sim m(\Lambda) - 2\,\sigma(\Lambda)$, where $m(\Lambda)$ and $\sigma(\Lambda)$ are the fitted mass and signal width as extracted from the final DIS candidate sample (figure 7.15). This corresponds to a rejection of $\sim 93\,\%$ of the Λ^0 signal contaminating the K^0_S signal. This cut has been varied to $\sim m(\Lambda) - 1.5\,\sigma(\Lambda)$ and $\sim m(\Lambda) - 3\,\sigma(\Lambda)$ (corresponding to a rejection of $\sim 89\,\%$ and $\sim 97.5\,\%$ of the Λ signal. Similarly the anti-K^0_S cut of $\sim m(K^0_S) - 2.5\,\sigma(K^0_S)$ (rejecting $\sim 96\,\%$ of the K^0_S contaminating signal) has been varied to $\sim m(K^0_S) - 2\,\sigma(K^0_S)$ and $\sim m(K^0_S) - 3.5\,\sigma(K^0_S)$ (rejecting $\sim 93\,\%$ and $\sim 98.5\,\%$ respectively). The criterion on the photon conversion background has been varied by $\pm 10\,\%$.

The systematic shifts are calculated for each varied selection criterion as deviations from the nominal rates :

$$\epsilon_{sel}(\xi) = \frac{r_{sel}(\xi) - r(\xi)}{r(\xi)} \tag{8.16}$$

For the error calculation on $\epsilon_{sel}(\xi)$ no error in $r(\xi)$ is assumed. The overall systematic shift $\epsilon_{Selection}(\xi)$ is the average of the twelve individual $\epsilon_{sel}(\xi)$.

$$\epsilon_{Selection}(\xi) = \frac{\sum_{sel} \epsilon_{sel}(\xi)}{12} \pm \frac{\sqrt{\sum_{sel} \delta\epsilon_{sel}(\xi)^2}}{12} \tag{8.17}$$

The overall systematic shift, ϵ_{Syst}, is calculated as the sum of the systematic shifts above, the errors are added in quadrature.

$$\begin{aligned} \epsilon_{Syst}(\xi) &= \epsilon_{DIS}(\xi) + \epsilon_{PAP}(\xi) \\ &\quad + \epsilon_{Method}(\xi) + \epsilon_{Reconstruction}(\xi) + \epsilon_{Selection}(\xi) \end{aligned} \tag{8.18}$$

$$\begin{aligned} \delta\epsilon_{Syst}(\xi) &= \delta\epsilon_{DIS}(\xi) \oplus \delta\epsilon_{PAP}(\xi) \\ &\quad \oplus \delta\epsilon_{Method}(\xi) \oplus \delta\epsilon_{Correction}(\xi) \\ &\quad \oplus \delta\epsilon_{Reconstruction}(\xi) \oplus \delta\epsilon_{Selection}(\xi) \end{aligned} \tag{8.19}$$

The overall absolute systematic shift is obtained as $\delta r_{Syst}(\xi) = \epsilon_{Syst}(\xi) \cdot r(\xi) \pm \delta\epsilon_{Syst}(\xi) \cdot r(\xi)$. These studies are repeated for each measured production rate distribution.

9

Properties of Neutral Strange Particles

This section studies various aspects of neutral strange particle production in DIS events. All studies are performed in the ZEUS laboratory frame and restricted to a kinematic range where the tracking acceptance is high and well understood. As has been shown in section 8 the Monte Carlo models predict a geometric acceptance of only $\sim 30\,\%$ for K^0_S, $\sim 20\,\%$ for Λ and $\sim 25\,\%$ for $\bar{\Lambda}$ in η. Outside this region, especially in the proton fragmentation region, there are no means to test this prediction since there the ZEUS detector is "blind". The same applies for the low p_t ($< 300\,MeV$) region where the tracking fails or is not understood yet. An extrapolation to the full p_t and η region would therefore include large uncertainties and be strongly model dependent. All distributions are given in the form of differential multiplicities rather than in differential cross-sections. This is in order to avoid systematic errors due to uncertainties in the determination of the integrated luminosity of the selected data sample and the uncertainty in the calculated DIS cross-section of the MC samples.

In section 9.1 the differential multiplicities as functions of η and p_t are studied. A comparison with MC models, which are based on knowledge gained from e^+e^- collider experiments, allows a test of the universality of the hadronization process as observed in both of the two different event classes. Of special interest is the suppression of heavy quarks relative to light quarks in the fragmentation process. Also included is a comparison between the results extracted from the 1993 e^-p and the 1994 e^+p run period.

In section 9.2 the particle and energy flow of neutral strange particles with respect to the current jet axis is studied. A comparison with the two DIS MCs allows a test

of the underlying parton shower models.

The hadronic final state of the DIS process, and therefore the production of neutral strange particles, depends on the event kinematics. These dependencies, as functions of Q^2 and W, are studied in section 9.3.

Section 9.4 focuses on the differences between K^0 production in events with and without rapidity gaps in order to look for possible differences in particle production in diffractive and non-diffractive events. Here again the distributions as functions of η, p_t and the particle flow are compared between the two event types. Also included is a comparison with diffractive MC models which incorporate different assumptions about the nature of the scattering mechanism.

9.1 *Differential Multiplicities as a Function of η and p_t*

9.1.1 *The ZEUS 1994 e^+p Analysis*

Figures 9.1 *a*) - *c*) show the differential K^0 and Λ^0 multiplicity as functions of their pseudorapidity η and transverse momentum p_t. The multiplicities are normalized to the number of ZEUS 1994 e^+p DIS events (N_{events}) with $10\,GeV^2 < Q^2 < 1280\,GeV^2$, $0.0003 < x < 0.1$ and $y > 0.04$. The choice to plot the differential multiplicities as $1/N_{events}\Delta n/\Delta\eta$ and $1/N_{events}\Delta n/\Delta p_t^2$ is motivated from the fact that $dY\,dp_t^2 \sim d\eta dp_t^2$ is proportional to the available phase space. The kinematic range for the K^0 is restricted to $-1.4 < \eta < 1.5$ and $0.3\,GeV < p_t < 6\,GeV$, the kinematic range for the Λ^0 is restricted to $-1.3 < \eta < 1.4$ and $0.3\,GeV < p_t < 4.0\,GeV$. In these ranges a reasonable detector acceptance and reconstruction efficiency is obtained. The black circles and squares are the measured distributions for the K^0 and Λ^0, fully corrected for all detector effects. The horizontal error bars span the bin size, the thick vertical error bars show the statistical errors and the outer error bars correspond to the statistical and systematic errors added in quadrature. The measured average number of K^0 per event, produced in the selected kinematic range is $0.406 \pm 0.005^{+0.001}_{-0.016}$. For the Λ^0 an average number of $0.053 \pm 0.002^{+0.003}_{-0.003}$ is obtained. The first error is the statistical error obtained from the number of reconstructed K^0_S and Λ^0, respectively.

For the systematic error an upper and lower value is given in order to emphasize a possible systematic shift intrinsic to the analysis.

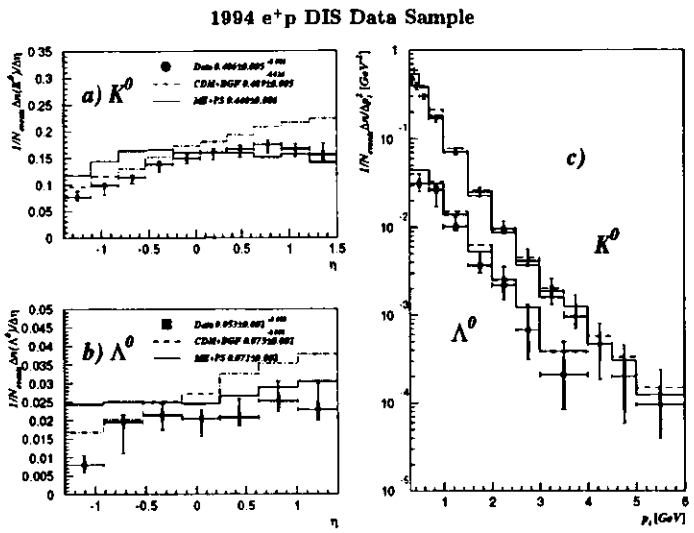

Figure 9.1: *Differential multiplicity as a function of a) the pseudorapidity η of the K^0, b) the pseudorapidity η of the Λ^0 and c) the transverse momentum p_t of the K^0 and Λ^0. The kinematic range for the K^0 is restricted to $-1.4 < \eta < 1.5$ and $0.3\,GeV < p_t < 6.0\,GeV$. The kinematic range for the Λ^0 is restricted to $-1.3 < \eta < 1.4$ and $0.3\,GeV < p_t < 4.0\,GeV$. The distributions are normalized to the number of ZEUS 1994 e^+p events (N_{events}) with $10\,GeV^2 < Q^2 < 1280\,GeV^2$, $0.0003 < x < 0.1$ and $y > 0.04$. The circles and squares are the measured distributions for the K^0 and Λ^0, respectively. The horizontal error bars give the bin size, the thick vertical error bars show the statistical errors and the outer error bars correspond to the statistical and systematic errors added in quadrature. The solid and the dashed lines show the predictions of the ME+PS and CDM+BGF MC models, respectively. The MC samples are generated with a strange quark suppression factor $P_s/P_u = 0.3$. The numbers in the legend correspond to the integrated multiplicity.*

For the η distribution of the K^0, the statistical errors vary between ~ 3 and $7\,\%$ for the individual bins. The systematic shift is consistent with being zero, *i.e.* ϵ_{Syst} is usually $< 5\,\%$ with $\delta\epsilon_{Syst} \lesssim 10\,\%$. The contributions of all the individual systematic shifts are generally smaller than $\pm 5\,\%$, except for the two lowest and the highest η bins. There the systematic shifts determined from the correction method ϵ_{Method} and the photoproduction background ϵ_{PhP} go up to $\sim 10\,\%$. For the p_t distribution of the

K^0, the statistical error is $\lesssim 5\,\%$ for $p_t < 2\,GeV$ increasing to $\sim 40\,\%$ in the highest p_t bin. The systematic shift is below $(5 \pm 10)\,\%$ for $p_t \leq 2.5\,GeV$, as are all the individual contributions. With increasing p_t, the dominating individual systematic shift arises from the correction method ϵ_{Method}. $\delta\epsilon_{PhP}$ and $\delta\epsilon_{Method}$, which increase strongly due to the limited statistics in the high p_t bins, dominate $\delta\epsilon_{Syst}$.

For the Λ^0 distributions the statistical error in the η bins is $\sim 10\,\%$, for the p_t bins the statistical error increases from $\sim 7\,\%$ to $\sim 30\,\%$ with increasing p_t. As for the K^0, the systematic shift for the η distribution of the Λ^0 is consistent with zero : ϵ_{Syst} is usually $\sim 10\,\%$ with $\delta\epsilon_{Syst} \sim 20\%$. For the p_t distribution the systematic shift ϵ_{Syst} is smallest in the lowest p_t bin ($\sim 6\,\%$) and rises with increasing p_t. The dominating source over the whole η and p_t range is ϵ_{Method} due to the limited statistics available for the Λ^0 data as well as MC.

Also shown in figures 9.1 *a*) - *c*) are the predictions of the official ZEUS 1994 DIS e^+p MC samples. All contributing events are generated in the same kinematic region as the selected data sample and only neutral strange particles generated within the same p_t and η range as above are included in these distributions. The parameters for the CDM+BGF and ME+PS models are tuned to provide a good description of the hadronic final state distributions of non-diffractive DIS events, as measured with the ZEUS detector ([Der93a, Der94a, Der96a]). However, all predictions for the neutral strange particle production show significant differences (up to $\sim 12\sigma_{stat.}$) in shape and absolute rate compared to the measured production rates of neutral strange particles. The predicted multiplicities are 0.489 ± 0.005 and 0.440 ± 0.006 K^0 per event for CDM+BGF and ME+PS, respectively (data : $0.406 \pm 0.005^{+0.001}_{-0.016}$). The predicted Λ^0 rates are 0.075 ± 0.001 (CDM+BGF) and 0.071 ± 0.002 (ME+PS) per event (data : $0.053 \pm 0.002^{+0.003}_{-0.003}$). The quoted errors are the statistical errors based on the limited number of generated neutral strange particles[1]. The CDM+BGF model suggests a much stronger forward - backward asymmetry for the production of neutral strange particles than the ME+PS model. In the backward region, η

[1]The selected MC samples have equivalent statistics to the selected data sample.

$\lesssim -0.2$ (*i.e.* $\theta \gtrsim 100°$) the data prefer the CDM+BGF prediction, although it is systematically higher. However, in the forward direction the data do not follow the rise of the CDM+BGF prediction but prefer the flatter ME+PS distribution. The biggest differences between data and MC for the p_t distributions are at low p_t. For the K^0 the MC predictions are significantly higher for $p_t \lesssim 1\,GeV$ ($\sim 7-9\sigma_{stat.}$), where the CDM+BGF model predicts higher rates than the ME+PS model. For $p_t \gtrsim 1.5\,GeV$ both MC models reproduce the measured distribution within the statistical errors. The p_t spectra can be described by a function of the form $\frac{c_1}{p_t}e^{c_2 p_t}$, where c_1 and c_2 are parameters determined with a fit. The slope c_2 can be interpreted as the hardness of the distribution. A fit to the data distribution gives a value of $(-1.30 \pm 0.02)\,GeV^{-1}$. This is in good agreement with the result of a fit to the MC distributions : $(-1.31 \pm 0.01)\,GeV^{-1}$ and $(-1.31 \pm 0.02)\,GeV^{-1}$ for CDM+BGF and ME+PS, respectively. In the case of the Λ^0 the differences between the MC models are not as significant as in the case of the K^0 ($\sim 4-5\,\sigma_{stat.}$), however the measured distribution is systematically lower. For the slopes, determined from fits to the p_t distributions, one finds $(-0.85 \pm 0.05)\,GeV^{-1}$ for the data, in agreement with $(-0.91 \pm 0.02)\,GeV^{-1}$ and $(-0.91 \pm 0.03)\,GeV^{-1}$ for CDM+BGF and ME+PS, respectively.

Figures 9.2 *a*) and *b*) show the the differential multiplicities for the Λ and $\bar{\Lambda}$ separately as function of their pseudorapidity η. The two measured distributions are in agreement within the statistical errors except for the second lowest η bin, where the Λ rate is $\sim 3.6\,\sigma$ higher. However, systematic studies of the Λ rate in this region suggest that the systematic shift is an artifact of the reconstruction method. Therefore, no evidence for a difference in the production mechanism for Λ and $\bar{\Lambda}$ is found. This is in agreement with the assumption that the "pick-up" production of Λ (see section 8) is not observed and only Λ^0 that are produced in the parton fragmentation process are detected. For the ME+PS model the predictions for the Λ and $\bar{\Lambda}$ rates are again in good agreement. The CDM+BGF model predicts a slight excess of $\sim 5\,\%$ ($\sim 2\,\sigma$) more Λ than $\bar{\Lambda}$, mainly in the forward region $\eta > 0$.

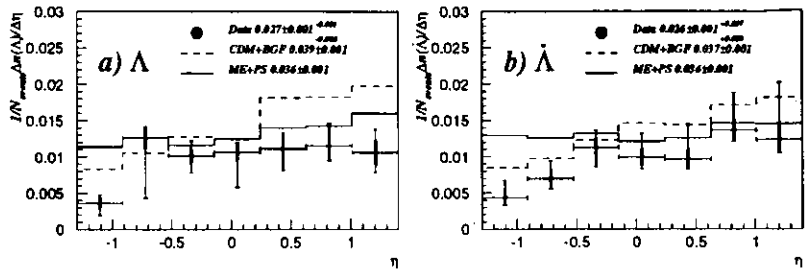

Figure 9.2: *Differential multiplicity as function of the pseudorapidity η for a) Λ and b) $\bar{\Lambda}$. The kinematic range for the Λ and $\bar{\Lambda}$ is restricted to $-1.3 < \eta < 1.4$ and $0.3\,GeV < p_t < 4.0\,GeV$. The distributions are normalized to the number of ZEUS 1994 e^+p events (N_{events}) with $10\,GeV^2 < Q^2 < 1280\,GeV^2$, $0.0003 < x < 0.1$ and $y > 0.04$. The circles are the measured distributions for the Λ and $\bar{\Lambda}$, respectively. The solid and the dashed lines show the predictions of the ME+PS and CDM+BGF MC models, respectively. The MC samples are generated with a strange quark suppression factor $P_s/P_u = 0.3$. The numbers in the legend correspond to the integrated multiplicity.*

Comparing the measured Λ or $\bar{\Lambda}$ distribution separately with the two MC shows the same behaviour within statistics as for the inclusive Λ^0 case.

9.1.2 *Review of the ZEUS 1993 e^-p Analysis*

A similar analysis has been done on the ZEUS 1993 e^-p data, the results of which are published in [Der95c]. Due to the statistics of the 1993 run period, which is roughly 5 times smaller than for the 1994 e^+p run period, the analysis was restricted to a smaller kinematic range $10\,GeV^2 < Q^2 < 640\,GeV^2$, $0.0003 < x < 0.01$ and $y > 0.04$. Among the selected events a total of ~ 1000 K^0_S and ~ 100 Λ^0 were reconstructed. These neutral strange particles were found within a kinematic range $|\,\eta\,| < 1.3$ and $0.5\,GeV < p_t < 4.0\,GeV$. With the higher statistics of the 1994 run period and the improved understanding of the tracking detector it was possible to improve the correction technique (for details on the correction technique for the 1993 analysis see ZEUS note [Geo94]). Applying now the new correction technique to the 1993 DIS[1]

[1]The effective acceptance is determined from the 1993 e^-p DIS MC samples, the purity is determined from the 1993 DIS data sample, both in the restricted kinematic range. Due to the limited statistics of the data, sample grids with fewer bins had to be chosen, therefore leading to higher systematic uncertainties.

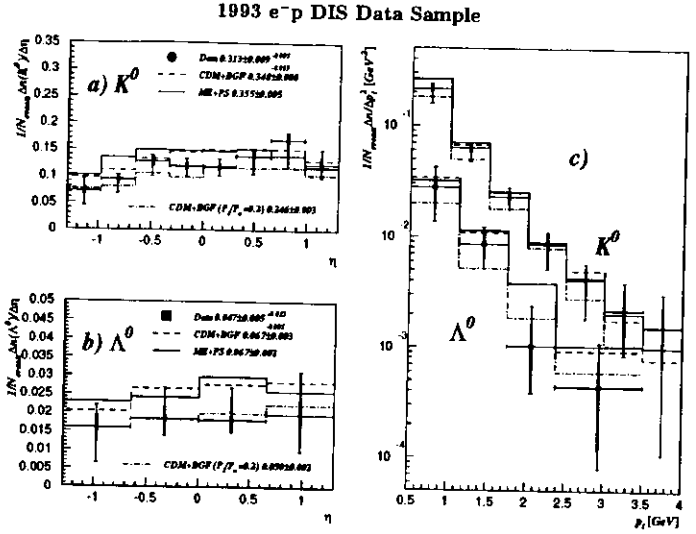

Figure 9.3: *Differential multiplicity as function of a) the pseudorapidity η of the K^0, b) the pseudorapidity η of the Λ^0 and c) the transverse momentum p_t of the K^0 and Λ^0 in bins of p_t. The kinematic range for the K^0 is restricted to $|\eta| < 1.3$ and $0.5\,GeV < p_t < 4.0\,GeV$. The kinematic range for the Λ^0 is restricted to $|\eta| < 1.3$ and $0.5\,GeV < p_t < 3.5\,GeV$. The distributions are normalized to the number of ZEUS 1993 e^-p events (N_{events}) with $10\,GeV^2 < Q^2 < 640\,GeV^2$, $0.0003 < x < 0.01$ and $y > 0.04$. The circles and squares are the measured distributions for the K^0 and Λ^0, respectively. The solid and the dashed lines show the predictions of the standard ME+PS and CDM+BGF MC models, respectively, generated with a strange quark suppression factor $P_s/P_u = 0.3$. The dash dotted lines show the predictions for the CDM+BGF model with a lowered strange quark suppression factor $P_u/P_s = 0.2$. The numbers in the legend correspond to the integrated multiplicity.*

data sample leads to results shown in figures 9.3 *a)* – *c)*.

The K^0 distributions are retained bin by bin within one σ of the statistical error. In the central region $\sim 10\,\%$ higher production rates are obtained, giving rise to an overall increase of $\sim 8\,\%$ with respect to the published result ($0.313 \pm 0.009^{-0.005}_{-0.039}$ instead of $0.289 \pm 0.015 \pm 0.014\,K^0$ per event). The systematic shifts are usually $\epsilon_{Syst} \lesssim 10\,\%$ with $\delta\epsilon_{Syst} \sim 10\,\%$, except for the second highest η bin, where ϵ_{Method} suggests an overestimation of $\sim 12\,\%$. For the p_t distribution the systematic shift is $\lesssim 10\,\%$ for the whole range, $\delta\epsilon_{Syst}$ increases with increasing p_t from $\sim 15\,\%$ to $\sim 60\,\%$, due to the decreasing statistics.

In case of the Λ^0 a general rise in all the bins is seen with respect to the published distribution ($0.047 \pm 0.005^{+0.012}_{-0.005}$ instead of $0.038 \pm 0.006 \pm 0.002\,\Lambda^0$ per event). Again the shift is of the order of one σ in each bin. The systematic shifts are between ~ -8 and $20\,\%$, dominated from $\epsilon_{Reconstruction}$. When applying stricter cuts, the determination of the correction factors is not reliable anymore given the limited statistics available in the 1993 samples. Therefore, the systematic errors should be regarded with care.

In the kinematic range chosen for the 1993 analysis, significant differences between the measured production rates for the neutral strange particles and the corresponding predictions of the standard 1993 e^-p DIS MC samples, overlaid as solid and dashed lines, are observed. However, the shapes of the measured distributions are reproduced reasonably well by both models. Also shown is the prediction of a second CDM+BGF MC sample with a modified strange quark suppression factor $P_s/P_u = 0.2$ instead of the standard value $P_s/P_u = 0.3$ (see section 5.1.3). The predicted rates are $0.246 \pm 0.003\,K^0$ and $0.050 \pm 0.002\,\Lambda^0$ per event. The measured K^0 distributions are usually between these two predictions, indicating a limit for the strange quark suppression factor of $0.2 < P_s/P_u < 0.3$. The measured Λ^0 production favours the lower value $P_s/P_u = 0.2$, but the modeling of baryon production includes additional parameters such as P_{qq}/P_q and P_{qs}/P_{qu} (see also 5.1.3) which allow adjustments to the measurements. The new revised results are in agreement with those published in [Der95c]. Detailed studies of the ratios of pions, kaons, strange baryons and protons are necessary for a determination of these parameters. This is beyond the scope of this thesis.

9.1.3 *Comparison of Results*

As for the 1994 analysis, the 1993 e^-p DIS MC samples were generated according to the ME+PS and the CDM+BGF model. Both models were subject to "fine tuning" of parameters for the 1994 run period, based on physics results from the 1993 run period. In order to compare the distributions of the 1993 analysis directly with the 1994 results and to disentangle the influence of this "fine tuning" and the physics

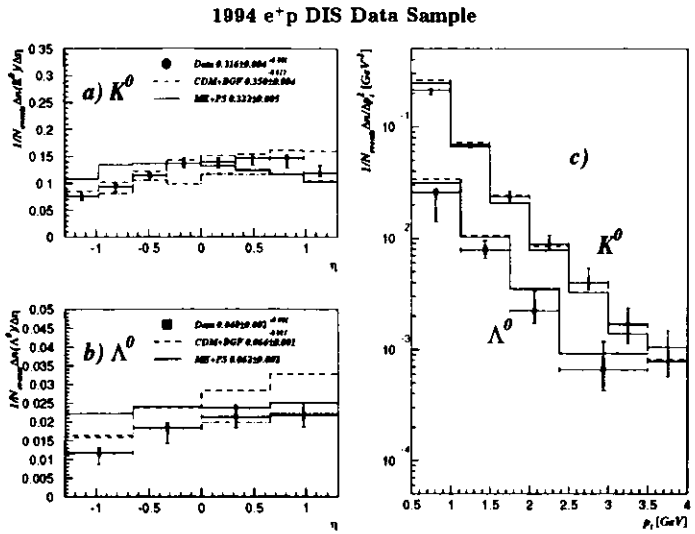

Figure 9.4: *Differential multiplicity as function of a) the pseudorapidity η of the K^0, b) the pseudorapidity η of the Λ^0 and c) the transverse momentum p_t of the K^0 and Λ^0 in bins of p_t. The kinematic range for the K^0 is restricted to $|\eta| < 1.3$ and $0.5\,GeV < p_t < 4.0\,GeV$. The kinematic range for the Λ^0 is restricted to $|\eta| < 1.3$ and $0.5\,GeV < p_t < 3.5\,GeV$. The distributions are normalized to the number of ZEUS 1994 e^+p events (N_{events}) with $10\,GeV^2 < Q^2 < 640\,GeV^2$, $0.0003 < x < 0.01$ and $y > 0.04$. The circles and squares are the measured distributions for the K^0 and Λ^0, respectively. The solid and the dashed lines show the predictions of the ME+PS and CDM+BGF MC models, respectively. The MC samples are generated with a strange quark suppression factor $P_s/P_u = 0.3$. The dash dotted lines in a) and b) show the predictions for the 1993 e^-p CDM+BGF model with a lowered strange quark suppression factor $P_u/P_s = 0.2$. The numbers in the legend correspond to the integrated multiplicity.*

of a widened kinematic region, the analysis was repeated with the ZEUS 1994 e^+p DIS sample, restricted to the same kinematic range as in the 1993 analysis. The kinematic range of the K^0 (Λ^0) is also restricted to $|\eta| < 1.3$ ($|\eta| < 1.3$) and $0.5\,GeV < p_t < 4.0\,GeV$ ($0.5\,GeV < p_t < 3.5\,GeV$), according to the range of the 1993 analysis. Figures 9.4 *a*) – *c*) show the the differential K^0 and Λ^0 multiplicity as functions of their pseudorapidity η and transverse momentum p_t. The same binning as in the 1993 analysis distributions was chosen. The multiplicities are normalized to the number of ZEUS 1994 e^+p DIS events in the restricted kinematic range. The

black circles and squares are the measured distributions for the K^0 and Λ^0, fully corrected for all detector effects[1]. The measured average number of K^0 per event, produced in the selected kinematic range is $0.316 \pm 0.004^{+0.001}_{-0.012}$. For the Λ^0 an average number of $0.048 \pm 0.002^{+0.001}_{-0.005}$ is obtained. Again, the first error is the statistical error obtained from the number of reconstructed K^0_S and Λ^0, respectively. The systematic shift is given as an upper and lower limit. For the η distribution of the K^0 the systematic shift ϵ_{Syst} is $\lesssim 5\,\%$, with $\delta\epsilon_{Syst} < 8\,\%$. The contributions of all the individual systematic shifts are in all bins smaller than $\pm 5\,\%$. For the p_t distribution of the K^0 the systematic shift is below $5\,\%$ for $p_t \leq 2.5\,GeV$, as are all the individual contributions. With increasing p_t the dominating individual systematic shift arises from the correction method ϵ_{Method}. $\delta\epsilon_{Php}$ and $\delta\epsilon_{Method}$ dominate $\delta\epsilon_{Syst}$ as p_t increases, due to the limited statistics in the high p_t bins. For the η distribution of the Λ^0 the systematic shift ϵ_{Syst} is in all bins better than $10\,\%$ with $\delta\epsilon_{Syst} \lesssim 15\,\%$. For the p_t distribution the systematic shift ϵ_{Syst} is completely dominated from ϵ_{Method} (the purity determination), suggesting systematic shifts up to $\pm 30\,\%$.

The corresponding MC predictions of the CDM+BGF and ME+PS model are overlaid. The same general behaviour as in figure 9.1 *a*) – *c*) is retained. However, for the K^0 the agreement between data and CDM+BGF extends now further into the forward region, giving an overall reasonable description of the shape. The ME+PS model still cannot reproduce the measured distribution. Both MC models overestimate the number of produced Λ^0 significantly.

Comparing the results of the above analyses in more detail leads to the following conclusions :

- The measured production rates of the neutral strange particles for the 1993 e^-p and 1994 e^+p DIS samples are in good agreement. For easier comparison the reconstructed rates for both run periods are overlaid in figures 9.5 *a*) – *d*). The agreement is usually better than one σ and, except for one point in the η

[1] The effective acceptance is determined from the 1994 e^+p DIS MC samples, the purity is determined from the 1994 e^+p DIS data sample, both in the restricted kinematic range of the 1993 analysis.

distribution of the K^0, better than two σ (for this point the difference is $2.3\,\sigma$). This is as expected from statistics. The σ are statistical errors of the 1993 measurement. Including the systematic errors the agreement is mostly better than one σ and always better than $1.5\,\sigma$. The consistency is expected since the $\gamma^* p$ process is independent of whether the photon is emitted from an electron or positron. The slightly higher positron beam energy ($27.5\,GeV$ e^+ in 1994, $26.7\,GeV$ e^- in 1993) is not significant (the change in the measured hadronic centre of mass energy is only of the order $\sim 3\,\%$).

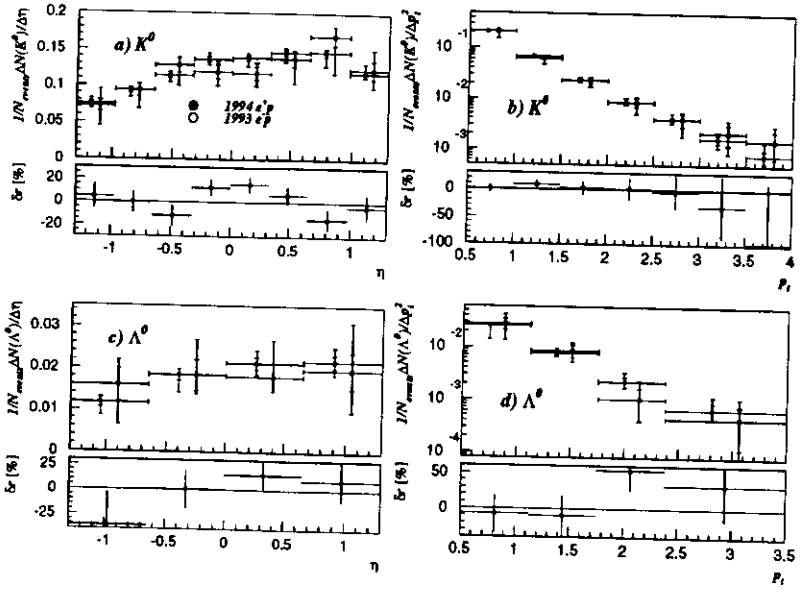

Figure 9.5: *Comparison of the differential multiplicities of neutral strange particles in ZEUS 1993 $e^- p$ (open circles) and 1994 $e^+ p$ (solid circles) DIS data samples. a), b) show the distribution for the pseudorapidity η and transverse momentum p_t of the K^0, c) and d) the corresponding distributions for the Λ^0. The upper parts of the figures show the measured distributions for the two data sets, with the data points shifted horizontally off the bin centre in order to allow an easy comparison. The lower part of the histograms show the relative change in the rates $\delta r = (r_{94} - r_{93})/r_{94}$ in %.*

- Comparing now the measured production rates 1994 $e^+ p$ in the 1993 analysis

range with the 1993 MC predictions confirms again the limit for the strange quark suppression factor $0.2 < P_s/P_u < 0.3$.

- Table 9.1 gives a review of P_s/P_u values obtained from different experiments at various centre of mass energies. Figure 9.6 is a graphical presentation of these values. The values vary between 0.13 and 0.55 with an average of $P_s/P_u \sim 0.29$. However, the situation for a direct comparison of the results is unclear, since not all data points are obtained from measurements, and/or include all parameters that affect strange particle production (*e.g.* an extra suppression factor for strange diquark production, proportion of pseudoscalar and vector resonances, etc.). Furthermore, studies show indications for a possible dependence of P_s/P_u on energy and/or the region of phase space. In that context the average numbers quoted in the figure for the different interaction types have to be taken with care. A more detailed discussion of these topics, including a description of the methods used to extract P_s/P_u, is given in [Wró90].

- Figures 9.7 *a*) – *d*) show the ratios of the predictions for the 1993 $e^- p$ and 1994 $e^+ p$ DIS MC samples. For the CDM+BGF model, no significant change in the p_t distribution for either K^0 or Λ^0 are seen. However, the η spectra show a trend to produce more neutral strange particles in the forward region and less in the rear. The main differences between the implementations of the CDM+BGF model in versions 4.03 and 4.06 of ARIADNE are a different treatment of the BGF process in order to improve the agreement with the measured three-jet rates, and the inclusion of a pomeron-like part in the proton structure function, in order to reproduce the topology of large rapidity gap events. Details of the new implementation can be found in [Lön94]. For the ME+PS model a depletion in the forward η region and over almost the whole p_t range, is observed for the K^0. The Λ distributions show the same tendency with reduced statistics. For the 1994 MC a change in the parameter y_{min} from the default $y_{min} > 0.0025$ to $y_{min} > 0.005$ was introduced. This parameter, *PARL*(8) in the LEPTO jargon, regulates the cutoff for the low-angle soft

emission in the matrix element calculation, avoiding singular regions. This is done in requiring a minimum invariant mass $m_{ij} > y_{min} W^2$ for each parton in the final state. Further details can be found in [Ing91]. The changes in the MC are based on physics results of the previous 1993 run period, changes in the detector description are not relevant for this analysis.

The measured multiplicities are summarized in tables 9.2 and 9.3.

Preliminary results of an independent study of strange particle production in DIS for the ZEUS 1994 e^+p run period have been published (see [Geo95]). The kinematic constraints on event selection and particle selection follow the 1993 ZEUS analysis. The resulting p_t and η distributions confirm the results of this analysis.

In a recent study the competing H1 experiment at the HERA collider presented a measurement of the differential multiplicity as function of η ([Aid96]). The data sample for their study is collected in the same 1994 e^+p run period as the data underlying the study in this thesis. The H1 study uses the same kinematic constraints on event and particle selection as in the 1993 ZEUS analysis. This allows one a direct comparison of the two independent measurements, which is shown in figure 9.8. The results of H1 confirm, within the statistical errors, the measurement in this thesis. The statistical and systematic errors of the two measurements are uncorrelated since the analyses use distinct data samples and different detectors.

Collider	Experiment	Energy range	P_s/P_u	Method
e^+e^-	DELPHI [Abr95]	$\sqrt{s} = 90\,GeV$	0.23	Simultaneous tuning of MC parameters to K^0,$K^{*\pm}(892)$ and ρ^0 scaled momentum distributions.
	ALEPH [Bus94]	$\sqrt{s} = 90\,GeV$	0.3	Comparison with MC
	OPAL [Ale91, Ake95]	$\sqrt{s} = 90\,GeV$	0.285 ± 0.035	K^0 cross section
	CELLO [Beh90]	$\sqrt{s} = 35\,GeV$	0.3	Comparison with MC
	JADE [Bar83]	$\sqrt{s} = 12 - 35\,GeV$	$0.27 \pm 0.03 \pm 0.05$	Ratio $K^0/(ch.\,part.)$
	TASSO [Alt85]	$\sqrt{s} = 14 - 34\,GeV$	$0.35 \pm 0.02 \pm 0.05$	Ratio K^0/π cross section
	PLUTO [Ber81]	$\sqrt{s} = 30\,GeV$	0.14	Comparison with MC
	HRS [Der88, Aba90]	$\sqrt{s} = 29\,GeV$	0.34 ± 0.03	Simultaneous tuning of MC parameters to K^{*0}, ρ^0,D and Λ^0 cross section. Comparison to $K^{0,\pm}$ cross section
	TPC [Aih84]	$\sqrt{s} = 29\,GeV$	0.250 ± 0.016	Ratio K/π cross section
$p\bar{p}$	CDF [Abe89]	$\sqrt{s} = 1800\,GeV$	0.40 ± 0.05	
		$\sqrt{s} = 630\,GeV$	0.4 ± 0.2	Ratio $K/\pi^{\pm}$
	UA5 [Ans88]	$\sqrt{s} = 900\,GeV$	0.29 ± 0.02	
		$\sqrt{s} = 546\,GeV$	$0.28 \pm 0.02 \pm 0.03$	Ratio $K^0/\pi^{\pm}$
		$\sqrt{s} = 200\,GeV$	0.26 ± 0.03	
pp	ABCDHW [Bre84]	$\sqrt{s} = 45, 62\,GeV$	0.55 ± 0.02	Ratio K^+/π^+
ep (NC)	H1 [Aid96]	$< W >= 138\,GeV$	$\sim 0.2 - 0.23$	Comparison K^0 rates with MC
	This thesis	$< W >= 130\,GeV$	$0.2 < P_s/P_u < 0.3$	**Comparison K^0 rates with MC**
	WSL [Coh78]	$< W >= 3.15\,GeV$	0.13 ± 0.03	Ratios K^0/π^+, Λ/p
μN (NC)	E665 [Ada94]	$E_\mu = 490\,GeV$	~ 0.2	Ratio $K^0/\pi^{\pm}$, K^0 cross section
μp (NC)	EMC [Arn87]	$E_\mu = 280\,GeV$	$0.3 \pm 0.01 \pm 0.07$	Ratio $K/(ch.\,part.)$
$\bar{\nu}N$ (CC)	FIIM [Amm80]	$(2 \le W \le 10)\,GeV$	0.27 ± 0.04	Ratio K^0/π^-
$\bar{\nu}p$ (νp) (CC)	WA21 [Jon85] [Jon93]	$< W >\sim 5\,GeV$	$0.203 \pm 0.014 \pm 0.010$ 0.15	Ratio K^0/π^- (K^+/π^+) Comparison K^0 rates with MC

Table 9.1: Review of P_s/P_u values obtained from other experiments. The numbers are taken from the references as quoted in the second column. The errors, if given, are statistical and systematic, respectively. For more detailed information on the measurement see the corresponding references.

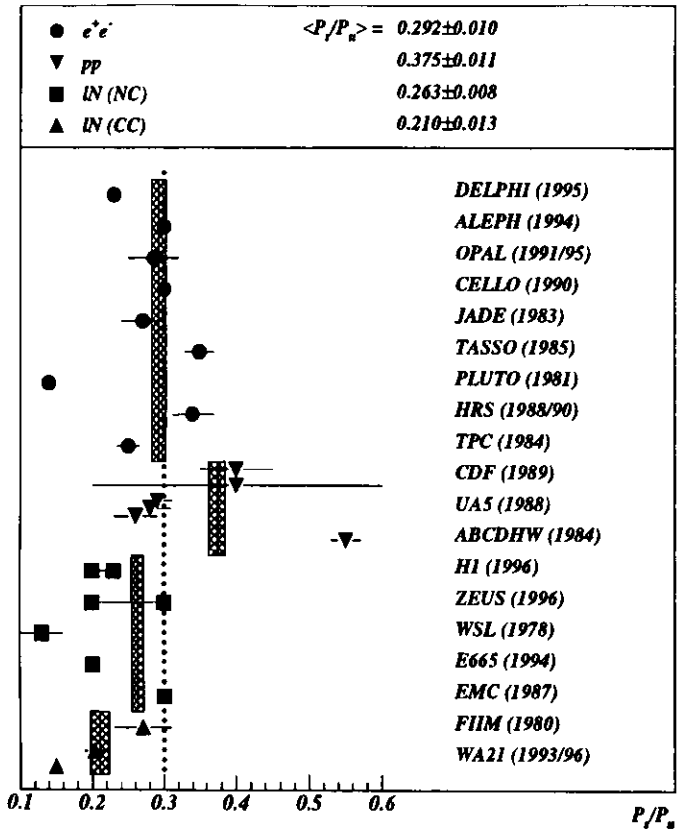

Figure 9.6: P_s/P_u values from other experiments as given in table 9.1. The errors, if given, are statistical only. The dotted line indicates the default value for P_s/P_u used in the JETSET Monte Carlo description of the fragmentation process. The hashed boxes indicate a two sigma window around the mean value obtained from a linear fit to the corresponding data points.

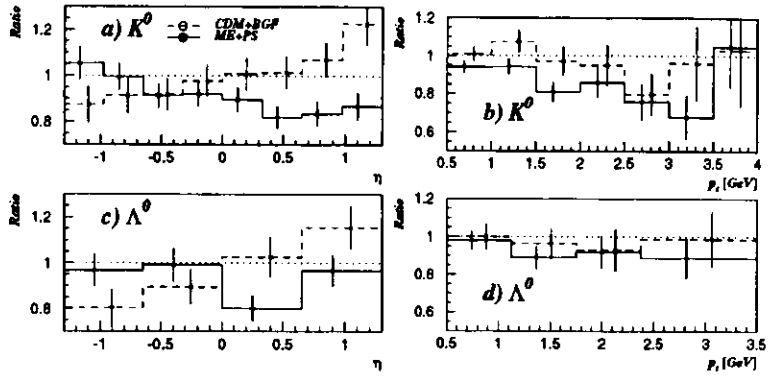

Figure 9.7: *Ratio of ZEUS 1994 e^+p to 1993 e^-p predicted MC differential multiplicities of neutral strange particles. The open circles are the ratios for CDM+BGF model, the solid circles the ratios for the ME+PS model. The error bars are statistical. The circles are shifted horizontally off the bin centre in order to allow an easy comparison. a), b) show the ratio of the predictions of pseudorapidity η and transverse momentum p_t for the K^0, c) and d) the corresponding ratios for the Λ^0.*

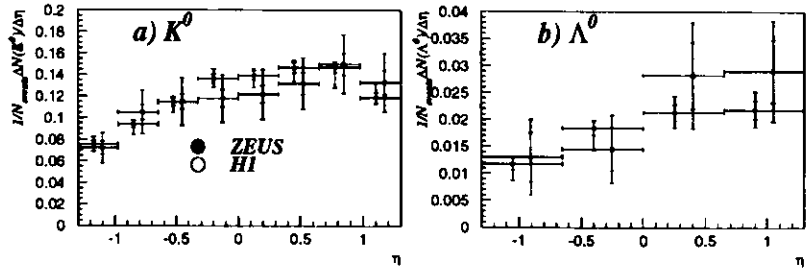

Figure 9.8: *Comparison of the differential multiplicities of neutral strange particles in 1994 e^+p DIS as measured with the H1 detector (open circles) and ZEUS (solid circles). The kinematic range for the selected events and the neutral strange particles for the ZEUS and H1 distribution are as established for the 1993 analysis. a), b) show the distribution for the pseudorapidity η for the K^0 and Λ^0, respectively. The data points are shifted horizontally off the bin centre in order to allow an easy comparison.*

Selected Kinematic Range		
$10\,GeV^2 < Q^2_{DA} < 1280\,GeV^2$		
$0.0003 < x_{DA} < 0.1$		
$y_{JB} > 0.04$		
1994 e^+p DIS Data Sample		
	$< n(K^0) >$ /event	$< n(\Lambda^0) >$ /event
Data	$0.406 \pm 0.005^{+0.001}_{-0.016}$	$0.053 \pm 0.002^{+0.003}_{-0.003}$
CDM+BGF	0.489 ± 0.005	0.075 ± 0.001
ME+PS	0.440 ± 0.006	0.071 ± 0.002
	$< n(\Lambda) >$ /event	$< n(\bar{\Lambda}) >$ /event
Data	$0.027 \pm 0.001^{-0.001}_{-0.005}$	$0.026 \pm 0.001^{+0.007}_{+0.003}$
CDM+BGF	0.039 ± 0.001	0.037 ± 0.001
ME+PS	0.036 ± 0.001	0.036 ± 0.001

Table 9.2: *K^0_S and Λ^0 multiplicities for 1994 DIS e^+p data sample.*

Selected Kinematic Range		
$10\,GeV^2 < Q^2_{DA} < 640\,GeV^2$		
$0.0003 < x_{DA} < 0.01$		
$y_{JB} > 0.04$		
1993 e^-p DIS Data Sample		
	$< n(K^0) >$ /event	$< n(\Lambda^0) >$ /event
Data	$0.313 \pm 0.009^{-0.005}_{-0.039}$	$0.047 \pm 0.005^{+0.012}_{-0.005}$
CDM+BGF $P_s/P_u = 0.3$	0.348 ± 0.008	0.067 ± 0.003
CDM+BGF $P_s/P_u = 0.3$	0.246 ± 0.003	0.050 ± 0.002
ME+PS	0.355 ± 0.005	0.067 ± 0.002
1994 e^+p DIS Data Sample		
	$< n(K^0) >$ /event	$< n(\Lambda^0) >$ /event
Data	$0.316 \pm 0.004^{+0.001}_{-0.012}$	$0.048 \pm 0.002^{+0.001}_{-0.005}$
CDM+BGF	0.350 ± 0.004	0.066 ± 0.001
ME+PS	0.322 ± 0.005	0.062 ± 0.002

Table 9.3: *K^0_S and Λ^0 multiplicities for 1993 DIS e^-p and 1994 DIS e^+p data samples.*

9.2 Particle and Energy Flow

In DIS, according to the picture of the quark parton model, the hadronic final state consists of a shower of particles originating from the struck quark. However, this simple picture needs substantial corrections introduced from QCD effects. Gluon and quark emissions, created by colour transfer between the struck quark and the proton remnant, fill the phase space between the current jet and the proton remnant. To study the production mechanism of the neutral strange particles, the production rate with respect to the hadronic axis, η_H (see formula 4.21), has been investigated. A restriction of $-1.0 < \eta_H < 1.0$ is made in order to insure that the current jet and a large portion of the colour flow region is within the acceptance for the reconstruction of neutral strange particles. This reduces a possible depletion of the observed production rate in the direction of the current jet or further backward. Figure 9.9 shows the event distribution in the x-Q^2 for the DIS data sample and lines of constant η_H. The solid lines emphasize the additional restriction in η_H.

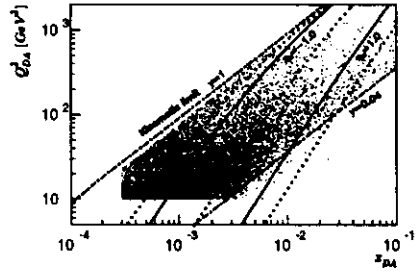

Figure 9.9: *Event distribution in the x-Q^2 for a DIS data sample. For clarity only a fraction of the selected sample is shown. The double angle method was used in order to reconstruct the kinematic variables. Lines of constant η_H are shown for $\eta_H = -1.5$ (dotted line), -1.0 (solid line), 0,(dotted line), 1 (solid line) and 1.5 (dotted lines).*

The reconstruction of η_H is based on equations 4.20 and 4.21. Figure 9.10 *a*) shows the reconstruction resolution for η_H for the two DIS MC samples. The reconstructed values $\eta_{H,rec.}$ tend to overestimate the "true" values $\eta_{H,gen.}$ systematically. The mean values of the systematic shifts are ~ 0.37 and ~ 0.23 for CDM+BGF and ME+PS

respectively. Both distributions are not symmetric with respect to the peak but show a tail towards higher values. In figure 9.10 *b*) the reconstructed η_H distributions for data and MC samples are compared. The MC distributions are normalized to the number of events in the data sample for easy comparison. The agreement between the reconstructed distributions for data and CDM+BGF MC is generally very good. The ME+PS sample shows an enhancement of $\sim 10\,\%$ in the region $-1.5 < \eta_H < -1.0$.

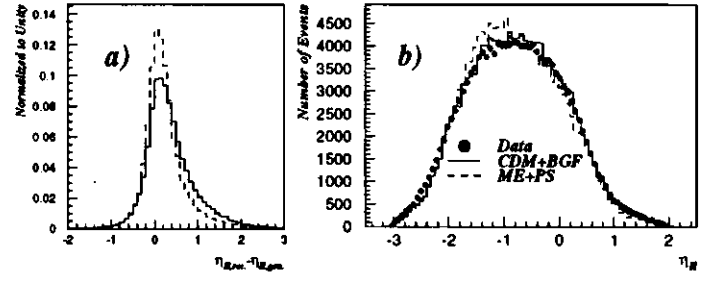

Figure 9.10: *a) η_H reconstruction resolution for the CDM+BGF (solid line) and ME+PS (dashed line) model. The distributions are normalized to unity for easy comparison of the results for the two models. b) Reconstructed η_H for data (circles), CDM+BGF (solid line) and ME+PS (dashed line) samples. The distributions for the two MC samples are normalized to the number of events in the data sample.*

The direction of the hadronic axis η_H depends on the event kinematics, *i.e.* is a function of Q^2,x and y. Therefore, detector effects lead to a dependence of the reconstruction resolution on these kinematic variables. The strongest dependence of the shift in the reconstruction of η_H is observed as function of the reconstructed Q^2_{DA} (see figure 9.11). Both MC predictions for this systematic show a behaviour that can be reasonably well described with a polynomial fit of second order in $\log_{10}(Q^2_{DA})$. However, the two distributions show significant differences in the absolute shift.

The reconstructed distribution of the data shows a better agreement with the reconstructed distribution of the CDM+BGF sample than with the ME+PS sample. Therefore, a correction of the reconstructed η_H using the fit results from the CDM+BGF distribution (upper half of figure 9.11) is chosen for the data sample. For each event a correction $\delta\eta_H$ is calculated as function of the reconstructed Q^2_{DA}

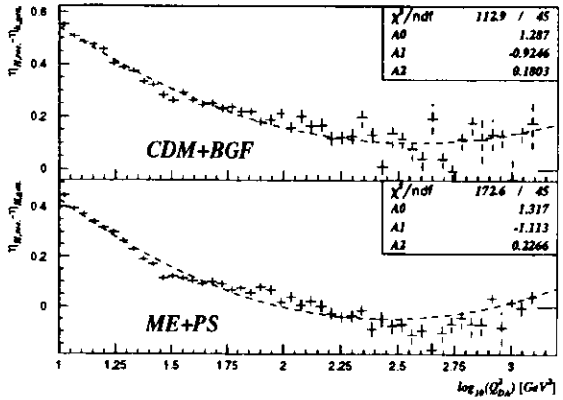

Figure 9.11: *Systematic shift in the reconstruction of η_H as function of $\log_{10}(Q^2_{DA})$ for CDM+BGF and ME+PS MC samples. The results of fits with a second order polynomial in $\log_{10}(Q^2_{DA})$ are overlaid, the results for the fit parameters are shown in the corresponding insets.*

and then subtracted from the reconstructed value of η_H. Figure 9.12 *a*) shows the resolution achieved after this correction is applied to the MC samples. The mean shift for the CDM+BGF sample is now 0.007. For the ME+PS sample the mean shift is 0.004 when using the fit parameters as obtained from the corresponding fit in the lower part of figure 9.11. If one applies the fit parameters as obtained from the fit to the CDM+BGF distribution, the distribution is overcorrected leading to a mean of -0.13. The resolution achieved (width of the distribution in figure 9.12 *b*)) is of the order ~ 0.4 units in rapidity. Figure 9.12 *a*) shows the reconstructed η_H distribution for the data before (open circles) and after the correction (solid circles) compared to the generated distributions of the two MC models. While the uncorrected data distribution shows a shift towards higher η_H, the corrected distribution reproduces the generated distributions reasonably well.

A total of 62466 events, $\sim 42\,\%$ of the selected DIS 1994 e^+p sample, is found within $-1.0 < \eta_H < 1.0$. The average corrected η_H in this subsample is ~ -0.3.

Figure 9.13 shows the differential production rate as function of the distance $\delta\eta$ with respect to the hadronic axis η_H for *a*) K^0 and *b*) Λ^0. As before, the inner

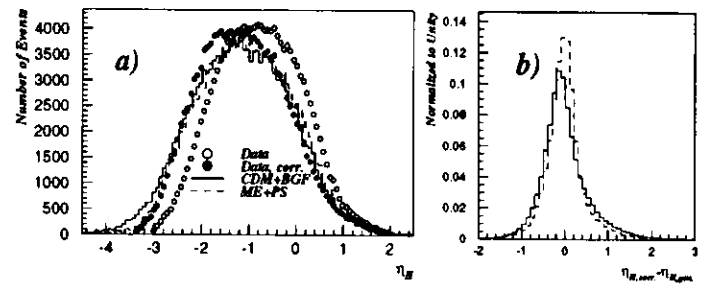

Figure 9.12: *a) Reconstructed and corrected η_H for data (solid circles), CDM+BGF (solid line) and ME+PS (dashed line) samples. Also shown, as open circles, is the uncorrected η_H distribution for the data. The distributions for the two MC samples are normalized to the number of events in the data sample. b) Reconstruction resolution of the corrected η_H for the CDM+BGF (solid line) and ME+PS (dashed line) model. The distributions are normalized to unity for easy comparison of the results for the two models.*

thicker error bars are statistical, the outer error bars show the statistical and systematic error added in quadrature. The systematic error is completely dominated by ϵ_{Method} suggesting systematic shifts between $-45\,\%$ and $+25\,\%$. The origin of these large systematic errors lies in the difference with which the two MC describe the reconstruction resolution of η_H. The influence of the reconstruction resolution of the particle pseudorapidity (see figure 8.15 in section 8.3) is negligible.

The kinematic restrictions of $-1.4 < \eta < 1.5$ for the K^0 and $-1.3 < \eta < 1.4$ for the Λ^0 and the restriction of η_H confine the distribution of $\delta\eta$ into $\sim -2.5 < \delta\eta < 2.5$. The distributions for both K^0_S and Λ^0 peak for values of $\delta\eta \sim 0.5$. Studies of the hadronic energy distributions (*e.g.* [Cro94]) show that the expectation of the QPM, a peak at $\delta\eta = 0$, is shifted towards the positive direction by about 0.5 units in pseudorapidity. This shift is due to QCD radiative processes, where the scattered quark loses some of its energy emitting a gluon. Therefore, the peaks of the $\delta\eta$ distributions for the K^0_S and Λ are in agreement with a production collimated around the hadronic axis, probably in the fragmentation process of the current jet. The distributions show an asymmetry between the production in the region between the hadronic axis and the proton remnant, $\delta\eta > 0.5$, and the more backward region $\delta\eta < 0.5$. The tail in the forward region includes the additional production of the K^0 and Λ^0 in the colour flux

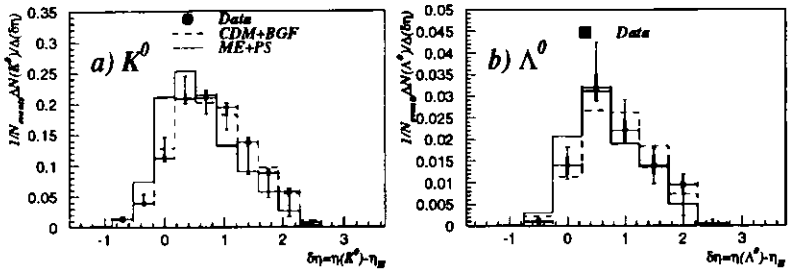

Figure 9.13: *Differential multiplicity as function of the distance $\delta\eta$ for a) K^0 and b) Λ^0. The kinematic range for the K^0 and Λ^0 are as established before. The distributions are normalized to the number of ZEUS 1994 e^+p events (N_{events}) with $10\,GeV^2 < Q^2 < 1280\,GeV^2$, $0.0003 < x < 0.1$, $y > 0.04$ and $-1.0 < \eta_H < 1.0$. The circles are the measured distributions for the K^0 and Λ^0, respectively. The horizontal error bars give the bin size, the thick vertical error bars show the statistical errors and the outer error bars correspond to the statistical and systematic errors added in quadrature. The solid and the dashed lines show the predictions of the ME+PS and CDM+BGF MC models, respectively, normalized to the multiplicity of the data.*

between the current jet and the proton remnant.

Overlaid are the predictions for the two MC models, normalized to the multiplicity of the data distribution. The CDM+BGF distribution reproduces well the shape of the data distribution for the K^0_S, while the ME+PS model predicts a collimation around the peak which is stronger than observed. For the Λ^0 distribution more data are necessary to distinguish between the two models.

The tail towards positive $\delta\eta$ is very sensitive to the lower bound of η_H. A variation in this lower bound changes the geometrical coverage of the available phase space for the fragmentation process in the colour flow region between the current jet and the proton remnant. A higher value of the lower bound rejects more events which have a larger portion of the colour flow region inside the acceptance region of the tracking detector. Due to the collimation of the current jet, the distribution at $\delta\eta < 0.5$ is not very sensitive to variations of the higher bound of η_H (as long as the current jet is contained within the region selected for the reconstruction of the neutral strange particles).

The measured multiplicities within this selected η_H range are listed in table 9.4.

The lower bound in η_H leads to a decrease of the measured multiplicities of $\sim 8\,\%$ (K^0) and $\sim 15\,\%$ (Λ^0). The CDM+BGF model predicts an even stronger decrease of $\sim 15\,\%$ $\sim 21\,\%$, while the ME+PS model, due to the stronger collimation of the particle flow, remains almost unaffected ($\sim 2\,\%$ and $\sim 3\,\%$, respectively).

Selected Kinematic Range		
$10\,GeV^2 < Q^2_{DA} < 1280\,GeV^2$ $0.0003 < x_{DA} < 0.1$ $y_{JB} > 0.04$ $-1.0 < \eta_H < 1.0$		
1994 e^+p DIS Data Sample		
	$< n(K^0) >$ /event	$< n(\Lambda^0) >$ /event
Data	$0.374 \pm 0.007^{-0.004}_{-0.026}$	$0.047 \pm 0.003^{+0.006}_{-0.002}$
CDM+BGF	0.417 ± 0.006	0.059 ± 0.002
ME+PS	0.430 ± 0.007	0.069 ± 0.002

Table 9.4: *K^0_S and Λ^0 multiplicities for 1994 DIS e^+p data sample with $-1.0 < \eta_H < 1.0$.*

Figure 9.14 shows the average energy per event (upper half) and average fraction of hadronic centre of mass energy W (lower half) carried by *a)* K^0 and *b)* Λ^0 as function of the distance $\delta\eta$. The upper distributions reproduce the shapes of the particle flow distributions in figure 9.13 up to a conversion factor $\sim 1.7\,GeV$ and $\sim 2.2\,GeV$ for the K^0 and Λ^0, respectively. These conversion factors reflect the average energy of the K^0 and Λ^0 as determined from their energy distributions. This simple scaling behaviour suggests again that the dominant production process is due to fragmentation rather than due to direct production (or decay of heavier, directly produced particles), since the latter mechanism(s) would lead to an enhancement of strange particles with higher energies in the direction of the current jet as compared to the strange particles in the colour flow (and fragmentation) region. The size and origin of the systematic shift and error is comparable to those of the particle flow

distributions. This is expected since the reconstruction of the energy E_{K^0,Λ^0} of the strange particles from the reconstructed invariant mass $m_{\pi\pi,p\pi}$ and momentum p_{K^0,Λ^0} introduces only small systematic effects.

Also interesting is what fraction $E_{K^0,\Lambda^0}/W$ the strange particles carry as a function of their distance from the current jet axis. Again, leading particles[1] are expected to carry a larger fraction than particles produced in the fragmentation process. The lower parts of figure 9.14 *a*) and *b*) show the distribution of the average fraction E_{K^0}/W and E_{Λ^0}/W as function of $\delta\eta$. The distribution for the K^0 exhibits a non-trivial structure that is compatible (fit with Gaussian plus linear function gives a $\chi^2/NDF = 0.65$) with an enhancement in the direction of the current jet (smeared by a Gaussian). A flat distribution is disfavoured (fit with a constant leads to a $\chi^2/NDF = 2.92$. In the Λ^0 distribution such enhancement, if existing, is hidden due to the low statistics. The systematic shifts and errors are consistent with those above. A further smearing is due to the reconstruction resolution of W^2.

A comparison between the MC predictions and the measured K^0 distributions show a good agreement for the CDM+BGF model. The ME+PS model predicts a stronger collimation of the energy flow around the current jet axis. However, it gives a fair description of the fractional energy flow. The MC predictions here are not normalized to the data multiplicities as in the particle flow distributions, the higher average multiplicity of the MC is compensated by a lower average energy carried by the K^0s. The integrated energy flows agree for both MC models within 2% ($\lesssim 1.25\,\sigma$). In case of the Λ^0, the predicted energy flow is higher by $\sim 30\,\%$ and $\sim 50\,\%$ for the CDM+BGF and ME+PS model, respectively. This reflects the predicted higher multiplicities for the Λ^0, the prediction for the average energy carried by the Λ^0 is in agreement with the measured value.

[1] This term refers here to particles that include the scattered quark or to the decay products of such particles.

[2] The double angle method with a correction as discussed in the next section is used.

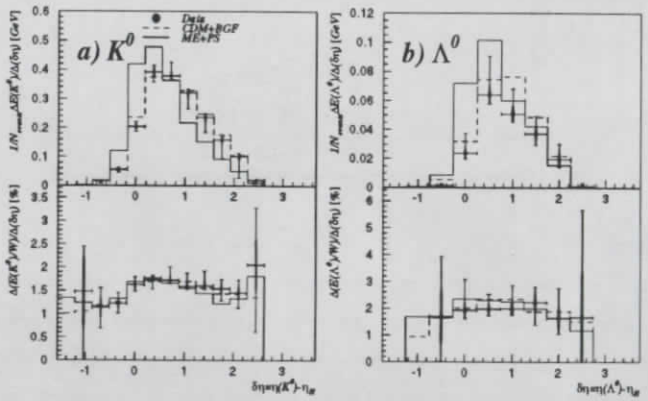

Figure 9.14: *Average energy per event (upper half) and average fraction of hadronic centre of mass energy (lower half) carried by a) K^0 and b) Λ^0 as function of the distance $\delta\eta$. The kinematic range for the K^0 and Λ^0 are as established before. The distributions are normalized to the number of ZEUS 1994 e^+p events (N_{events}) with $10\,GeV^2 < Q^2 < 1280\,GeV^2$, $0.0003 < x < 0.1$, $y > 0.04$ and $-1.0 < \eta_H < 1.0$. The circles are the measured distributions for the K^0 and Λ^0, respectively. The solid and the dashed lines show the predictions of the ME+PS and CDM+BGF MC models, respectively, normalized to the multiplicity of the data.*

9.3 Differential Multiplicities as a Function of Q^2 and W

9.3.1 Q^2 Dependence

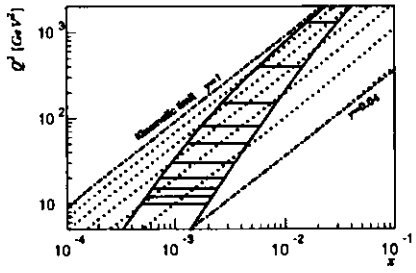

Figure 9.15: *Equidistant lines of constant W (dotted) in x-Q^2 plane are shown for $W = 300\,GeV$ ($\sim y = 1.0$) to $W = 60\,GeV$ ($\sim y = 0.04$) in steps of $40\,GeV$. The selected range in η_H (curved lines) and the bin definitions for the Q^2 analysis of the K^0 multiplicities (horizontal lines) are included.*

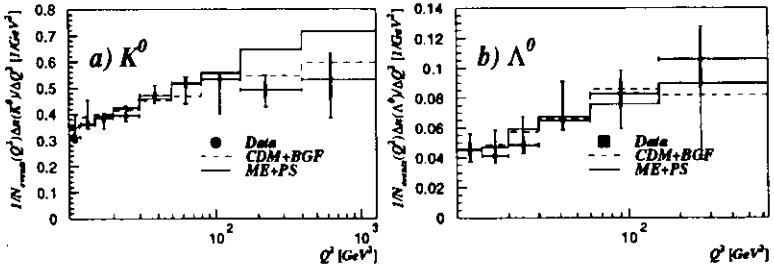

Figure 9.16: *Differential multiplicity as function of Q^2 for a) K^0 and b) Λ^0. The kinematic ranges for the K^0 and Λ^0 are as established before. In addition only events with with $-1.5 < \eta_H < 0.0$ are accepted. In each bin the number of reconstructed neutral strange particles is normalized to the number of ZEUS 1994 e^+p events ($N_{events}(Q^2)$) within this bin. The circles and squares are the measured distributions for the K^0 and Λ^0, respectively. The solid and the dashed lines show the predictions of the ME+PS and CDM+BGF MC models, respectively, normalized to the data.*

The mean multiplicity of neutral strange particle production as a function of Q^2 has been studied. Following the results of the previous section which showed that the production of neutral strange particles peaks in direction of the current jet ($\sim \eta_H + 0.5$), the analysis has been restricted to events with the additional criteria

$-1.5 < \eta_H < 0.0$ besides the established kinematic selection. The η_H are corrected as described in the previous section. Within this selected kinematic region (including the restriction in η_H), the direction of the current jet, and therefore of η_H, changes only slightly as a function of Q^2. With the data sample, a mean $\eta_H \sim -0.9$ for events with Q^2 between 10 and $12\,GeV^2$ has been determined, which increases to $\eta_H \sim -0.7$ for the events with $Q^2 > 200\,GeV^2$. The choice of the cutoff in η_H allows one to retain a large portion of the K^0 and Λ^0 of the colour flow region within the acceptance of the inner tracking detector, without varying this portion too much in the kinematic range under study. For events with $\eta_H \lesssim -1.0$ the tracking acceptance introduces a cut into the tail at negative $\delta\eta$. However, only small multiplicities are observed in this region and therefore the influence is small and is stable over the kinematic range.

Figure 9.15 shows the selected kinematic region and the bin definitions for the K^0 distribution. A total of 77302 events, $\sim 52\%$ of the selected DIS 1994 e^+p sample fulfills the additional requirement $-1.5 < \eta_H < 0.0$. The average corrected η_H in this subsample is ~ -0.8. The measured multiplicities in this kinematic range are listed in table 9.5.

Selected Kinematic Range		
$10\,GeV^2 < Q^2_{DA} < 1280\,GeV^2$		
$0.0003 < x_{DA} < 0.1$		
$y_{JB} > 0.04$		
$-1.5 < \eta_H < 0.0$		
1994 e^+p DIS Data Sample		
	$< n(K^0) >$ /event	$< n(\Lambda^0) >$ /event
Data	$0.416 \pm 0.006^{+0.027}_{+0.005}$	$0.056 \pm 0.003^{+0.011}_{+0.003}$
CDM+BGF	0.522 ± 0.007	0.080 ± 0.002
ME+PS	0.491 ± 0.008	0.081 ± 0.002

Table 9.5: *K^0_S and Λ^0 multiplicities for 1994 DIS e^+p data sample, restricted to $-1.5 < \eta_H < 0.0$.*

Figure 9.16 shows the differential *a*) K^0 and *b*) Λ^0 multiplicity as a function of Q^2. The multiplicities within each bin are normalized by the number of selected ZEUS 1994 e^+p DIS with a reconstructed Q^2_{DA} within this bin. The horizontal error bars define the bin boundaries, each abscissa corresponds to the mean Q^2 of the events in this bin. The statistical errors in the individual bins are $\sim 4\,\%$ for the K^0 and $\sim 10\,\%$ for the Λ^0. In the highest Q^2 bin the statistical error is approximately doubled. The systematic error is dominated by ϵ_{Method}. For the K^0 and $Q^2 > 15\,GeV^2$ the systematic shifts are generally less than 15 %, with an error of $\delta\epsilon_{Syst} \sim 8\,\%$. For $Q^2 < 15\,GeV$ the systematic shift reaches $\sim 20\,\%$. The dominant contribution to this systematic shift is due to the reconstruction resolution of Q^2_{DA}. The latter is of the order of $12 - 18\,\%$ (with a systematic shift of $\sim 2\,\%$), leading to non-negligible event migration effects and bin to bin migration in the low Q^2 bins. These effects lead to a systematic shift of up to 15 %, decreasing with increasing Q^2. Of importance is also the resolution of η_H[1] which also leads to event migration effects. Here the effective region of the particle flow covered by the (geometrical) acceptance of the tracking devices varies. Systematic shifts of up to 5 % are attributed to this origin. Contributions due to a varying signal to background ratio are of the order $\sim 6\,\%$. For the Λ^0 the upper limit in Q^2 is reduced to 640 GeV since no clear signal has been found above. The systematic shift varies between $\pm 25\,\%$ and $\delta\epsilon_{Syst} \sim 15\,\%$. Systematic shifts due to the reconstruction resolution of Q^2_{DA}, are of $\mathcal{O}(20\,\%)$, effects due to the reconstruction resolution of η_H contribute with up to $\sim 20\,\%$. Contributions due to a varying signal to background ratio are $\sim 1\,\%$, except for the highest Q^2-bin where it is $\sim 5\,\%$.

The choice of the bin definition is a compromise between the sensitivity to a rising Q^2 dependence and controllable systematics in the low Q^2 region and constrained by the statistics of the data sample with increasing Q^2.

The distributions of the CDM+BGF and ME+PS model are overlaid. Both MC

[1]The achieved resolution in the reconstruction of η_H improves to a mean shift of 0.006 and a width of ~ 0.3 units in rapidity, when restricted to $-1.5 < \eta_H < 0.0$.

distributions reproduce qualitatively the rise of the multiplicity with Q^2, suggested from the data. The MC distributions are normalized to give the same average multiplicity as the data. This removes the already established overall higher rates (as listed in table 9.5 for this selected kinematic region) and allows an easier comparison of the shapes of the distributions.

At this point the data suggest a rise of the production rate with increasing Q^2. From figure 9.15 it can be seen that the kinematic variables Q^2 and W are correlated. As Q^2 varies from $10\,GeV^2$ to $1280\,GeV^2$ W increases from $70\,GeV$ to $270\,GeV$. The statistics of the data sample and the possible kinematic bias at low Q^2 do not allow a sensitive study of the multiplicities as function of Q^2 at fixed values of W. However, the established agreement between the shapes of data and MC gives confidence to use the CDM+BGF MC sample, to decide whether this increase has to be attributed to Q^2 or rather to the corresponding increase in W.

Figure 9.17 shows the predictions of the CDM+BGF MC sample for the multiplicities of *a*) K^0 and *b*) Λ^0 as a function of Q^2 for different W ranges. For each distribution the mean value of W in the selected W range is quoted in the figure. Both, K^0 and Λ^0, show a rise of the multiplicity with increasing W. The K^0 distributions show, within the statistics, a behaviour which is consistent with only a small or no dependence on Q^2. It is concluded that the dominant contribution to the rise in the K^0 multiplicity with increasing Q^2 is due to an effective rise in W. However, the Λ^0 distributions suggest, within the limited statistics, a rise of the multiplicity with increasing Q^2 as well with increasing W.

9.3.2 *W Dependence*

In order to study the multiplicity as a function of W it is necessary to understand the reconstruction resolution of W. W is calculated from the kinematic variables Q^2 and x (using the double angle method) according to formula 4.9. Figure 9.18 *a*) shows the achieved resolution of W_{DA} for the CDM+BGF (solid line) and the ME+PS (dashed line) model for events passing the standard kinematic range selection criteria. A Gaussian fit to the CDM+BGF distribution suggests a systematic shift of $\sim -11\,\%$

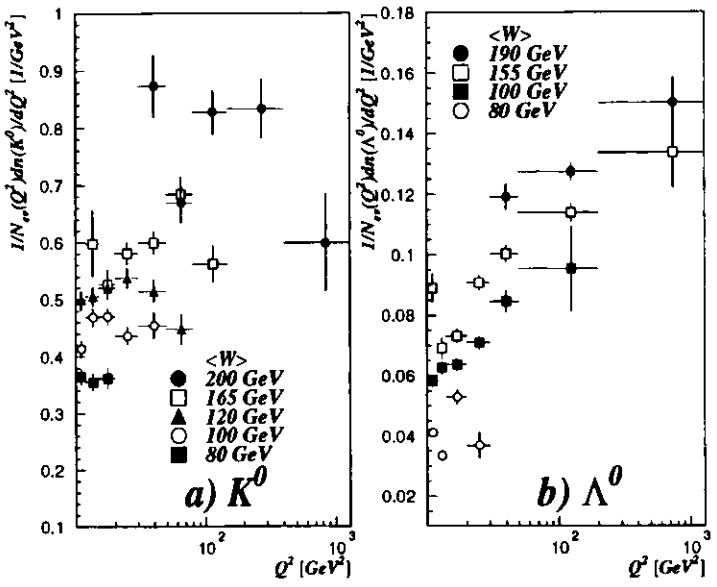

Figure 9.17: *CDM+BGF MC predicted differential multiplicity as function of Q^2 for a) K^0 and b) Λ^0 for several values of fixed W. The same selection criteria for events and particles as in figure 9.16 are applied to the MC sample. The error bars are scaled by a factor of 0.5 (0.25) for the K^0 (Λ^0) to allow a better distinction between the distributions of different $< W >$.*

and a width of $\sim 16\,\%$, for the ME+PS model a systematic shift of $\sim -7\,\%$ and a width of $\sim 13\,\%$ percent is obtained. If one restricts the reconstruction of W to events with $-1.5 < \eta_H < 0.0$ the widths of the resolutions are retained, the systematic shifts increase slightly by $\sim 1\,\%$. The size of the systematic shift is considered big enough to be corrected for.

Since W is reconstructed from the kinematic variables x and Q^2, a correction procedure as a function of these variables seems advisable. However, such a correction leads to technical disadvantages since the DIS selection cuts exclude certain regions of the x-Q^2-plane. Using equation 4.7, formula 4.9 can be expressed as linear function

in y and Q^2 :

$$W^2 = m_p^2 + sy - Q^2. \tag{9.1}$$

The selected DIS events cover the whole y-Q^2-plane. A bin by bin correction procedure, using an equidistant 20×25 grid in the y-$log_{10}(Q^2)$-plane, has been chosen to correct W_{DA} :

$$W_{cor.} = W_{DA} \cdot (1 - c(y, Q^2)) \tag{9.2}$$

where $c(y, Q^2) = \frac{W_{DA} - W_g}{W_g}(y, Q^2)$ as determined from the Monte Carlo sample. Figure 9.18 *b*) shows the uncorrected W_{DA} distribution for the DIS data sample and the two MC models. The shape of the data distribution is well reproduced from both MC models, which gives confidence that the reconstruction of W is modeled correctly. The CDM+BGF model has been chosen to determine $c(y, Q^2)$.

Figure 9.18 *c*) shows the corrected W distribution ($W_{cor.}$, solid circles) in comparison to the generated W distributions of the CDM+BGF (solid line) and the ME+PS (dashed line) model. Also shown is the uncorrected W_{DA} distribution (open circles) to visualize the influence of the correction. Again the MC predictions are in good agreement with the corrected data distribution. Figure 9.18 *d*) shows the predicted resolution for $W_{cor.}$. The systematic shifts are reduced to $\sim -2\,\%$ and $\sim -1\,\%$, the widths are $\sim 20\,\%$ and $\sim 16\,\%$ for CDM+BGF and ME+PS, respectively. For events with $-1.5 < \eta_H < 0.0$ the systematic shifts are retained, the widths of the resolutions improve slightly by $\sim 3\,\%$.

Figures 9.19 *a*) and *b*) show the rise of the mean multiplicity of neutral strange particle production as a function of W for the K^0 and Λ^0, respectively. The multiplicities within each bin are normalized by the number of selected ZEUS 1994 e^+p DIS with a corrected W_{DA} within this bin. The horizontal error bars define the bin boundaries, each abscissa corresponds to the mean W of the events in this bin. The statistical errors in the individual bins are $\sim 3 - 8\,\%$ for the K^0 and $\sim 10 - 23\,\%$ for the Λ^0. The systematic error is dominated by ϵ_{Method}. For the K^0 the systematic shifts are generally less than $15\,\%$, with an error of $\delta\epsilon_{Syst} \sim 6\,\%$. The systematic shift originates from differences in the reconstruction resolution of the corrected W_{DA} for

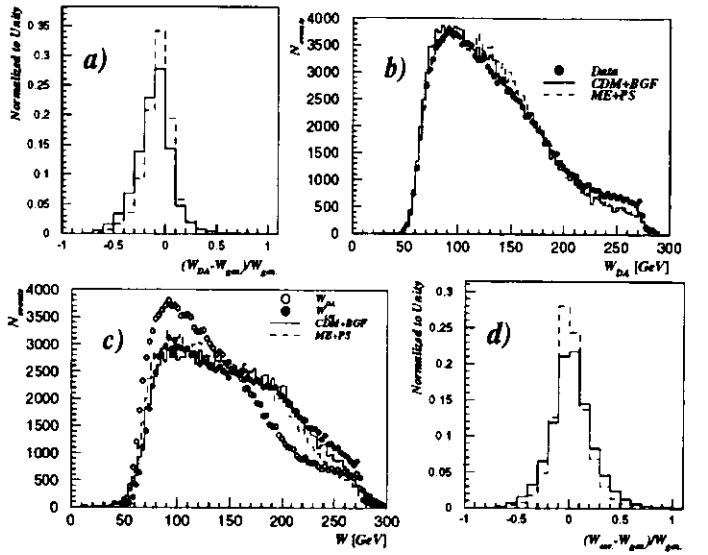

Figure 9.18: *a) W_{DA} reconstruction resolution for the CDM+BGF (solid line) and ME+PS (dashed line) model. The distributions are normalized to unity for easy comparison of the results for the two models. b) Reconstructed W_{DA} for data (circles), CDM+BGF (solid line) and ME+PS (dashed line) samples. The distributions for the two MC samples are normalized to the number of events in the data sample. c) Uncorrected W_{DA} (open circles) and corrected W_{DA} (circles) for data. The generated CDM+BGF (solid line) and ME+PS (dashed line) distributions are normalized to the number of events in the data sample. d) Reconstruction resolution for the corrected W_{DA} as determined from CDM+BGF (solid line) and ME+PS (dashed line)*

the two MC, migration effects due to the η_H resolution (leading to variations of the effectively covered particle flow region) and to a variation of the signal to background ratio. The individual contributions vary between $\sim 5-10\,\%$.

For the Λ^0 the systematic shift varies between $5-20\,\%$ and $\delta\epsilon_{Syst} \sim 15\,\%$ for $W < 160\,GeV$. The two highest W bins show larger fluctuations of $\sim \pm 40\,\%$, which are mainly due to the limited statistics in the MC samples. The origin of the systematic shifts are due to the W and η_H resolution, varying between $\sim 10-20\,\%$. Contributions due to a varying signal to background ratio are only $\sim 1\,\%$, except for the highest W-bin where it is $\sim 5\,\%$.

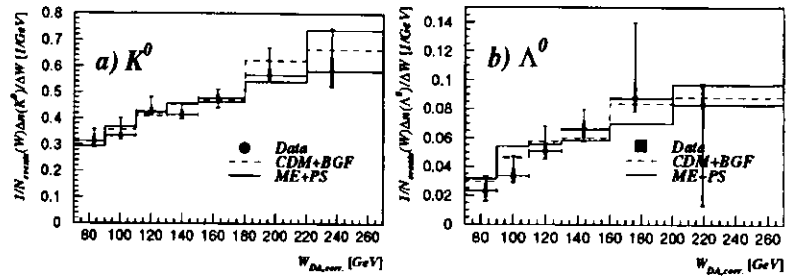

Figure 9.19: *Differential multiplicity as function of W for a) K^0 and b) Λ^0. The kinematic ranges for the K^0 and Λ^0 are as established before. In addition only events with with $-1.5 < \eta_H < 0.0$ are accepted. In each bin the number of reconstructed neutral strange particles is normalized to the number of ZEUS 1994 e^+p events ($N_{events}(W)$) within this bin. The circles and squares are the measured distributions for the K^0 and Λ^0, respectively. The solid and the dashed lines show the predictions of the ME+PS and CDM+BGF MC models, normalized to the multiplicity of the data.*

The distributions of the CDM+BGF and ME+PS model reproduce the rise of the multiplicity with W, suggested from the data. Again, the MC distributions are normalized to give the same average multiplicity as the data.

The observed rise of the K^0 and Λ^0 multiplicities with increasing W as dominating source, is attributed to the increase in the phase space, available for particle production in the fragmentation process of the hadronic system. This assumption is confirmed by an observed global rise in the charged particle multiplicity[1] with W. The ratio of the neutral strange to all charged particles constant stays constant. Therefore, no evidence for a suppression or enhancement of strange quark production with increasing W is observed.

[1]The charged particle multiplicity was hereby obtained as the number of tracks that fulfill the following constraints: 1) Only tracks within the same kinematic constraints as the daughter tracks of the neutral strange particles are accepted. 2) Tracks associated with the decay of neutral strange particles are removed. 3) The tracks have to originate from the event vertex.

9.4 Multiplicities for Events with and without Large Rapidity Gap.

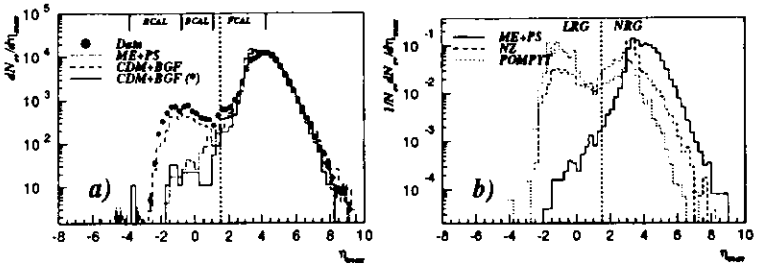

Figure 9.20: η_{max} *distribution for a) all selected 1994* e^+p *DIS events (circles). Overlaid are the MC predictions, normalized to the number of data events. The ME+PS (dash dotted line) and CDM+BGF(*) (solid line) MC samples are purely non-diffractive MC, while the CDM+BGF (dashed line) MC sample contains diffractive admixture. b) shows the predicted* η_{max} *distribution for the non-diffractive ME+PS MC (solid line) and the two diffractive MCs NZ (dashed line) and POMPYT (dotted line). The dotted vertical line indicates the classification as LRG and NRG events.*

The DIS data sample is a mixture of diffractive and non-diffractive events. As already mentioned in section 2.5, at ZEUS η_{max} can be used to separate subsamples that are dominated by events of either non-diffractive or diffractive type. Here η_{max}, is defined as the pseudorapidity of the most forward final state particles which are reconstructed from a set of adjacent cells in the UCAL. A threshold of 400 MeV is required for the sum of the cell energies. This choice of the threshold follows earlier studies of rapidity gap events in DIS (*i.e.* [Der93b, Der94b]) and is motivated to restrict final state particles to a pseudorapidity close to the true rapidity and to reduce the sensitivity to calorimeter noise.

Figure 9.20 *a*) shows the measured distribution of η_{max} for the selected 1994 e^+p DIS data sample (circles). As can be seen from the purely non-diffractive MC samples ME+PS (dash dotted line) and CDM+BGF(*)[1] (solid line), the distribution is well described for values above $\eta_{max} = 1.5$. However, the plateau at $\eta_{max} < 1.5$ as seen by

[1]This is the 1993 e^-p DIS MC.

Selected Kinematic Range		
$10\,GeV^2 < Q^2_{DA} < 1280\,GeV^2$		
$0.0003 < x_{DA} < 0.1$		
$y_{JB} > 0.04$		
Fraction of events with $\eta_{max} < 1.5$ [%]		
	all W	$W > 110\,GeV$
Data	5.9	6.9
ME+PS	0.6	0.7
CDM+BGF(*)	0.3	0.3
CDM+BGF	3.3	4.1
NZ	23.1	29.8
POMPYT	68.0	72.6

Table 9.6: *Percentage of LRG events with respect to the full 1994 DIS* e^+p *samples. The CDM+BGF (*) refers to the 1993* e^-p *DIS MC.*

the data cannot be reproduced. The non-diffractive MC show an exponential drop off. All η_{max} distributions are uncorrected for detector effects, such as seen *e.g.* as a drop in the event rate at $\eta_{max} \sim 1.1$ and $\eta_{max} \sim -0.75$. Here the acceptance is lower due to boundary effects between FCAL/BCAL and BCAL/RCAL, respectively. The geometric acceptances of the UCAL components are indicated at the upper boundary of the figure. Events with an η_{max} outside the geometric acceptance of the UCAL, *i.e.* $\eta_{max} > 4.3$ or $\eta_{max} < -3.8$, are an artifact of the clustering algorithm used to calculate η_{max} and may occur when energy is deposited in contiguous cells around the beam holes. Events with $\eta_{max} < 1.5$ are henceforth referred to as large rapidity gap events (LRG). This definition corresponds to a requirement of a rapidity gap of at least 2.8 units in rapidity. Events with $\eta_{max} > 1.5$ are said to have no rapidity gap (NRG).

The measured excess of LRG events cannot be explained with non-diffractive

scattering alone but needs a contribution from diffractive scattering processes. The CDM+BGF MC (dashed line) includes a diffractive component due to a pomeron-like part in the proton structure function, which qualitatively reproduces the measured distribution. However, the prediction for the fraction of LRG events is $\sim 40\,\%$ too low compared to the measured fraction. Figure 9.20 *b*) shows the predicted η_{max} distribution for two diffractive MC models, POMPYT (dotted line) and NZ (dashed line), as introduced in section 2.5.1 and 2.5.2, respectively. They both predict a plateau-like behaviour in the LRG region. For comparison, the non-diffractive ME+PS prediction is also shown (solid line). They also predict that a substantial fraction of diffractive events will be of NRG type. Table 9.6 lists the measured fraction of LRG events for the selected 1994 DIS e^+p data sample and the predictions for the different MC models.

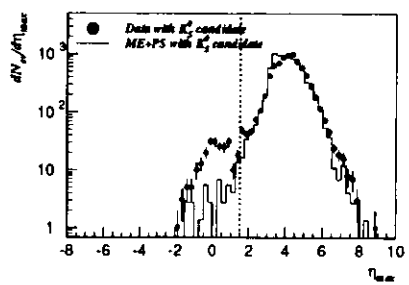

Figure 9.21: *η_{max} distribution for all selected 1994 e^+p DIS events with at least one reconstructed K^0_S candidate (circles). The corresponding (non-diffractive) ME+PSMC prediction is normalized to the number of events in the data sample.*

Figure 9.21 shows the measured η_{max} distribution for events with a reconstructed K^0_S candidate in comparison to the corresponding prediction of the non-diffractive ME+PS MC. Again the measured distribution shows an excess of LRG events. This excess can therefore be interpreted as strange particle production[1] in diffractive DIS. The ZEUS event display, figure 2.7, shows an example of K^0_S production in diffractive events. Two K^0_S candidates have been found in this event with reconstructed masses

[1] In this case K^0_S production. However, this excess is also observed for events with reconstructed Λ^0.

$m_{\pi^+\pi^-}$ of $510\,MeV$ and $493\,MeV$ and transverse momenta p_t of $0.9\,GeV$ and $1.9\,GeV$, respectively. The daughter tracks of these candidates are labeled with indexes 1 and 2 in the lower left inset of figure 2.7.

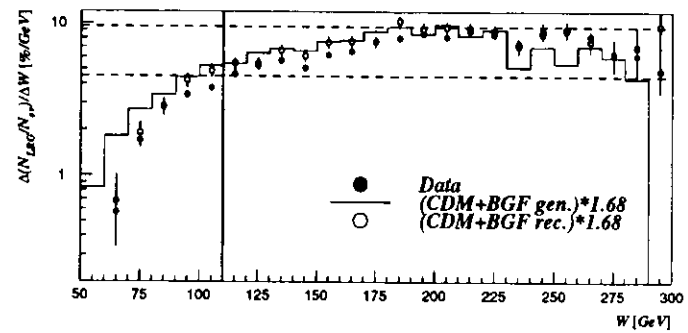

Figure 9.22: *Fraction of LRG events in the selected 1994 e^+p DIS data sample as function of the reconstructed invariant hadronic centre of mass energy W (solid circles). Also shown are the generated (line) and reconstructed fraction as predicted from the CDM+BGF MC sample. The MC predictions are scaled by a factor of 1.68 for easier comparison with the data distribution. The dashed lines indicate the range in which the fraction varies for $W > 110\,GeV$.*

Figure 9.22 shows the fraction of LRG events (without K^0 selection) in the selected data sample as a function of the reconstructed and corrected W (solid circles). For events with $W > 110\,GeV$ the contribution of LRG events to the DIS sample is roughly constant, $\sim 7 \pm 2.5\,\%$ (range indicated by dashed lines). For smaller W the fraction of LRG events drops strongly. This is because the hadronic final state is boosted into the forward direction, leading to a decrease in the acceptance for LRG events. Also shown in figure 9.22 is the predicted fraction as generated (line) and reconstructed (open circles) from the CDM+BGF MC. The MC distributions are scaled by a factor of 1.68, the ratio of the fractions of events with LRG ($W > 110\,GeV$) as seen in data and CDM+BGF MC (see table 9.6). This compensates for the underestimated fraction of LRG events in the CDM+BGF MC sample. The global shape of the measured fraction is well reproduced from the MC. The differences between the generated and reconstructed fractions are due to the reconstruction resolution of W. In order to avoid a kinematic bias when comparing multiplicities of events with and

without rapidity gaps this analysis is restricted to events with $W > 110\,GeV$. After this additional requirement, 109164 events remain. 101625 are of NRG type, 7539 are LRG events. A total of 5134 K^0_S over a background of 509 have been counted[1] in the NRG subsample, in the LRG subsample 176 K^0_S over a background of 8 have been determined. For the Λ^0, the counted signal over background ratio is 584/59 and 14/4 for the NRG and LRG subsamples, respectively. The yield of reconstructed Λ^0 within the LRG event sample is too small to perform a sensitive comparison between production mechanisms in NRG and LRG type events. This analysis is therefore restricted to the production of K^0s.

The correction method and the determination of the systematics in this section follows the discussion in the previous sections (see chapter 8). However, some adaptions have been made as listed below :

- The accepted kinematic range for reconstructed K^0_S is restricted to $0.3\,GeV < p_t < 3.0\,GeV$ and $\eta <\mid 1.3 \mid$. No clear signal for K^0_S in LRG events was found outside this range.

- Due to smaller available statistics the granularity of the effective acceptance correction grid (as introduced in section 8.2) has been reduced to 5 bins in p_t and 4 bins in η. A separate determination of the effective acceptance grid for LRG events (using the diffractive NZ and POMPYT MC and the "mixed" CDM+BGF MC events with $\eta_{max} < 1.5$) and NRG events (using the ME+PS and CDM+BGF MC events with $\eta_{max} > 1.5$) showed agreement within the errors[2]. The differences between the effective acceptances for LRG events from the two diffractive MC models separately are of the same order as the differences between the combined effective acceptance for NZ/POMPYT/CDM+BGF (LRG) and ME+PS/CDM+BGF (NRG). Therefore, only one effective acceptance grid has been determined for both LRG and NRG studies, using the combined statistics of events with and without rapidity gap in the combined ME+PS and CDM+BGF MC samples.

- The purities as introduced in section 8.1 have been determined separately for the selected data events with and without rapidity gap. The agreement between the two purity grids is usually better than $1\,\sigma$ in the bins with significant statistics (*i.e.* more than 20 candidates). However, the LRG events show a tendency ($\sim 5\,\%$ effect) to higher purity. For the other bins differences up to $4\,\sigma$ are observed. Again these are effects of $\sim 5 - 11\,\%$, mostly towards higher purity in the LRG events. The differences are considered big enough to do a separate purity correction for NRG and LRG events.

- The bin by bin correction of W_{DA} (see previous section 9.3) shows a systematic overcorrection of $\sim 7\,\%$ and a width of $\sim 18\,\%$ for MC events with LRG. Therefore, for LRG events the reconstructed W_{DA} are corrected bin by bin with correction factors determined from LRG events of the CDM+BGF MC. This improves the achieved reconstruction resolution of W for LRG events to a systematic shift of 0.7 %, 2.5 % and 2.7 % for the CDM+BGF, NZ and POMPYT MC sample, respectively. The width is $\sim 14\,\%$ for all three models.

- The systematic shifts and errors which are determined from MC samples are, in the case of the NRG distributions, extracted from all 4 MC samples. For the LRG distributions only CDM+BGF, NZ and POMPYT are used (ME+PS has not enough LRG events to provide a reasonable systematic study).

Figures 9.23 *a*) and *b*) show the differential K^0 multiplicity as a function of their pseudorapidity η and transverse momentum p_t for events with (squares) and without (circles) large rapidity gap. The multiplicities are normalized to the number of ZEUS 1994 e^+p DIS events (NRG or LRG, respectively) with $10\,GeV^2 < Q^2 < 1280\,GeV^2$, $0.0003 < x < 0.1$, $y > 0.04$ and $W > 110\,GeV$. The kinematic range for the K^0 is restricted to $\eta <\mid 1.3 \mid$ and $0.3\,GeV < p_t < 3\,GeV$. The measured multiplicities and

[1] The counting method 2 as introduced in section 8.1 has been used. The fit is applied to the mass spectra of all reconstructed candidates within the selected data samples (LRG and NRG subsamples separately).

[2] Note that the statistical error on the effective acceptance for LRG events reaches up to 40 %.

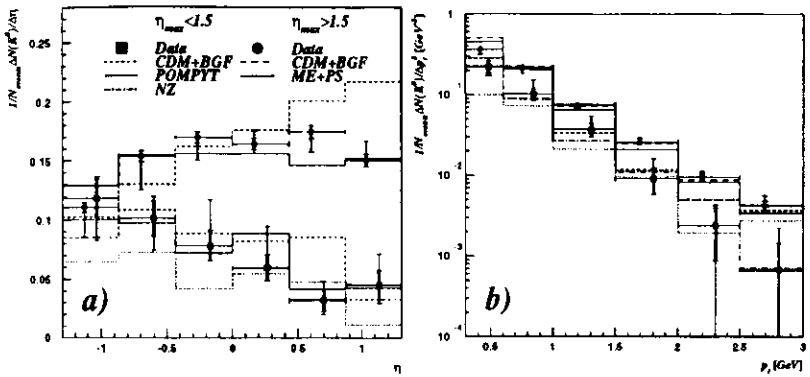

Figure 9.23: *Comparison of K^0 multiplicities as function of a) the pseudorapidity η and b) the transverse momentum p_t for events with (squares) and without (circles) rapidity gap.*

the MC predictions are listed for NRG and LRG events separately in table 9.7. The predictions of the ME+PS and CDM+BGF for the NRG events and NZ, POMPYT and CDM+BGF for the LRG events are overlaid in the figure. The measured multiplicities for NRG and LRG are $0.400 \pm 0.005^{+0.011}_{-0.028}$ and $0.188 \pm 0.014^{+0.032}_{-0.001}$, respectively. The statistical errors for NRG events in the individual η bins are $\sim 3\,\%$. In the two lower η bins, the systematic shifts of $(-17 \pm 6)\,\%$ and $(-12 \pm 6)\,\%$ are dominated by ϵ_{Method}. In the other η bins the systematic errors are $\epsilon_{Syst} \lesssim (5 \pm 6)\,\%$, as are all the individual contributions. For the p_t distribution the statistical errors increase from 2 to 7 % with increasing p_t. The systematic errors $\mid \epsilon_{Syst} \mid < 12\,\%$ are consistent with no systematic shift. For LRG events the statistical errors in the η bins vary between 12 and 30 %, with increasing p_t they increase from 14 to 40 %. The systematic errors suggest an underestimation of the rates by up to 50 % in the central η region and for some p_t bins, with $\delta\epsilon_{Syst} \gtrsim \sim 16\,\%$ (increasing with p_t). These large systematic uncertainties are mainly due to small statistics in the diffractive MC samples. Here the weighting procedure enhances even more the fluctuations in the reconstructed distributions. This leads to large values of ϵ_{Method}. In addition, the contribution of photoproduction events is found to be higher in LRG events ($\sim 6\,\%$) as compared

Selected Kinematic Range
$10\,GeV^2 < Q^2_{DA} < 1280\,GeV^2$
$0.0003 < x_{DA} < 0.1$
$y_{JB} > 0.04$
$W_{cor.} > 110\,GeV$

$< n(K^0) >$ /event, 1994 e^+p DIS Data Sample		
	$\eta_{max} < 1.5$ (LRG)	$\eta_{max} > 1.5$ (NRG)
Data	$0.188 \pm 0.014^{+0.032}_{-0.001}$	$0.400 \pm 0.005^{+0.011}_{-0.028}$
CDM+BGF	0.209 ± 0.017	0.428 ± 0.005
ME+PS	(0.472 ± 0.076)	0.387 ± 0.005
NZ	0.191 ± 0.015	0.203 ± 0.008
POMPYT	0.126 ± 0.012	0.202 ± 0.009

Table 9.7: *K^0_S multiplicities for 1994 DIS e^+p LRG/NRG data and MC samples.*

NRG events ($\sim 3\,\%$). The systematic shift ϵ_{PAP} is found to contribute with up to $\pm 12\,\%$.

A comparison of the distributions gives the following results :

- The measured K^0 multiplicities for NRG and LRG events show strong differences in the overall multiplicities. The average number of K^0 produced in an LRG event is roughly half the number as for NRG events. However, the average number of tracks[1] also drops by a factor ~ 2. This reflects that the mass M_X of the hadronic system observed in the detector is small for LRG events compared to NRG events, since QCD radiation is suppressed (see [Der94a]). Therefore, the number of K^0 scales as the general charged particle multiplicity and no indication for any strange quark enhancement or suppression is found in the

[1] Only tracks that are associated with the primary event vertex and fulfill the same "Foster" cuts (see section 7.1) as required for the daughter tracks of the strange particle candidates are taken into account.

production mechanism of LRG events.

- The shapes of the η distributions show strong differences between NRG and LRG events. While the NRG events reproduce the result of the inclusive[1] distribution (see section 9.1[2] and figure 9.1), the LRG events show a strong depletion towards the forward region (*i.e.* towards higher η). This reflects again the suppression of QCD radiation in the colour flow region for diffractive events.

- A comparison of the slopes of the p_t spectra for NRG and LRG events (as determined from fits similar to section 9.1) suggests a softer distribution for K^0 in LRG events than in NRG events. The fitted slopes are $(-1.52 \pm 0.16)\,GeV^{-1}$ (LRG) and $(-1.30 \pm 0.03)\,GeV^{-1}$ (NRG). However, this might be an artifact due to the low statistics in the LRG sample and more data are necessary.

- The discussion of differences between the measured η and p_t distribution and the corresponding prediction of the ME+PS and CDM+BGF MCs for NRG events follows section 9.1 and is therefore omitted here.

- A comparison between the measured multiplicity and the MC predictions for LRG events show a good agreement for the purely diffractive NZ MC and the "mixed" CDM+BGF[3]. POMPYT underestimates the measured K^0 multiplicity by $\sim 30\,\%$. However, the strange quark production in the fragmentation process is modeled like in the other MC samples. This suggests the necessity to include a strange quark component in the pomeron structure function. The ME+PS

[1] In this context "inclusive" is understood as DIS without distinction of NRG/LRG.

[2] Note however, that the accepted kinematic range for the K^0 is reduced in η as well as in p_t for the NRG/LRG events. This loss is by chance compensated by the higher average hadronic energy per event as introduced by the W cut. The emphasis is therefore more on the global shape of the distribution than on the absolute rates.

[3] The non-diffractive contribution of the CDM+BGF MC to the LRG events contributes only to $\sim 8\,\%$ while $92\,\%$ are diffractive photon-pomeron scattering events.

MC sample suggests a significantly (3.7σ) higher multiplicity than observed. However, the statistics are very small.

- The measured shapes of the η and p_t distributions show, within the limited statistics, good agreement with the MC predictions. The statistical error in the MC predictions is of equal size as for the data. More data and MC are needed to allow a distinction between the models and gain more information about the nature of the pomeron.

In order to investigate the shift to lower η values observed in the LRG events as compared to the NRG events, the particle flow with respect to the hadronic axis η_H has been studied. For this study η_H is restricted to the range $|\,\eta_H\,| < 1.0$. The arguments for this restriction as well as the method of reconstruction and correction of η_H follow section 9.2 exactly. However, the resolution of the uncorrected η_H shows a different behaviour for LRG events as for NRG events. For LRG events the reconstructed values $\eta_{H,rec.}$ show a smaller tendency to overestimate the true values $\eta_{H,gen.}$; a shift of ~ 0.1 units of rapidity for NZ and POMPYT and ~ 0.2 for CDM+BGF is observed. The NRG events for comparison show a shift of ~ 0.3 and ~ 0.4 units of rapidity for ME+PS and CDM+BGF, respectively. The different behaviour can be explained by the different event topologies, especially the suppression of energy deposits associated with the proton remnant in the LRG events. Therefore, the parameters of the polynomial in $log_{10}(Q^2_{DA})$ have been determined from the CDM+BGF MC sample with $\eta_{max} < 1.5$. This reduces the observed shifts for LRG events to ~ -0.02 for CDM+BGF and ~ -0.09 for NZ and POMPYT. The achieved resolution is ~ 0.3 for CDM+BGF and ~ 0.2 for NZ and POMPYT.

Figure 9.24 *a*) shows a comparison of the measured K^0 multiplicity as a function of $\delta\eta = \eta(K^0) - \eta_H$ for events with (squares) and without (circles) rapidity gap. For the NRG distribution the statistical errors are $\sim 3\,\%$ in the peak region, the systematic shifts are $\lesssim 15\,\%$ with an error of $\sim 10\,\%$. For LRG events the statistical errors are $\sim 10 - 30\,\%$, the systematic shifts vary between $\pm 40\,\%$ with an error of the same magnitude. The systematic studies for LRG and NRG show a consistency

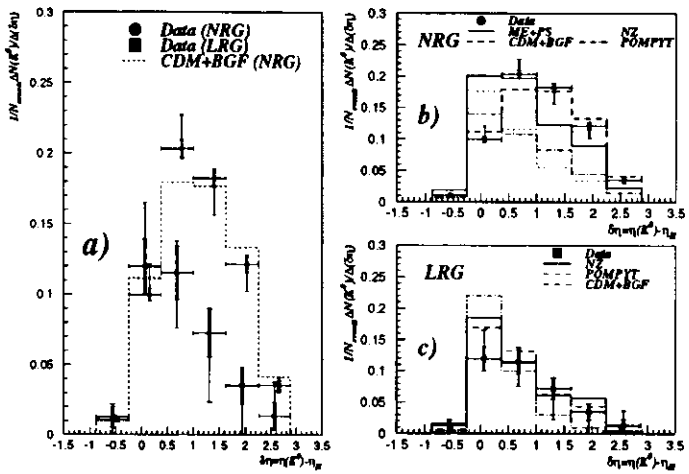

Figure 9.24: *Comparison of K^0 particle flow for events with and without rapidity gap. a) compares the measured distributions of LRG events with NRG events. The prediction for the CDM+BGF model (NRG only) is also included. b) and c) show the comparison of the measured particle flows with the MC predictions separately for NRG and LRG events, respectively.*

with no systematic shift. The main contribution to the systematic shifts arises from ϵ_{Method}, due to differences in the reconstruction resolution of η_H for the individual MC models. The particle flow distributions for events with and without large rapidity gap exhibit striking differences. The NRG distribution reproduces the properties of the (inclusive) distribution of section 9.2 : the peak of the distribution at $\delta\eta \sim 0.5$ and a tail with high K^0 multiplicity in the colour flux region. The LRG events on the other hand show a peak at $\delta\eta \sim 0$ and a narrower collimination of the particle flow due to a strong suppression of K^0 production in the colour flux region, where the systematic studies suggest an even stronger collimation than measured. These prominent features of K^0 production in LRG events can be interpreted as a direct consequence of a suppression of QCD radiation, in agreement with the assumption that the LRG events are dominantly of diffractive nature. However, this not a feature specific to the K^0s. It should rather be observed for all produced particles, *e.g.*

charged pions. Indeed, studies of energy flow in LRG events show this behaviour (see [Der94a]).

Figure 9.24 *b*) shows the NRG distribution as above in comparison with the two standard DIS MC models CDM+BGF and ME+PS (normalized to the data distribution). The results of section 9.2 are retained. Also shown are the predictions for the two diffractive MC models NZ and POMPYT, which exhibit a significant lower overall production rate and the suppressed QCD radiation due to the lack of colour transfer in the scattering process. Figure 9.24 *c*) shows the LRG data distribution together with the predictions of the diffractive MC models. All three models reproduce the shape of the measured distribution reasonably well[1], CDM+BGF and NZ also predict within the statistical errors the correct multiplicities. The POMPYT model, which does not include an s-quark content in the pomeron structure function, underestimates the measured multiplicity significantly.

Now with the understanding of the differences in the particle flow for the two event classes it is possible to understand the strong difference in the shape of the η distributions, figure 9.23 *a*), for LRG and NRG events. For large values of W the hadronic system (*i.e.* η_H) is predominantly oriented in the backward direction. In the LRG events production is collimated around the scattered quark direction and the production in the more forward region is suppressed. Therefore, the η distribution drops with increasing η. For the NRG events the production peak is shifted towards the forward direction and the more forward region is filled by K^0s produced in fragmentation processes in the colour flow region. This compensates for the predominantly backward orientation of η_H.

[1] Note that the distribution of the POMPYT MC is normalized to the data to cope for the much lower prediction. This allows an easier comparison of the shape of the distributions.

10

Summary and Outlook

This thesis has presented a first analysis of various aspects of neutral strange particle production in neutral current deep inelastic scattering of $27.5\,GeV$ positrons and $820\,GeV$ protons in the ZEUS experiment at HERA. The analysis is based on the data sample of the 1994 e^+p run period in which a integrated luminosity of $\sim 3.2\,pb^{-1}$ have been accumulated. Out of these, a clean sample of DIS events in the kinematic range $10\,GeV^2 < Q^2 < 1280\,GeV^2$, $0.0003 < x < 0.1$ and $y > 0.04$ has been extracted. For this sample the average K^0 and Λ multiplicities have been measured to $0.406 \pm 0.005^{+0.001}_{-0.016}$ and $0.053 \pm 0.002^{+0.003}_{-0.003}$, respectively. The kinematic range for the K^0 (Λ) was restricted to $0.3\,GeV < p_t < 6.0\,GeV$ ($0.3\,GeV < p_t < 4.0\,GeV$) and $-1.4 < \eta < 1.5$ ($-1.3 < \eta < 1.4$). About 30 % of the K^0 and 20 % of the Λ particles are predicted to be produced within this kinematic range. No differences between the production of Λ and $\bar{\Lambda}$ have been observed. The two current DIS Monte Carlo models CDM+BGF and ME+PS tend to overestimate the measured multiplicities and show significant differences in the shapes of the measured p_t and η distributions.

The particle and energy flow with respect to the struck quark direction has been studied. The observed shift of the peak associated with the scattered quark is in agreement with QCD radiation processes. A comparison with the prediction of the two standard DIS Monte Carlo models shows reasonable agreement for both models. However, the ME+PS model predicts a stronger collimation of the particle flow around the scattered quark axis than measured. The CDM+BGF model gives a good description of the measured distribution, especially in the colour flow region.

The dependence of the average K^0 and Λ production rates as function of the

four-momentum transfer, Q^2, and the hadronic center of mass energy, W, of the ep scattering process have been studied. A rise of the production rates with both, Q^2 and W, is observed. However, these kinematic variables are correlated and a reliable decision, whether the increase is due to an increase in Q^2 or W is not possible due to the limited statistics of the data. MC Studies predict for the K^0 a rise with W rather than with Q^2, while for the Λ no decision is possible.

The K^0 and Λ multiplicities in the kinematic range $10\,GeV^2 < Q^2 < 640\,GeV^2$, $0.0003 < x < 0.01$ and $y > 0.04$ are compared with the results from data from the 1993 run period with $26.7\,GeV$ electrons and $820\,GeV$ protons within the same kinematic region. The kinematic range for the K^0 (Λ) was hereby restricted to $0.5\,GeV < p_t < 4.0\,GeV$ ($0.5\,GeV < p_t < 3.5\,GeV$) and $|\,\eta\,| < 1.3$ ($|\,\eta\,| < 1.3$), including about 25 % (20 %) of the produced neutral strange particles. The measured multiplicities are in good agreement. This is expected since the γ^*p process is independent of whether the photon is emitted from an electron or positron.

The two standard MC models reproduce the shapes of the measured p_t and η, however, the predicted multiplicities are systematically higher. The MC parameter which controls the strange quark production in the fragmentation process, P_s/P_u, is set to 0.3. This corresponds to the world average value determined from e^+e^- collider experiments. However, the data presented in this thesis favour a lower value of $0.3 > P_s/P_u > 0.2$.

The production of K^0 in events with and without large rapidity gaps (LRG) with respect to the proton direction are compared in order to probe differences in diffractive and non-diffractive scattering processes. In LRG events a K^0 production rate significantly lower than in NRG events is observed. However, the ratio of K^0 to charged particles remains constant. Therefore, within the limited statistics available, the difference between K^0 production in LRG and NRG events is attributed to a lower invariant mass in the LRG events, rather than to an additional suppression or enhancement mechanism for strange particle production in LRG events. The diffractive MC models reproduce reasonably well the measured shapes of the η, p_t and particle

flow distribution. The particle flow distribution does not exhibit the shift of the peak associated with the scattered quark as observed in the inclusive NRG events. This shift is characteristic for QCD radiation processes, which is suppressed in diffractive scattering processes. The K^0 multiplicities of the NZ and CDM+BGF MC are in agreement with the measured multiplicity of $0.188 \pm 0.014^{+0.032}_{-0.001}$ K^0 per event. The POMPYT MC, which does not include s-quark content in the pomeron structure function underestimates the measured multiplicity by $\sim$ 30 %. This indicates the necessity to include a strange quark component into the pomeron structure function.

As can be seen above, the study of neutral strange particle production with the ZEUS experiment has proven to be able to test various aspects of the DIS scattering process. Of special interest are scattering processes of diffractive nature in which the study of neutral strange particle production can help to clarify the nature of the pomeron, which is at present far from being well understood. With the completion of the detector parts FTD and RTD, their understanding and inclusion in future analyses, the acceptance for particles in the tracking detector will improve and a widened kinematic range will be accessible, allowing one to test the existing MC models in a wider range. Together with the improvements in the HERA performance, which leads to a strong increase of accumulated data, topics that remained unresolved due to low statistics can be studied with higher scrutiny and new studies, such as Λ production in diffractive events, will become possible.

APPENDICES

A.1 Properties of Neutral Strange Particles

A.1.1 K^0 properties

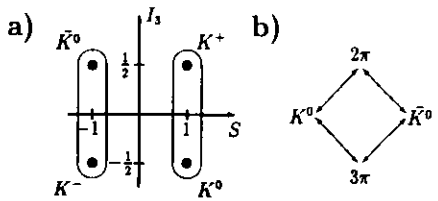

Figure A.1: *a) Two kaon isospin $I = \frac{1}{2}$ doublets with $S = -1$ and $S = 1$. b) K^0-$\bar{K}^0$ mixing : transition via (virtual) intermediate pion states.*

The charged kaons $K^{\pm}$ and the neutral kaons K^0 and $\bar{K}^0$ form two isospin doublets with strangeness $S = -1$ and $S = 1$, respectively, as shown in figure A.1.1 *a*). The strong interaction conserves I and I_3 as well as S. Therefore, the neutral kaon eigenstates of the strong interaction are the K^0 and $\bar{K}^0$. Strangeness conservation allows only associated production of s and $\bar{s}$ and prohibits a strong decay of the strange kaons. The decay of the kaons proceeds via the weak interaction. The neutral kaons both decay with $|\Delta S| = 1$, preferably into the same final two (or three) pion states. Thus second-order weak interactions allow transitions between K^0 and $\bar{K}^0$. The two states are therefore coupled and the eigenstates of the weak interaction are superpositions of these. This follows also from the observation that weak interactions do not conserve charge conjugation C or parity P but the combination CP[1]. The neutral kaons are not eigenstates of CP :

$$CP \mid K^0 >= - \mid \bar{K}^0 >$$
$$CP \mid \bar{K}^0 >= - \mid K^0 >$$

However, it is possible to construct eigenstates of CP :

$$\mid K_1^0 > = 1/\sqrt{2}(\mid K^0 > - \mid \bar{K}^0 >)$$
$$\mid K_2^0 > = 1/\sqrt{2}(\mid K^0 > + \mid \bar{K}^0 >)$$

[1] The CP-violation observed in the neutral kaon system is of $O(10^{-3})$ and here disregarded.

K^0

Quark content	$d\bar{s}$, 50% K^0_S, 50% K^0_L
$I(J^P), S$	$\frac{1}{2}(0^-), +1$
Mass	$m = (497.672 \pm 0.031)\, MeV$
Mass splittings	$m_{K^0} - m_{K^\pm} = (3.995 \pm 0.034)\, MeV$
	$m_{K^0_L} - m_{K^0_S} = (3.510 \pm 0.018) \times 10^{-12}\, MeV$

K^0_S

Mean life time	$\tau = (0.8926 \pm 0.0012) \times 10^{-10}\, s$
Proper life time	$c\tau = 2.676\, cm$
K^0_S decay mode	Fraction (Γ_i/Γ)
$\pi^+\pi^-$	$(68.61 \pm 0.28)\,\%$
$\pi^0\pi^0$	$(31.39 \pm 0.28)\,\%$
$\pi^+\pi^-\gamma$	$(1.78 \pm 0.05) \times 10^{-3}$
$\gamma\gamma$	$(2.4 \pm 1.2) \times 10^{-6}$
$\pi^+\pi^-\pi^0$	$< 8.5 \times 10^{-5}$
$3\pi^0$	$< 3.7 \times 10^{-5}$
$\pi^\pm e^\pm \nu$	$(6.68 \pm 0.10) \times 10^{-4}$
$\pi^\pm \mu^\pm \nu$	$(4.66 \pm 0.10) \times 10^{-4}$
$\mu^+\mu^-$	$< 3.2 \times 10^{-7}$
e^+e^-	$< 1.0 \times 10^{-5}$
$\pi^0 e^+ e^-$	$< 1.1 \times 10^{-6}$

K^0_L

Mean life time	$\tau = (5.17 \pm 0.04) \times 10^{-8}\, s$
Proper life time	$c\tau = 15.49\, m$
K^0_L decay mode	Fraction (Γ_i/Γ)
$3\pi^0$	$(21.6 \pm 0.8)\,\%$
$\pi^+\pi^-\pi^0$	$(12.38 \pm 0.21)\,\%$
$\pi^\pm \mu^\mp \nu$	$(27.0 \pm 0.4)\,\%$
$\pi^\pm e^\mp \nu$	$(38.7 \pm 0.5)\,\%$

Table A.1: *Excerpt of the K^0 properties from [Par96]*

with

$$CP \mid K^0_1 > = \mid K^0_1 >$$
$$CP \mid K^0_2 > = - \mid K^0_2 >$$

K^0_1 and K^0_2 are distinguished by their decay modes determined by the eigenvalue of the CP operator. The K^0_1 state decays mainly into two pion states[1] and is therefore identified as the K^0_S' "S" standing for "short-lived". The K^0_2 decays solely into a 3 pion system, reducing the available phase-space and therefore the decay rates. The K^0_2 is therefore identified as the "long-lived" version K^0_L.

A.1.2 Λ properties

Λ	
Quark content	uds
$I(J^P), S$	$0(\frac{1}{2}^+), -1$
Mass	$m = (1115.684 \pm 0.006)\, MeV$
Mean life time	$\tau = (2.632 \pm 0.020) \times 10^{-10}\, s$
Proper life time	$c\tau = 7.89\, cm$
Λ decay mode	Fraction (Γ_i/Γ)
$p\pi^-$	$(63.9 \pm 0.5)\,\%$
$n\pi^0$	$(35.8 \pm 0.5)\,\%$
$n\gamma$	$(1.75 \pm 0.15) \times 10^{-3}$
$p\pi^-\gamma$	$(8.4 \pm 1.4) \times 10^{-4}$
$pe^-\bar{\nu}_e$	$(8.32 \pm 0.14) \times 10^{-4}$
$p\mu^-\bar{\nu}_\mu$	$(1.57 \pm 0.35) \times 10^{-4}$

Table A.2: *Excerpt of Λ^0 properties from [Par96]*

[1] It is possible to construct 3 pion states with positive CP eigenvalues for angular momenta $l > 0$. However, decays of K^0_1 into such states are strongly suppressed by angular momentum barrier effects.

A.2 Glossary

ADAMO "Aleph DAta MOdel". Entity-Relationship model for defining tabular data structures and for manipulating and validating them from analysis programs.

ALHALO2 PHANTOM routine to identify beam halo muons.

BCAL Barrel CALorimeter.

CTD Central Tracking Detector.

DESY Deutsches Elektronen Synchrotron. German research institute in Hamburg.

DIS Deep Inelastic Scattering. Scattering processes with large momentum transfer between the interacting particles.

ELECT5 Analysis routine to reconstruct electrons from the energy depositions in the UCAL. Part of the PHANTOM library.

EEXOTIC Analysis routine to reconstruct electrons from the energy depositions in the UCAL. Part of the PHANTOM library.

EVB EVent Builder.

η_H Pseudorapidity associated with the scattered quark.

η_{max} Pseudorapidity of most forward energy deposit in UCAL above a 400 MeV energy threshold.

FCAL Forward CALorimeter.

EVTAKE PHANTOM routine that rejects events on basis of the detector and running conditions at the time of the data taking.

FLT First Level Trigger.

GFLT Global First Level Trigger.

GSLT Global Second Level Trigger.

HERA Hadron Elektron Ring-Anglage. Electron (positron) proton collider at DESY.

ISITAMU PHANTOM routine to identify muons in the detector.

LOCAL Analysis routine to reconstruct electrons from the energy depositions in the UCAL. Part of the PHANTOM library.

LRG events "Large Rapidity Gap" events. In DIS events with $\eta_{max} < 1.5$ (no hadronic energy between the proton (remnant) and the current jet).

LUMI LUMInosity detector.

MOZART "MOnte carlo for Zeus Analysis Reconstruction and Trigger". Software program to simulate ZEUS detector.

NRG events "No Rapidity Gap" events. In DIS events with $\eta_{max} > 1.5$ (region between proton remnant and current jet filled with hadronic activity due to colour flow).

PHANTOM "PHysics ANalysis Techniques, Operations and Methods". ZEUS software library for analysis routines.

PMT PhotoMultiplier Tube.

RCAL Rear CALorimeter.

RG "Rapidity Gap". Interval of (pseudo-) rapidity without hadronic activity above a energy threshold above 400 MeV.

RMSPARK PHANTOM routine to reject events which are due to PMT discharges.

SLT Second Level Trigger.

TLT Third Level Trigger.

UCAL "Uranium CALorimeter". The combination of FCAL,BCAL and RCAL.

V0FIND PHANTOM routine to reconstruct secondary the vertex of a decaying neutral particle.

VCTPAR ADAMO table containing the parameters of all reconstructed tracks.

VCTRAK ZEUS tracking package to reconstruct the event vertex and the trajectories of charged particles traversing the inner tracking system.

VCTRHL ADAMO table containing the parameters of all reconstructed tracks which are associated with the primary event vertex.

VCTVTX ADAMO table containing the parameters of the reconstructed event vertex.

VXD Vertex detector.

ZEUS Detector experiment in the south experimental area of the HERA collider facility.

ZGANA ZEUS trigger simulation software.

Bibliography

[Aba90] S. Abachi et al.; HRS Collaboration. Quark Hadronization Probed by K^0 Mesons. *Phys. Rev.*, D41:2045–2056, 1990.

[Abe89] F. Abe et al.; CDF Collaboration. K^0_S Production in $p\bar{p}$ Interactions at $\sqrt{s} = 630$ and $1800\,GeV$. *Phys. Rev.*, D40:3791–3794, 1989.

[Abr95] P. Abreu et al.; DELPHI Collaboration. Production Characteristics of K^0 and Light Meson Resonances in Hadronic Decays of the Z^0. *Z. Phys.*, C65:587–602, 1995.

[Ada94] M.R. Adams et al.; E665 Collaboration. Production of Neutral Strange Particles in Muon-Nucleon Scattering at $490\,GeV$. *Z. Phys.*, C61:539–549, 1994.

[Ahm94a] T. Ahmed et al.; H1 Collaboration. Deep Inelastic Scattering with a Large Rapidity Gap at HERA. *DESY-94-133*, 1994.

[Ahm94b] T. Ahmed et al.; H1 Collaboration. Observation of Hard Processes in Rapidity Gap Events in γp Interactions. *DESY-94-198*, 1994.

[Aid96] S. Aid et al.; H1 Collaboration. Strangeness Production in Deep-Inelastic Positron-Proton Scattering at HERA. *DESY-96-122*, 1996.

[Aih84] H. Aihara et al. Charged Hadron Production in e^+e^- Annihilation at $29\,GeV$. *Phys. Rev. Lett.*, 52:577–580, 1984.

[Ake95] R. Akers, et al.; OPAL Collaboration. The Production of Neutral Kaons in Z^0 Decays and their Bose-Einstein Correlations. *Z. Phys.*, C67:389–402, 1995.

[Ale91] G. Alexander et al.; OPAL Collaboration. A Study of K^0_S Production in Z^0 Decays. *Phys. Lett.*, B264:467–475, 1991.

[Alt85] M. Althoff et al.; TASSO Collaboration. A Detailed Study of Strange Particle Production in e^+e^- Annihilation at High Energy. *Z. Phys.*, C27:27–37, 1985.

[Amm80] V. V. Ammosov et al.; Fermilab-IHEP-ITEP-Michigan Univ. Coll. Measurement of SU(3) Symmetry Violation in the Quark Jet. *Phys. Lett.*, B93:210–212, 1980.

[And83] B. Andersson, G. Gustavson, G. Ingelman and T. Sjöstrand. Parton Fragmentation and String Dynamics. *Phys. Rep.*, 9:31–145, 1983.

[And91] A. Andresen et al.; ZEUS Calorimeter Group. Construction and Beam Test of the ZEUS Forward and Rear Calorimeter. *Nuclear Instruments & Methods in Physics Research*, A309:101–142, 1991.

[Ans88] R. E. Ansorge et al.; UA5 Collaboration. Kaon Production in $\bar{p}p$ Interactions at C.M. Energies from 200 to $900\,GeV$. *Z. Phys.*, C41:179–190, 1988.

[Arn87] M. Arnedo et al.; European Muon Collaboration. Strangeness Production in Deep Inelastic Muon Nucleon Scattering at $280\,GeV$. *Z. Phys.*, C34:283–291, 1987.

[Bad92] B. Badelek, K. Charchuła, M. Krawczyk, J. Kwieciński. Small-x Physics in Deep-Inelastic Lepton-Hadron Scattering. *Rev. Mod. Phys.*, 64:927–960, 1992.

[Bar83] W. Bartel et al.; JADE Collaboration. Charged Particle and Neutral Kaon Production in e^+e^- Annihilation at PETRA. *Z. Phys.*, C20:187–206, 1983.

[Bar94] E. Barberis et al. On the Properties of Diffractive Events in Deep-Inelastic ep Scattering. *ZEUS-Note 94-37*, 1994.

[Beh90] H.-J. Behrend et al.; CELLO Collaboration. Inclusive Strange Particle Production in e^+e^- Annihilation. *Z. Phys.*, C46:397–403, 1990.

[Ben87] M. Bengtson, G. Ingelman, T. Sjöstrand. Parton Cascade Evolution and Event Structure at HERA. In R. D. Peccei, editor, *Proceedings of the HERA Workshop*, volume 1, pages 149–165, 1987.

[Ber81] Ch. Berger et al.; PLUTO Collaboration. Inclusive K^0 Production in e^+e^- Annihilation for $9.3 < \sqrt{s} < 31.6\,GeV$. *Phys. Lett.*, B104:79–83, 1981.

[Bjo69] J. D. Bjorken and E. A. Paschos. Inelastic Electron-Proton and γ-Proton Scattering and the Structure of the Nucleon. *Phys. Rev.*, 185:1975–1982, 1969.

[Blo69] E. D. Bloom et al. High-Energy Inelastic $e-p$ Scattering at 6° and 10°. *Phys. Rev. Lett.*, 23:930–934, 1969.

[Bon88] R. Bonino et al.; UA8 Experiment. Evidence for Transverse Jets in High-Mass Diffraction. *Phys. Lett.*, B211:239–246, 1988.

[Bre69] M. Breidenbach et al. Observed Behavior of Highly Inelastic Electron-Proton Scattering. *Phys. Rev. Lett.*, 23:935–939, 1969.

[Bre84] A. Breakstone et al.; Ames-Bologna-CERN-Dortmund-Heidelberg-Warsaw Collab. High $p_t K^{\pm}/\pi^{\pm}$ Production in $p-p$ Collisions at the ISR; Strangeness Suppression and Gluon Effects. *Phys. Lett.*, B135:510–514, 1984.

[Bru94] P. Bruni and G. Ingelman. POMPYT Version 2.4 - A Monte Carlo to Simulate Diffractive Hard Scattering Processes. *DESY draft*, 1994.

[Bus94] D. Buskulic et al.; ALEPH Collaboration. Production of K^0 and Λ in Hadronic Z^0 Decays. *Z. Phys.*, C64:361–387, 1994.

[Cal69] C. G. Callan and D. J. Gross. High Energy Electroproduction and the Constituents of the Electric Current. *Phys. Rev. Lett.*, 22:156–159, 1969.

[Chl94] F. Chlebana. Description of the ZEUS Global Second Level Trigger in 1994. *ZEUS-Note 94-102*, 1994.

[Coh78] I. Cohen et al. Inclusive K^0_S and Λ Electroproduction. *Phys. Rev. Lett.*, 40:1614–1617, 1978.

[Cor92] F. Corriveau. The FLD Package for Magnetic Field Retrival in ZEUS. *ZEUS-92-091*, 1992.

[Cro94] M. B. Crombie. Hadronic Energy Distributions in Deep-Inelastic Electron-Proton Scattering. PhD Thesis, 1994.

[Der88] M. Derrick et al.; HRS Collaboration. Hadron Production in e^+e^- Annihilation at $\sqrt{s} = 29\,GeV$. *Phys. Rev.*, D35:2639–2649, 1988.

[Der93a] M. Derrick et al.; ZEUS Collaboration. Hadronic Energy Distributions in Deep Inelastic Electron-Proton Scattering. *Zeit. f. Phys.*, C59:231–242, 1993.

[Der93b] M. Derrick et al.; ZEUS Collaboration. Observation of Events with a Large Rapidity Gap in Deep Inelastic Scatteringat HERA. *Phys. Lett.*, B315:481–493, 1993.

[Der94a] M. Derrick et al.; ZEUS Collaboration. Comparison of Energy Flows in Deep Inelastic Scattering Events with and without Large Rapidity Gap. *Phys. Lett.*, B338:483–496, 1994.

[Der94b] M. Derrick et al.; ZEUS Collaboration. Observation of Jet Production in Deep Inelastic Scattering with a Large Rapidity Gap at HERA. *Phys. Lett.*, B332:228–243, 1994.

[Der94c] M. Derrick et al.; ZEUS Collaboration. Proposal for a Presampler for the Forward and Rear Uranium-Scintillator Calorimeter in ZEUS. *ZEUS-Note 94-001,DESY PRC 94-01*, 1994.

[Der95a] M. Derrick et al.; ZEUS Collaboration. Cross Section Measurement of Diffractive Production in Deep Inelastic Scattering. *Collaboration Draft*, 1995.

[Der95b] M. Derrick et al.; ZEUS Collaboration. Diffractive Hard Photoproduction at HERA and Evidence for the Gluon Content of the Pomeron. *Phys. Lett.*, B356:129–146, 1995.

[Der95c] M. Derrick et al.; ZEUS Collaboration. Neutral Strange Particle Production in Deep Inelastic Scattering at HERA. *Zeit. f. Phys.*, C68:29–42, 1995.

[Der95d] M. Derrick et al.; ZEUS Collaboration. Observation of Hard Scattering in Photoproduction Events with a Large Rapidity Gap at HERA. *HEP-EX-9501011*, 1995.

[Der95e] M. Derrick et al.; ZEUS Collaboration. Properties of Diffraction and Measurement of the Diffractive Structure Function in Deep Inelastic Scattering at HERA. *Collaboration Draft*, 1995.

[Der96a] M. Derrick et al.; ZEUS Collaboration. Measurement of the Proton Structure Function F_2 at Low x and Low Q^2 at HERA. *Zeit. f. Phys.*, C69:607–620, 1996.

[Der96b] M. Derrick et al.; ZEUS Collaboration. Rapidity Gaps between Jets in Photoproduction at HERA. *Phys. Lett.*, B369:55–68, 1996.

[Des95] K. Desler, U. Schneekloth. The Hardware of the Proton Remnant Tagger (PRT) in 1994. *ZEUS-Note 95-061*, 1995.

[Fos95] B. Foster. Private Communication, 1995.

[Fre94] A. Freidhof. Bestimmung der Ereigniszeit von ep-Wechselwirkungen durch Kalometrie am ZEUS-Detektor. PhD Thesis, 1994.

[GEA] GEANT,Detector Description and Simulation Tool. CERN Program Libray Long Writeup W5013.

[Geo94] S. George, J.P. Fernandez, L. Labarga, J. Hartmann, C.G. Matthews, R. Ullmann. Study of Neutral Strange Particle Production in Deep Inelastic Scattering. *ZEUS-Note 94-155*, 1994.

[Geo95] S. George. Study of Strange Meson Production in Deep Inelastic Scattering with the ZEUS Detector at HERA. PhD Thesis, 1995.

[Gou83] K. Goulianos. Diffractive Interactions of Hadrons at High Energies. *Phys. Rep.*, 101, No.3:169–219, 1983.

[Har96] G. F. Hartner, Y. Iga, J. B. Lane, N. A. McCubbin. VCTRAK (3.06/20): Offline Output Information. *ZEUS-Note 96-013*, 1996.

[HER90] HERMES Collaboration. A Proposal to Measure the Spin-Dependent Structure Function of Neutron and Proton at HERA, 1990.

[HER94] HERA-B Collaboration. HERA-B An Experiment to study CP Violation in the B System Using an Internal Target at the HERA Proton Ring. *DESY PRC 94-02*, 1994.

[Ing85] G. Ingelman, P. E. Schlein. Jet Structure in High Mass Diffractive Scattering. *Phys. Lett.*, B152:256–260, 1985.

[Ing91] G. Ingelman. LEPTO Version 6.1 - The Lund Monte Carlo for DIS Lepton-Nucleon Scattering. In W. Buchmüller and G. Ingelman, editor, *Physics at HERA*, volume 3, pages 1366–1394, 1991.

[Jac79] F. Jacquet, A. Blondel. In U. Amaldi, editor, *Proceedings of the Study of an ep Facility for Europe*, pages 391–394, 1979.

[Jam94] F. James. MINUIT, Function Minimization and Error Analysis. *CERN Program Library Long Writeup*, D502, 1994.

[Jon85] G. T. Jones et al.; WA21 Collaboration. The K^0/π^- Ratio and Strangeness Suppression in νp and $\bar{\nu} p$ Charged Current Interactions. *Z. Phys.*, C27:43–52, 1985.

[Jon93] G. T. Jones et al.; WA21 Collaboration. Neutral Strange Particle Production in Neutrino and Antineutrino Charged Current Interactions on Protons. *Z. Phys.*, C57:197–209, 1993.

[Koe94] L. Koepke, R. van Woudenberg. Photon Conversions in the ZEUS Detector. *ZEUS-Note 94-016*, 1994.

[Kwi91] A. Kwiatkowski, H. Spiesberger, H.-J. Möhring. HERACLES, An Event Generator for ep Interaction at HERA Including Radiative Processes. In W. Buchmüller and G. Ingelman, editor, *Physics at HERA*, volume 3, 1991.

[Lön92] L. Lönnblad. ARIADNE Version 4 - a Program for Simulation of QCD Cascades Implementing the Colour Dipole Model. *Computer Physics Communications*, 71:15–31, 1992.

[Lön94] L. Lönnblad. Rapidity Gaps and Other Final State Properties in the Colour Dipole Model for Deep Inelastic Scattering. *CERN-TH.7307/94*, 1994.

[Low75] F. E. Low. Model of the Bare Pomeron. *Phys. Rev.*, D12:163–173, 1975.

[Mar93] A. D. Martin, R. G. Roberts and W. J. Stirling. Parton Distributions Updated. *Phys. Lett.*, B306:145–150, 1993.

[Mat94] C. G. Matthews. V0FIND: A Secondary Vertex Finder for ZEUS. *ZEUS-Note 94-010*, 1994.

[McA56] R. W. McAllister and R. Hofstadter. Elastic Scattering of 188 MeV Electrons from the Proton and the Alpha Particle. *Phys. Rev.*, 102:851–856, 1956.

[Nac86] Nachtmann, Otto. *Phänomene und Konzepte in der Hochenergiephysik*. Friedr. Vieweg & Sohn, 1986.

[Nik92] N. N. Nikolaev, B.G. Zakharov. Pomeron Structure Function and Diffraction Dissociation of Virtual Photons in Perturbative QCD. *Z. Phys.*, C53, 1992.

[Nik94] N. N. Nikolaev, B.G. Zakharov, V.R. Zoller. The Spectrum and Solutions of the Generalized BFKL Equation for Total Cross Section. *KFA-IKP(Th)-1994-1, Submitted to Phys. Lett. B*, 1994.

[Nus75] S. Nussinov. Colored-Quark Version of Some Hadronic Puzzles. *Phys. Rev. Lett.*, 34:1–286, 1975.

[Par96] Particle Data Group. Particle Properties Data Booklet, 1996.

[Per74] M. L. Perl. *High Energy Hadron Physics*. John Wiley & Sons, New York, 1974.

[Roc47] G. D. Rochester, C. C. Butler. Evidence for the Existence of New Unstable Elementary Particles. *Nature*, 160:855–857, 1947.

[Sjö86] T. Sjöstrand. The Lund Monte Carlo for Jet Fragmentation and e^+e^- Physics - JETSET Version 6.2. *Computer Physics Communications*, 39:347–407, 1986.

[Sjö94] T. Sjöstrand. PYTHIA 5.7 and JETSET 7.4 The Lund Monte Carlo for DIS Lepton-Nucleon Scattering. *CERN-TH.7112/93*, 1994.

[Vre94] M. Vreeswijk et al. Monte Carlo Studies for a Presampler in ZEUS. *ZEUS-Note 94-004*, 1994.

[Wró90] A. K. Wróblewski. Soft Hadron Physics. In K. K. Phua and Y. Yamaguchi, editor. *Proceedings of the 25th International Conference on HEP, Singapore*, volume 1, pages 125–143, 1990.